STANDARDIZING INDIRECT TARGETING AND BUILDING ELECTROPHYSIOLOGICAL MAPS FOR DEEP BRAIN STIMULATION SURGERY AFTER ACCOUNTING FOR BRAIN SHIFT

By

SRIVATSAN PALLAVARAM

Dissertation
Submitted to the Faculty of the
Graduate School of Vanderbilt University
in partial fulfillment of the requirements
for the degree of
DOCTOR OF PHILOSOPHY
in
Electrical Engineering
August, 2010
Nashville, Tennessee

Approved by:
Professor Benoit M. Dawant
Professor Robert Bodenheimer
Professor J. Michael Fitzpatrick
Dr. Peter E. Konrad
Dr. Joseph S. Neimat

To my dear parents, loving wife, supportive brother and my teachers.

ACKNOWLEDGEMENTS

I am grateful to all of those who made this dissertation possible. First and foremost, I would like to express my sincere gratitude to my advisor Dr. Benoit Dawant for his guidance and help during this work. He has been a true inspiration for me. I have learnt as much from Dr. Dawant on the science of research, and the importance of perseverance, patience, collaboration and professionalism as I have on the technical details of the project. Every time I have had a one-on-one meeting with him I have felt his passion and sincerity in passing on his experience and knowledge, and I have always gained from it. I would like to thank him for his kindness, encouragement and support during some very tough times and for giving me the opportunity and the funding to work on this project. I am proud to have trained under him and I am sure a lot of what I have learnt from him will stay with me forever.

Thanks are due to Dr. J. Michael Fitzpatrick for his constructive feedback and insight. I have always been inspired by his passion for perfection and teaching. Interacting with him has been a very humbling experience and it inspires me to remember that there is always so much to learn. I look up to him and feel fortunate to have his input. I want to thank Dr. Bobby Bodenheimer for his valuable suggestions and collaboration during various stages of the project. Many thanks are due Dr. Peter Konrad and Dr. Joseph Neimat from neurosurgery for their time and insightful suggestions, and for providing me invaluable access to their operating rooms and clinics which provided the backbone for this work. I appreciate how fortunate I am to have access to such supportive neurosurgeons. Both Dr. Konrad and Dr. Neimat always make time for research and that has been a great help to me. I want to particularly thank Dr. Konrad for always keeping his doors open for me in spite of his extremely busy schedule. His passion for research is truly inspirational and I am very grateful to him for his support and encouragement. It is simply amazing how he is always welcoming and unruffled even in the tightest of situations. Very special thanks are due to Dr. Pierre-François D'Haese whose doctoral work laid the foundation for this dissertation. I am very grateful to Pierre for his immense support and tremendous guidance throughout. He has been a mentor and a friend with whom I have worked very closely on the project. His technical input has been extremely valuable to me and I look forward to continuing to work with him. I have learnt a lot from each of you on the technical, professional and personal fronts. I look forward to many more collaborations with you all.

I would also like to thank Dr. Thomas Davis and Dr. Fenna Phibbs from neurology for their collaboration and for providing access to their clinics. I look forward to working with them even more closely on the post-operative programming project in the near future. Thank you to Dr. Chris Kao, Dr. Michael Remple and Corrie Camalier for their help with gathering intra-operative data. I am grateful to Rui Li whose fantastic visualization tools came in extremely handy during my work. Thank you to Dr. Prashanth Dumpuri for his guidance and friendship and his willingness to help at all times. I also want to thank all the members of the Medical Image Processing Lab for their support.

Thanks are due to Hampton Albert who has been ever so helpful with all my computer needs, to Sandy Winters and Linda Koger for being incredibly approachable and helpful. I am also thankful to the operating room and medical staff for their assistance during this work.

My family gave me boundless support in the pursuit of this degree. I would like to thank my parents Mr. P.D. Srinivasan and Mrs. P.S. Pushpalatha to whom I am ever indebted for the innumerable sacrifices they have made for me, and for the values they have instilled in me. My father had to give up a lot for my sake and I want him to know that I appreciate it from the bottom of my heart. He was my role model as I was growing up and he continues to inspire me. I have learnt so much from him. I thank my mother for her fortitude in enduring tremendous hardships to keep our family together during very difficult times, for dedicating her life to the family and for always caring for us selflessly. My dear brother Srikanth Srinivasan is and will always remain close to my heart for the pillar of support that he is to me. I know that I can always count on him and I love him dearly. My loving wife Dr. Poonkuzhali (Anjali) deserves many thanks for her love and relentless support and for changing my life into a dream come true. While she continues to amaze me as my wife and best friend, I cannot cease to admire her for her ambitions and professional accomplishments, and how she finds a way to balance them with family. I am indeed fortunate to have such wonderful people in my life. I dedicate all my work to them.

Financial support for this work came from the NIH (Grant No. R01EB006136).

TABLE OF CONTENTS

Content Page

Chapter

LIST OF TABLES

Table Page

LIST OF FIGURES

CHAPTER I

INTRODUCTION

I.1 A brief introduction to Deep Brain Stimulation (DBS) surgery

Movement disorders like Parkinson’s disease (PD), essential tremor (ET) and dystonia affect approximately 1 million, 1.5 million and 250,000 people respectively in the United States [1]. Direct health-related expenses, indirect disability expenses and lost productivity in the United States for PD alone amount to $25 billion annually [2]. Since its first FDA approval in 1997, high frequency DBS has become a contemporary treatment of these diseases as well as of an emerging number of other focal neurological disorders [10-14]. It is offered to patients who have begun to see failure with standard medical therapy and also to patients in whom medical therapy is poorly effective. DBS involves the placement of a 4-contact electrode shown in figure 1 (Medtronic #3387 or #3389 quadripolar lead®, Medtronic, Inc., Minneapolis, MN), in the deep brain. Stimulation is applied with the aid of a stimulator implanted in the patient’s chest. Converging computational and experimental results [14, 15] suggest that therapeutic DBS generates an excitatory effect on axons surrounding the electrode. Although correlations between axonal activation and the therapeutic mechanisms of DBS remain controversial, one leading hypothesis is that high-frequency stimulation overrides the underlying pathologic neural activity patterns [3-5].

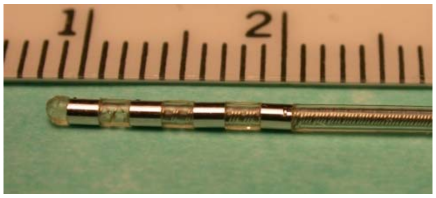

Figure 1. Medtronic #3387 quadripolar lead® (Medtronic Inc., Minneapolis, MN). Each silver band is one stimulating contact. The scale is in centimeters.

Effective stimulation results when the contacts surround the optimal target [6]. If the contacts are located away from the optimal location, ineffective stimulation results due to several reasons: a) failure to capture control of the desired group of neurons, b) stimulation of non-desirable areas resulting in unpleasant stimulation, or c) necessity for higher stimulus intensities to produce the desired effect resulting in reduced battery life of the implant. Therefore, targeting the specific neurons of interest for this therapy requires precision and allowance for variability among patients.

The pre-operative stage involves planning for the location of implantation of a multi-contact electrode in a specific region deep within the brain, the intra-operative stage involves the placement of the electrodes after refining the pre-operative target based on data collected during the surgery and the post-operative stage involves choosing the appropriate contact(s) as well as stimulation settings that will provide maximum therapeutic benefit (reduction in symptoms with minimum or no adverse effects).

Specifically, during the pre-operative stage, based on experience and knowledge of the anatomy the neurosurgeon selects what he/she believes would be the optimal target for electrode implantation by visualizing the patient’s images. During the intra-operative stage, the pre-operatively selected target is refined by probing the surrounding region with a recording and/or a stimulating electrode. Micro-electrode recordings and semi-micro/macro stimulation responses are useful to accurately locate the target and optimize the final position of implantation [18-23]. The recording electrode is used to characterize the neuronal firing patterns, which are then used to infer locations of deep brain nuclei relevant to the targeted region. Stimulating electrodes are used to elicit responses in an awake patient. Both these sources of information allow the neurosurgeon, neurologist, and neurophysiologist to establish functional borders and to mentally reconstruct the somatotopic arrangement of the structures of interest. This, in turn, allows the surgical team to correct for initial targeting errors based on detailed knowledge of the intended therapeutic effect versus unintended adverse effects from the final implanted electrode. The clinical judgment of where the final electrode position should be requires sub-specialty training in neurosurgery. The post-operative stage is referred to as the stage of programming the electrode where the goal of the neurologist is to find the optimal contact and the stimulator settings that can provide the best therapeutic benefit (maximize symptom relief, and minimize adverse effects if any). The surgery can be a lengthy process (sometimes extending for hours with the patient awake) and the entire procedure from pre-operative to post-operative stage requires expertise in neurosurgery, neurophysiology, and clinical neurology [7, 8]. This combined expertise is available only at a limited number of sites, which limits access to the procedure for a small fraction of the patients who would benefit from it.

I.2 Indirect targeting based on anterior and posterior commissures

Common targets of interest for DBS are poorly visible in current imaging modalities. Therefore, in normal clinical practice pre-operative target localization is typically done by indirect targeting which involves determining the position of the targets with respect to landmarks visible in the images. A popular indirect targeting approach defines a coordinate system based on the Anterior and Posterior Commissures (AC and PC). The commissures are fiber tracts connecting the two cerebral hemispheres. The posterior commissure lies just in front of and above the superior colliculi, and below the pineal gland. The anterior commissure runs just in front of the fornix. Average standardized ACPC-based target coordinates for SubThalamic Nucleus (STN) [9], Globus Pallidus Internus (GPi) [9], and Ventralis intermedius nucleus (Vim) [10] are given in table 1.

Table 1. Average AC-PC coordinates for target locations inside the STN, Vim and GPi reported in literature to clinically produce successful symptom reduction due to DBS.

Nucleus	**Coordinates (mm)**		
	Vertical (origin)	**Lateral (origin)**	**AP (origin)**
STN	-4 (MC)	12 (MC)	-3 (MC)
Vim	0 (MC)	12 (MC)	-6 (MC)
GPi	-2 (MC)	20 (MC)	5 (MC)

Since this approach continues to be commonly used, the definition of a standard coordinate system that can be consistently reproduced across patients is necessary for effective communication of target locations. Therefore, it is valuable to quantify the variability among neurosurgeons in manually selecting AC and PC points on typical MRI scans used for neurosurgery and to further evaluate the effect this variability can have on the accuracy of localizing targets and communicating the same.

An automated and robust method based on image features for the localization of the anterior and posterior commissure points can aid in standardizing the AC-PC based coordinate system. Therefore, it is useful to investigate the accuracy with which an automatic method can select the AC and PC so that such a method can be used to overcome the inter-surgeon variability in selecting these points. To that end, an atlas-based method has been applied to predict the position of AC and PC automatically and its accuracy has been validated. More importantly, the focus of this work is to validate the method against clinically selected points in a large number of patients as well as against a gold standard selected in a controlled laboratory setting.

Target selection can also be done by direct targeting in which the target is selected by locating it on the patient images (if visible on those images) or by overlaying the target from atlases like the Talairach [11] or Schaltenbran-Wahren (S-W) [12] atlas onto the patient images. These atlases consist of unevenly spaced brain sections that have been histologically stained to reveal the structures and sub-structures of interest. However, such atlases are imperfect because they are either limited to one sectioning plane per hemisphere (Talairach) when a single brain is used or to non-contiguous anatomy in intersecting orthogonal slices (S-W) when several brains are used.

Alternatives to these have been developed recently by Yelnik et al. [13] and Bardinet et al. [14]. These approaches involve one 3D histological atlas reconstructed from thin contiguous slices registered to their MR volume. Automatic segmentation of anatomical structures of interest can then be obtained by registering the atlas MR volume to the patient MR volume. Chakravarty et al. [15, 16] also proposed a 3D anatomical atlas that was derived from a set of serial histological data. To aid the surgical target identification several groups use rigid or non-rigid alignment of the digitized stereotactic [15, 17-20] and histological atlases with patient-specific pre-operative brain images.

However, there is a lack of consensus on the exact location where stimulation can provide the best efficacy for a given disease. While STN is a popular target for PD, the precise location of the optimal target is not straightforward because STN is not clearly visible on conventional imaging used for DBS. Locating sub-regions of STN on the images is even more challenging. Using micro-electrode recordings data to identify nuclei based on neuronal signatures, Lanotte et al. [21] located the center of the STN in a number of patients and found the variability in their positions to be approximately 4 mm in each direction; namely, anterior-posterior, medial-lateral, and dorsal-ventral. It has been reported by Plaha et al. [22] that there are multiple regions in the brain where efficacy for a given movement disorder can be achieved by DBS. For instance, for PD it is reported that both the dorsal part of the STN and zona inserta (ZI) provide symptom relief. Andrade-Souza et al. [23] recommended the use of a target near the superior portion of the nucleus. However, Maks et al. [24] have recently reported that patient-specific models showed that therapeutic benefits were achieved with direct stimulation of a wide range of anatomical structures in the STN region in 10 PD patients. Furthermore, Zonenshayn et al. [25] found that anatomical targeting methods including direct targeting, S-W atlas and AC-PC based indirect targeting resulted in targets that were statistically different from the final MER-based electrophysiological targets. Thus, there is a need for the development of accurate electrophysiological atlases that can be used during the various stages of DBS.

I.3 Building electrophysiological atlases and maps

As mentioned in section I.1, intra-operatively acquired micro-electrode recordings and stimulation response data allow the neurosurgeon, neurologist, and neurophysiologist to establish functional borders and to mentally reconstruct the somatotopic arrangement (organization of sensory and motor areas of the brain) of the structures of interest. This, in turn, allows the surgical team to plan electrode displacements. From the post-operative stage, similar stimulation response data as well as information on the clinically selected contact and the stimulator settings can be recorded. Using all this information from a population of patients, accurate electrophysiological atlases of intra-operative observations can be developed. Nowinski et al. [26] have contributed a Probabilistic Functional Atlas (PFA) for the STN using spatial distribution data of the locations of clinically active contacts in a number of patients. But, this atlas does not contain any stimulation response data collected either intra-operatively or during post-operative programming of the electrode. Finnis et al. [27] describe a functional database used to capture and normalize information acquired intra-operatively. The data is normalized spatially by registering the MR volume of each patient to one reference volume with a combination of rigid and non-rigid registrations. D'Haese et al. [28, 29] have shown techniques by which a computer system can be used to predict the pre-operative planned target. The techniques involve creating statistical atlases of implant positions in a population of patients. Guo et al. [30] compared a number of methods for STN DBS targeting including direct targeting, use of anatomical atlases [12], electrophysiological databases [31], actual surgical targets from a population of patients [28] and a combination of these methods. They found that the electrophysiological database, actual surgical target locations, and the combination of approaches based on functional and anatomical information, provided more accurate initial estimation of the surgical target positions than those techniques dependent solely on anatomical references. Castro et al. [32, 33] have shown atlas-based targeting using non-rigid registration similar to the method by D'Haese et al. [34]. In [34], D'Haese et al. used MRI image volumes as atlases and performed non-rigid registration between the atlases and MR images of patients using the adaptive bases algorithm proposed by Rohde et al. [35]. Pluim et al. [36] provide a detailed survey of mutual-information-based methods for medical image registration. Chakravarty et al. [16] survey various atlas warping techniques used for DBS and suggest that template-based atlas-to-patient warping techniques such as the methods above that use MRI imaging for atlas creation work best for customizing the atlas onto patient data.

With reliable techniques for warping MRIs of patients to an atlas MRI, intra-operatively acquired electrophysiological data can be mapped from a population of patients onto the atlas MRI. The collection of such data in the atlas MRI space is referred to as an *electrophysiological atlas*. This data includes micro-electro recordings, stimulation responses, pre-operative targets, final intra-operative implant positions, post-operative implant positions, etc. Such data can be processed to make them more informative for identifying high likelihood regions by creating what are referred to as *statistical electrophysiological maps* or simply *statistical maps* in the remainder of this dissertation. D'Haese et al. [34] showed how statistical maps of stimulation response data could be created by placing a Gaussian kernel at each stimulation response data point and combining those kernels. Guo et al. [37] also built stimulation response maps using this method for automatic target planning. However, as will be discussed in chapter IV, this method has certain drawbacks that need to be addressed.

I.4 Brain shift in DBS

In stereotactic neurosurgery, an underlying assumption is that anatomical structures do not move between the time of the pre-operative image acquisition and the time of the surgery. However, this assumption is not valid. For years, neurosurgeons and researchers have investigated the value of tracking brain shift during surgery for invasive procedures such as brain tumor resection [39, 40]. Gerdes et al. [38] in 1975 first described the error resulting from subdural air invasion and "brain sinking" in stereotactic procedures. Recently, by comparing pre- and post-operative images, Wester et al. [39], Winkler et al. [40], Khan et al. [41] reported that brain tissues can in fact shift during DBS surgery. Using real-time intra-operative MRI, Martin et al. [42] reported that appreciable ipsilateral brain shift was evident during burr hole access. Khan et al. [43] studied 25 subjects that underwent DBS surgery and analyzed brain shift between pre- and post-operative 3D MRI scans. Brain shift of up to 4 mm was observed in deep brain structures. The mean and standard deviation (and maximum) of shift magnitudes for the AC, PC, medial-anterior corners of left and right putamen were 1.8 ± 0.7 (2.9) mm, 1.6 ± 0.8 (2.9) mm, 1.8 ± 0.9 (3.5) mm, and 2.0 ± 0.7 (3.9) mm, respectively. Winkler et al. [40]

reported intra-operative brain movement of 2 mm in the region of the STN in a case study. By comparing post-operative MRI acquired on the day of the surgery with pre-operative MRI, Miyagi et al. [44] reported medial, posterior and inferior shifts of 0.69 ± 0.45 mm, 2.23 ± 0.93 mm and 0.58 ± 0.77 mm respectively for AC. For PC, these shifts were 0.35 ± 0.26 mm, 1.03 ± 0.90 mm and 0.37 ± 0.47mm. Halpern et al. [45] reported that shift appeared to impact the number of microelectrode tracks required to optimize STN targeting.

Intra-operative brain shift happens due to loss of cerebrospinal fluid and air invasion into the skull through the burr hole, gravitational force [46], change in pressure due to skull opening during the surgery, pneumocephalus, and forces due to insertion of the DBS lead. It could increase during the procedure due to the length of the procedure itself and failure or delay in sealing the burr hole. A shift of deep brain structures by only a few millimeters can potentially increase the number of required exploratory tracks and impact implantation accuracy. Although intra-operative neurophysiological techniques such as microelectrode mapping and macroelectrode stimulation may compensate for it, brain shift may require greater number of micro- and macro-electrode passes thereby lengthening the procedure and increasing the likelihood of complications. A review of STN-implanted patients in 2001 by the DBS for PD study group suggested that the higher the number of microelectrode passes the higher the risk of intracranial bleeding during DBS [47].

Thus, brain shift can have an effect on the functional atlases and databases of intra-operative observations and statistical maps of such data developed by various groups which have been discussed earlier [27, 31, 34, 37, 48, 49]. This is because to create such atlases pre-operative image volumes are typically used whereas due to brain shift the pre- and intra-operative coordinates of anatomic structures may be different. Therefore, ignoring brain shift could lead to inaccuracies and imprecision in the statistical atlases and maps and reduce the predictive value of systems that use this information. Model-driven brain shift compensation techniques [50] are difficult to implement in burr hole surgeries such as DBS due to very limited brain surface deformation information. In the latter part of the dissertation, the effect of brain shift on building electrophysiological atlases is studied and approaches to build shift-corrected atlases are discussed and validated.

I.5 Using electrophysiological atlases for DBS

Limousin et al. [51] reported that neurophysiological guidance changed the target coordinates in 87% of the procedures in an experienced surgical team. These authors and others have concluded that guidance is a useful tool to improve and confirm target localization. The longer the intervention and the greater the number of tracks, the higher the possibility of adverse effects [52]. Gironell et al. [53] have presented benefits of a computerized intra-operative neurophysiological navigator system in helping a surgical team select the optimal target. A number of functional atlases and databases [16, 26, 27, 29, 34, 48, 54, 55] containing intra-operatively acquired sub-cortical electrophysiology from a number of patients have been implemented to complement the anatomical and histological atlases. Butson et al. [56-58] developed a detailed methodology to predict the volume of tissue activated (VTA) during DBS as a function of electrode design and stimulation parameter settings. D'Haese et al. have shown preliminary results on using electrophysiological maps for post-operative programming assistance in DBS. Thus, a number of groups have seen the need for the use of electrophysiological atlases in DBS. However, these systems either are still being validated for their use to provide assistance to the surgical team or do not address the issues described in the previous sections. Towards the end of the dissertation, the use of electrophysiological maps built based on the results from earlier chapters is investigated for post-operative programming assistance. The feasibility of using such an atlas for intra-operative assistance is also discussed.

The dissertation is organized in the following manner to best present the contributions:

Chapter II investigates the inter-surgeon variability in manually selecting the anterior and posterior commissures (AC and PC) and the effect this has on AC-PC based localization of common DBS targets.

Chapter III validates the accuracy of an atlas-based method for the prediction of commissures by comparing the predictions against careful manual selections by a large number of neurosurgeons as well as against clinical selections in a large number of patients.

Chapter IV describes the limitations of the previous model (Gaussian kernel) used for building statistical maps of stimulation response. A new model (Gaussian smoothed spherical shell kernel) is proposed and maps generated by the two models are compared.

Chapter V shows the effect of intra-operative brain shift on the creation of electrophysiological atlases using intra-operative MER and stimulation response data from a population of patients.

Chapter VI proposes two different approaches to build electrophysiological maps after accounting for brain shift. Maps built using the new kernel as well as after accounting for brain shift are validated in this chapter.

Chapter VII provides preliminary results for post-operative programming assistance using electrophysiological maps built using the new model after accounting for brain shift.

Chapter VIII provides the summary of the work and discusses possible future work.

CHAPTER II

INTER-SURGEON VARIABILITY IN THE SELECTION OF ANTERIOR AND POSTERIOR COMMISSURES (AC AND PC) AND ITS POTENTIAL EFFECTS ON TARGET LOCALIZATION

Abstract

The selection of the anterior and posterior commissures (AC and PC) defines the reference system by which stereotactic coordinates of targets are communicated in the literature and among surgeons. Atlases like the Nowinski [26] atlas also use AC and PC for normalization of a population of patients to a common reference space. Thus, it is important to quantify errors that may occur in this reference system because of difference in visual localization of AC and PC points. In this chapter, a study on the inter-surgeon variability in manually selecting the anterior and posterior commissures (AC and PC) and the effect this has on AC-PC based localization of common DBS targets is presented.

This work was published in the Journal of Stereotactic and Functional Neurosurgery in 2008 [59].

II.1 Introduction

Based on the standard convention of the Schaltenbrand-Wahren atlas, AC and PC are defined as two points with the shortest, intraventricular distance between the commissures [12]. The mid-commissural point (MC), or the midpoint of the line connecting AC and PC, is the most common origin of the coordinate space used for stereotactic targeting. Some neurosurgeons continue to use the traditional definition of AC-PC distance to signify the shortest, intraventricular distance based on the traditional method of determining this by ventriculography and true lateral skull X-rays. On the other hand, most stereotactic neurosurgery relies on MRI imaging today, and some neurosurgeons use the middle of the commissure versus the intraventricular edge of the commissure to designate the AC and PC points. Because the selection of the AC and PC points defines the reference system by which stereotactic coordinates are communicated in the literature and among surgeons, it is important to quantify errors that may occur in this reference system because of difference in visual localization of AC and PC points. Furthermore, any discussion of localization of targets like the subthalamic nucleus (STN), ventralis intermedius nucleus (Vim) and globus pallidus internus (GPi) based on AC-PC is limited by the variability of visually selected AC and PC selections. The variability in manual AC-PC selections by 43 neurosurgeons that specialized in stereotactic neurosurgery was examined. The impact this variability has on the localization of three popular deep brain stimulation (DBS) targets was also evaluated.

II.2 Data and Method

During the American Society for Stereotactic and Functional Neurosurgery (ASSFN) conference held in Boston, MA, USA in 2006, 43 neurosurgeons (38 attendings and 5 residents/fellows) selected AC and PC (as they routinely do for surgical planning) on two high resolution MRI volumes. The scans were displayed on a laptop computer with image-viewing software containing simple tools for slice selection, zooming, and point selection. Both MRI volumes were acquired as sagittal T1 sequences (referred to as Patient1 with 1mm x 1mm x 1.2mm resolution and Patient2 with 1mm x 1mm x 1mm resolution, TR 8.05ms, TE 3.68ms) on a 1.5T Phillips Medical Systems scanner. Both scans were displayed to the neurosurgeons at a resolution of 1mm x 1mm x 1mm in three standard views (axial, sagittal, and coronal) simultaneously. A point selection made on one view was also displayed on the other two views to allow further refinement on any of the three views. Figure 2(a) shows a snapshot of one of the scans as shown to the neurosurgeons.

Every attempt was made to not provide any verbal cues or assistance to the surgeons while selecting the AC and PC points so that bias was minimized. To completely define the AC-PC reference system, a point on the mid-sagittal plane is required in addition to the AC and PC points. Surgeons were not asked to pick the mid-sagittal plane point (MP) in order to limit interaction time. Instead, the MP was designated by a senior neurosurgeon and remained the same in all measurements. The X, Y, and Z coordinates (in mm) of AC and PC selections were recorded and the mid-commissural point (MC) was calculated for each neurosurgeon's pair of AC and PC. The data consisting of the coordinates (X, Y, Z) of the manual selections made by the neurosurgeons for each MRI volume were further divided in two sets: pointset_all including selections by all 43 neurosurgeons and pointset_attendings including selections by only the 38 attending neurosurgeons.

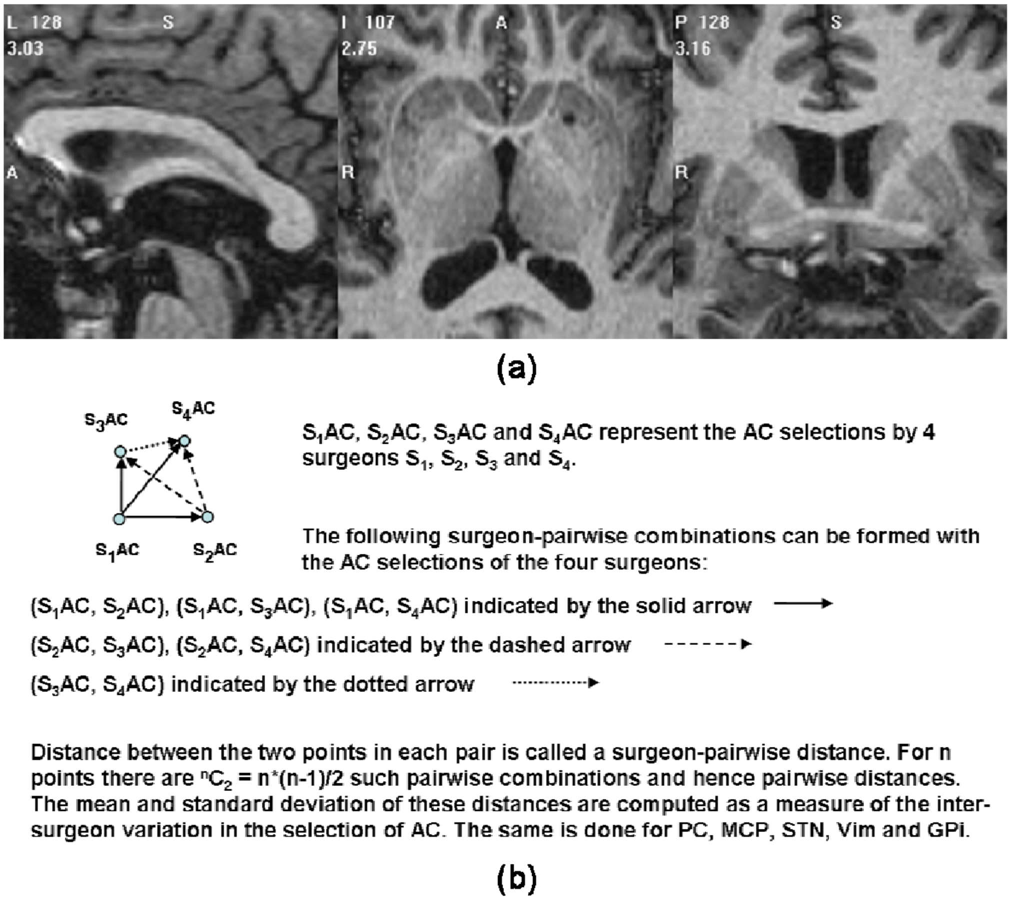

S_1AC, S_2AC, S_3AC and S_4AC represent the AC selections by 4 surgeons S_1, S_2, S_3 and S_4.

The following surgeon-pairwise combinations can be formed with the AC selections of the four surgeons:

(S_1AC, S_2AC), (S_1AC, S_3AC), (S_1AC, S_4AC) indicated by the solid arrow ⟶
(S_2AC, S_3AC), (S_2AC, S_4AC) indicated by the dashed arrow - - - - - -▸
(S_3AC, S_4AC) indicated by the dotted arrow ·········▸

Distance between the two points in each pair is called a surgeon-pairwise distance. For n points there are $^nC_2 = n*(n-1)/2$ such pairwise combinations and hence pairwise distances. The mean and standard deviation of these distances are computed as a measure of the inter-surgeon variation in the selection of AC. The same is done for PC, MCP, STN, Vim and GPi.

Figure 2. (a) Sample display from the image viewer software. The number on the top in the upper-left corner of each view refers to the slice number and the bottom number refers to the zoom factor. L=left, R=right, I=inferior, S= superior, A=anterior, P=posterior. (b) Illustration of the computation of “surgeon-pairwise distances” between surgeon selections.

Surgeon-Pairwise distances as a measure of inter-surgeon variability

Traditionally, the spread of a cluster of points is measured as the mean distance from the centroid of the cluster to a given point, but this does not provide a direct measure of distances between points in the cluster. In this study, which focuses on measuring inter-surgeon differences, we have opted for pairwise distances. Suppose, for instance, that S_1AC, S_2AC, S_3AC, and S_4AC are the AC selections by four surgeons S_1, S_2, S_3 and S_4 and that distance(a, b) is the distance between points a and b, then we compute distances between the four surgeon selections taken pairwise, i.e., distance(S_1AC, S_2AC), distance(S_1AC, S_3AC), distance(S_1AC, S_4AC), distance(S_2AC, S_3AC), distance(S_2AC, S_4AC) and distance(S_3AC, S_4AC) and call these surgeon-pairwise distances. Their mean, standard deviation (SD) and median (to eliminate the effect of outliers) were computed as a measure of the inter-surgeon variability in selecting the AC. This is illustrated in figure 2(b).

Measuring the inter-surgeon variation at AC, PC and MC and the resultant variation at targets

The method described above was applied to the AC, PC and MC coordinates for each surgeon pair to calculate the inter-surgeon variability at the commissures and at the MC. The effect of variation in the selection of AC and PC on target localization was analyzed using coordinates published in the literature for STN [9], GPi [9], and Vim [10]. These standard coordinates are shown in table 1. Using the coordinates shown in table 1, (X, Y, Z) coordinates for STN, GPi and Vim targets were calculated from each neurosurgeon's

AC-PC selections. To generate a 3-dimensional coordinate space, one point in the mid-plane other than AC, PC and MC was chosen by a senior neurosurgeon on each MRI volume. This mid-plane point remained the same in all cases, and was used in the calculation of each of the targets in X, Y, Z coordinates. The surgeon-pairwise distances were computed from these as a measure of the inter-surgeon variability at the targets. This variability is due only to the variability in selection of the commissures.

Experiment to estimate the effect of mid-plane tilt

To study the effect of variations in the selection of one or more midplane points, which could not be studied with the data set acquired at the conference, a small experiment was carried out. On the same two volumes, two neurosurgeons selected multiple sets of three points on the falx that could potentially be picked by a neurosurgeon to fit the mid-plane. The AC and PC for each of the volumes were fixed. Mid-planes were then fitted through each set of points selected on the falx for each volume. Pairwise angles between all these planes (inter-plane angles) were then computed to measure the variability in selecting mid-planes. Based on the results of this experiment the effect of mid-plane tilt on target localization was studied.

II.3 Results

II.3.1 Inter-surgeon variability in localizing the anterior and posterior commissures

Mean and median surgeon-pairwise distances for the AC, PC and MC selections on *MRI volumes* 1 and 2 and both the datasets are given in table 2. The medians of AC and PC selection variability are similar. The mean of PC selection variability is substantially larger than that of AC selection variability when all the data points are pooled (*pointset_all*). Both mean and median of MC selection variability are smaller than those of AC and PC selection variability for both data sets on both MRI volumes. This suggests that the MC point is more consistent as a common reference point than the AC or the PC. However, it must be noted that the standard deviation for the MC point remains large when all the data points are pooled (*pointset_all*) in both MRI volumes.

Table 2. Mean and median of the surgeon-pairwise distances for manual AC-PC selections by 43 surgeons on two datasets (a) patient1, (b) patient2.

Surgeon pairwise distance (mm) (a) Patient1							
	pointset_all				***pointset_attendings***		
	AC	**PC**	**MC**		**AC**	**PC**	**MC**
Mean	1.92	2.27	1.47		1.53	1.45	0.85
SD	1.96	3.92	2.01		1.44	1.24	0.42
Median	1.26	1.23	0.89		1.21	1.17	0.81

Surgeon pairwise distance (mm) (b) Patient2							
	pointset_all				***pointset_attendings***		
	AC	**PC**	**MC**		**AC**	**PC**	**MC**
Mean	1.44	2.05	1.26		1.29	1.41	0.88
SD	1.05	3.46	1.68		0.77	1.62	0.78
Median	1.18	1.08	0.69		1.16	1.08	0.65

One reason for the variability at MC being smaller than that at the AC and PC stems from the fact that it is a computed quantity (average of two measurements - the AC and PC selections). Therefore, if the disparities between the surgeons are random and uncorrelated at the commissures, the variance at the MC is expected to be half the average of the variances at the commissures. However, the variance at the MC is considerably smaller than that. The reason for this could be the convention followed for selecting the commissures in MRI images. The manual selections could either be with respect to the intraventricular edge or middle of the commissure. In other words, if the AC was chosen posterior then the PC was chosen anterior, and if the AC was chosen anterior then the PC was chosen posterior with respect to the middle of each commissure. This trend was indeed found in 65% of the surgeon selections, thus accounting for the additional tightness at the MC clusters.

II.3.2 Variation in localization of STN, Vim and GPi targets due to variation in AC-PC selections

Mean and median surgeon-pairwise distances for the STN, Vim and GPi coordinates on *MRI volumes* 1 and 2 and both the datasets are given in table 3.

Table 3. Mean and median of the surgeon-pairwise distances for indirect targeting of STN, Vim and GPi based on manual AC-PC selections by 43 surgeons on two datasets (a) patient1, (b) patient2.

Surgeon pairwise distance (mm) **(a) Patient1**							
	pointset_all				***pointset_attendings***		
	STN	**Vim**	**GPi**		**STN**	**Vim**	**GPi**
Mean	2.64	2.75	3.31		1.15	1.45	1.21
SD	6.32	6.09	8.61		0.89	1.25	0.83
Median	1.02	1.24	1.15		0.94	1.20	1.02

Surgeon pairwise distance (mm) **(b) Patient2**							
	pointset_all				***pointset_attendings***		
	STN	**Vim**	**GPi**		**STN**	**Vim**	**GPi**
Mean	1.45	1.82	1.54		1.08	1.35	1.12
SD	2.07	2.83	2.01		1.37	1.71	1.17
Median	0.77	0.95	0.87		0.73	0.93	0.81

Effect of variation of mid-plane

The maximum pairwise inter-plane angle was found to be 1.00^0 for Patient1 and 1.70^0 for Patient2. We found that the effect of mid-plane orientation is maximum in terms of Euclidean shift on the localization of GPi (error = 0.71mm) as it is farthest away from the mid-plane laterally, followed by STN (error = 0.44mm) and then Vim (error = 0.43mm) for a 2^0 tilt in the mid-plane.

II.4 Discussion and Conclusions

The dataset populated with 43 neurosurgeons localizing AC and PC on the same two MRI volumes is unique. The results show that variation in manual selection of the AC and the PC is substantial and has a substantial effect on AC-PC based indirect target localization. They also show that the MC is a more consistent reference point than either the AC or the PC. This is likely due to canceling of differences among neurosurgeons using different conventions.

It is noteworthy that the error in designating AC and PC has the most effect on targets located more lateral from the midline. Based solely on the error in determining AC and PC, two neurosurgeons on average would select STN, Vim and GPi up to 2.64 mm, 2.75 mm and 3.31 mm apart respectively. This variability is significant because the distance between adjacent contacts on a standard DBS electrode is only 1.5 mm. Variability in selection of the mid-plane (which was held constant in the original experiment) adds further 0.44 mm, 0.43 mm and 0.71 mm variability in selecting STN, Vim and GPi respectively.

The two MRI image data sets used in this study were of high quality, with very limited motion artifacts because the images were acquired with the patient under anesthesia. The study, therefore, does not address the effect of quality of the images or the effect of large variability in brain anatomy (such as ventricular size). This may further have a significant impact on the surgeons' ability to select AC and PC accurately. It is expected that blurring due to motion artifacts in image volumes acquired with awake patients will further increase inter-surgeon variability.

The data set also strongly suggests that experience plays an important role in a neurosurgeon's ability to select the points accurately. For Patient1 the mean surgeon-pairwise distances for the attendings group are lower than those for the pooled group by 20% for AC and 36% for PC. These percentages for Patient2 are 10% for AC and 31% for PC. This translates into a mean increase in the surgeon-pairwise distance of targeting error in the pooled data (including residents/fellows) versus experienced stereotactic neurosurgeons (attendings) by 130%, 90% and 174% for STN, Vim and GPi respectively for Patient1. For Patient2, the increase in percentage targeting errors between the pooled data and attendings only are 34%, 35% and 37% for STN, Vim and GPi respectively.

The selection of the midplane point (MP) was held constant during the survey to reduce interaction time. Because of this, the effect of variation in selecting points on the falx on target selection could not be assessed in the subject population. But, the experiments indicate that this could introduce an additional error of 0.71 mm, 0.44 mm, and 0.43 mm at the GPi, STN, and Vim, respectively for a 2^0 tilt in the mid-plane. Although this is relatively small compared to the error of AC-PC selection, this error can become more significant in patients with a curved falx. The variability presented herein should thus be considered as a lower bound. This study highlights the difficulty of establishing a common reference system to communicate locations of target points based on visual inspection of the MRI for AC-PC reference points. Yet, when comparing therapeutic target locations, a method of normalizing targets with respect to a common reference system (AC-PC coordinates) is highly useful. The source of error we have measured is only one among several sources of errors that complicates the surgical procedures. Others include the accuracy of the stereotactic frame used to place the electrode or anatomical differences between patients. It is therefore difficult to measure directly the impact of AC and PC localization errors on the overall procedure or its outcome. It is, however, reasonable to believe that any source of error in the reference process could potentially lengthen the procedure by requiring more intra-operative adjustment or lead to suboptimal placements. This, in turn, could lead to less than optimal therapeutic response from the procedure.

A more accurate reference for stereotaxy would eliminate visual inspection of the AC-PC on MRI scans, and instead automate the selection based on imaging criteria. To that end, the first step is to develop automatic methods that would permit the accurate and consistent localization of the AC and the PC points [60-63]. The second is to develop algorithms that permit the automatic non-rigid registration of MRI images. D’Haese et al. [34] have used a non-rigid registration method [35] in the past for accurate localization of targets. In the next chapter, this non-rigid registration technique will be used for automatic AC and PC predictions and the accuracy of the predictions will be validated.

CHAPTER III

AN AUTOMATIC METHOD AND IT'S VALIDATION FOR THE ROUTINE SELECTION OF THE ANTERIOR AND POSTERIOR COMMISSURES IN MR IMAGES

Abstract

The previous chapter showed that there was substantial inter-surgeon variability in the manual selection of AC and PC and that this has a substantial impact on AC-PC based manual localization of targets. Since the AC and PC continue to be commonly used for targeting and communication of targets as well as for the normalization of patients to build certain atlases, there is a need for a method for accurate localization of these landmarks. In this chapter, an existing atlas-based technique is applied to predict the commissures. The accuracy of the method is validated by comparing the predictions against careful manual selections by a large number of neurosurgeons, and against selections made in a clinical setting as well as against gold standards created in a non-clinical setting.

This work was published in the Journal of Stereotactic and Functional Neurosurgery in 2009 [64] and the proceedings of SPIE Medical Imaging [60].

III.1 Introduction

The findings from the previous section suggest the need for automated and robust methods for the localization of the anterior and posterior commissure points. To that end an atlas-based method we have used in the past [34] for target predictions is applied to predict the position of AC and PC automatically. More importantly, the focus of this work is to validate the method against clinically selected points in a large number of patients as well as against a gold standard selected in a controlled setting. The results show that the predictions are more accurate than routine manual selection.

III.2 Data and Method

With IRB (Vanderbilt University IRB #060232) approval, a pre-operative 3D MRI scan (TR 12.2ms, TE 2.4ms, 256x256x170 voxels, with typical voxel resolution of 1x1x1 mm^3) was acquired for each patient using the SENSE parallel imaging technique (T1W/3D/TFE) from Philips on a 3T scanner. These images were acquired with the patient anesthetized and head taped to the table to minimize motion. The study presented herein includes 60 patients who underwent DBS surgery at our institution between December 2006 and January 2008.

Atlas-based automatic AC and PC predictions

An atlas-based method is used to predict automatically the position of AC and PC points. Atlas-based methods require two main components: (1) reference image volumes in which points or structures of interest have been localized and (2) registration algorithms, which permit the spatial realignment of the reference volumes to other image volumes in which the structures or points of interest need to be localized. Reference volumes in which the points of interests have been localized will be referred to as atlases in the remainder of the text. In this work, automatic spatial realignment or registration between image volumes is achieved in two steps. First, the volumes are realigned using an affine transformation (rotation, translation, and anisotropic scaling). This is followed by a non-rigid registration step. In this study, non-rigid registration is performed with the adaptive bases algorithm proposed by Rohde et al. [35]. Briefly, this algorithm computes a deformation field that is modeled as a linear combination of radial basis functions with finite support. This results in a transformation with several thousands of degrees of freedom. Two transformations (one from the atlas to the subject and the other from the subject to the atlas) are computed simultaneously and constrained to be inverses of each other. Both the rigid and non-rigid registration algorithms are mutual information based [65, 66].

Using this method, AC and PC points selected on an atlas volume can be projected onto a patient's volume to predict these points on that particular patient. Figure 3 illustrates this concept. The AC and PC from the atlas are projected onto the patient using a transformation (T) which is the result of rigid and non-rigid registrations between the atlas and the patient. This results in the automatic localization of the anterior and posterior commissures in the patient (AC_P and PC_P).

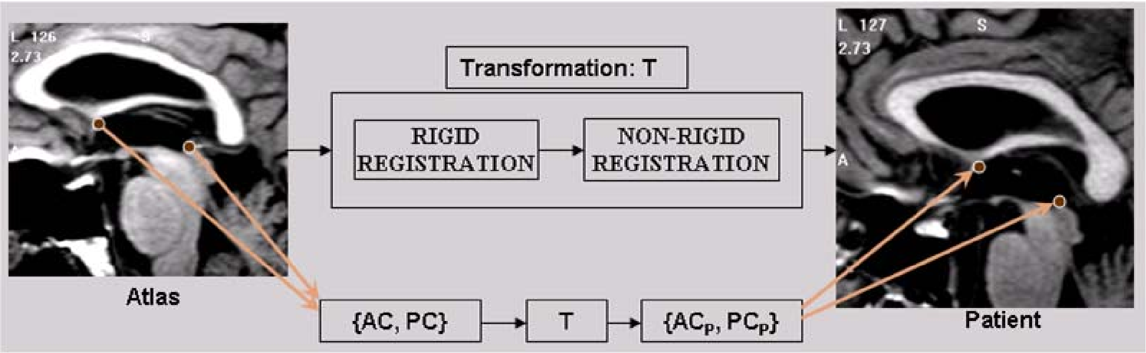

Figure 3. Atlas-based automatic method for predicting the anterior and posterior commissures on a patient (AC_P, PC_P) by applying a transformation T (result of rigid and non-rigid registration between atlas and patient) to the atlas points (AC, PC).

Multiple-atlases-based automatic AC and PC predictions

As others have observed (see for instance the work of Rohlfing et al. [67]), registration accuracy achievable by non-rigid registration may be influenced by morphological differences between the volumes to be registered. It is now relatively common to rely on outputs of several atlases to perform atlas-based segmentation [34, 67, 68]. To study the impact of the choice of an atlas on the process accuracy, four MRI image volumes were used as atlases. Three of these were patient volumes, which differed in size and/or shape (both overall and at specific structures like the ventricles). The fourth one was a synthetic volume generated by averaging 20 patient volumes using the method proposed by Guimond et al. [69]. This is an iterative method which starts with one of the volumes as a target and converges toward a volume that is representative of the population as a whole.

Figure 4 illustrates the extension of the single atlas approach described in the previous section to a multiple-atlases approach. The AC and PC points selected on each of the N atlases (AC^1 and PC^1, AC^2 and PC^2, …, AC^N and PC^N) are projected onto the patient volume (AC_P^1 and PC_P^1, AC_P^2 and PC_P^2, …, AC_P^N and PC_P^N) using the transformation between the respective atlas and the patient volume.

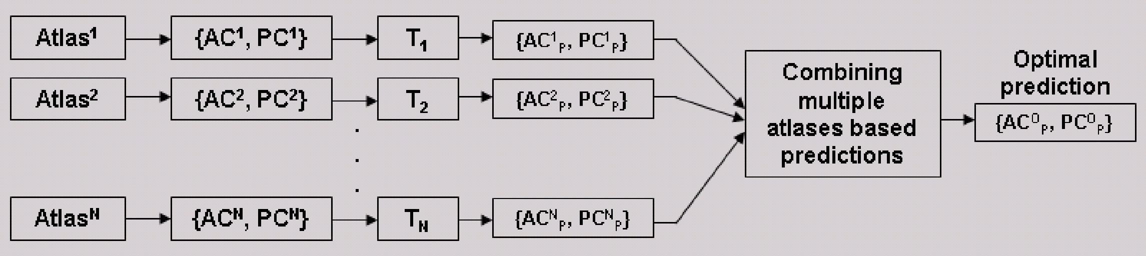

Figure 4. Using multiple atlases to produce optimal AC and PC predictions by combining the individual atlas-based predictions generated using the approach shown in figure 3.

The multiple predictions are then combined to produce the automatic prediction of the commissural points. The easiest way to combine the predictions from each atlas is to compute their average and use it as the optimal prediction. The drawback of this approach is that the predictions made by all the atlases are weighted equally, regardless of the quality of the registrations. In a 2005 study [70], we proposed an alternative approach in which the quality of the registration at a given location (STN), was estimated indirectly by estimating the quality of the segmentation of structures surrounding that location (thalamus, globus pallidus, and putamen). The measure of the quality of the segmentation is given by the specificity and sensitivity of the segmentations obtained with each atlas on these structures. These are computed using the STAPLE algorithm proposed by Warfield et al. [68]. The specificity and sensitivity values are then used to weigh the contribution of each atlas to the optimal prediction while eliminating the contributions of atlases that produce low sensitivity values for the structures (i.e., atlases that lead to poor segmentation results for structures surrounding the location of interest).

Manual localization of the points on the atlases

As shown in the previous study and in [59], there is substantial inter-surgeon variability in the manual selection of the AC and PC points, which complicates the creation of atlases. Indeed, errors in the localization of the AC and PC points in the atlases produce prediction errors independent of the registration accuracy. To minimize the effect of localization errors in the atlases, two senior neurosurgeons were asked to carefully select AC and PC on each of the atlases without any time constraints. For each atlas, the reference AC and PC points were computed as the average of the selections by the two neurosurgeons.

Evaluating accuracy of automatic AC and PC predictions against manual selections by 43 neurosurgeons on the two MRI volumes from the previous study

On the two MRI patient volumes used in the previous study on inter-surgeon variability in localizing the commissures, automatic atlas-based predictions of AC and PC were made using the method described above. Using the predicted AC and PC points STN, Vim and GPi were then indirectly localized in the two images based on the AC-PC coordinates in table 1. The automatic AC and PC predictions were evaluated against the median of the manual AC and PC selections by the 43 neurosurgeons. The accuracy of our indirectly computed coordinates of STN, Vim and GPi based on atlas-predicted AC and PC were evaluated against the median of the computed coordinates of the same targets based on the 43 manual AC and PC selections. The atlas prediction accuracy was compared with the mean manual accuracy of the surgeon selections.

Evaluating accuracy of automatic AC and PC predictions against clinical selections

The automatic predictions of AC and PC points were evaluated against clinical manual selections on 60 DBS patients. Thirty of these patients were operated on by one neurosurgeon and thirty by the other. The pre-operative plans for these patients, which included clinical manual selection of AC and PC points, were generated by the neurosurgeon that performed the procedure. These clinical manual selections of the AC and PC points will be referred to as clinical selections. For each patient, using the pre-operative MRI scan of the head, automatic predictions of AC and PC were generated using the individual atlases and the multiple-atlases-based methods described earlier. The accuracy of atlas-based automatic predictions (individual atlas as well as multiple-atlases-based) was evaluated by measuring the Euclidian distance between the automatic predictions and clinical selections.

Need for a standard to evaluate AC and PC prediction accuracy

Planning for a DBS procedure is typically performed under time constraints. This introduces inaccuracies. Thus, the clinical selections of AC and PC may not always be absolutely accurate. Consequently, measuring the distances between atlas-based predictions and clinical selections will not be conclusive in determining the accuracy of atlas-based predictions. To address this issue, a gold standard needs to be defined to which automatic AC and PC predictions and manual clinical selections can be compared.

Creation of the gold standard to evaluate prediction accuracy

To create the AC and PC gold standards, the following method was followed. Due to the time consuming nature of this method, 20 patients were selected out of the 60 patients used in this study. First, 10 of the 30 patients operated on by one of the neurosurgeons and 10 of the 30 patients operated on by the other neurosurgeon were selected randomly. Each of these patients already had AC and PC selected clinically by the operating neurosurgeon at the time of surgical planning. On these 20 volumes, both neurosurgeons were asked to carefully select AC and PC points in the laboratory without time constraints, using the same software tool that was used to create the atlases. Localization was performed independently by both neurosurgeons and they did not have access to the points that were selected by them clinically. This experiment created two new sets of AC and PC selections (one per neurosurgeon) on each of the 20 patients. These new selections can be considered to be the best achievable manual selections, henceforth referred to as the silver standards (SlvStd1 and SlvStd2). The average of the two silvers standards on a given patient is the gold standard for that patient.

Statistical Analysis

The accuracy of various selection methods was computed by comparing the distances between the selections and the corresponding reference points. Comparisons between these distances were conducted with a Wilcoxon signed-rank test to account for dependency between the values observed on the same patient. The Wilcoxon signed-rank test is a non-parametric statistical hypothesis test for the case of two related samples or repeated measurements on a single sample. It is used as an alternative to the paired Student's t-test when the population cannot be assumed to be normally distributed. The distances were summarized with the median and the lower and upper quartiles. R version 2.7.0 [71] was used for all statistical analyses.

III.3 Results

III.3.1 Validation against manual selections by a 43 neurosurgeons in two datasets

Quantitative results for prediction accuracy of AC, PC and MC and for the computed coordinates of STN, Vim and GPi based on the predicted commissures against the medians of the corresponding clusters based on the manual selections of AC and PC by the 43 neurosurgeons (ground truth) are given in table 4. This work was published in [60].

Table 4. Distances between the atlas-based AC, PC and MC predictions, the computed coordinates of STN, Vim and GPi based on the predicted commissures, manual AC and PC selections by 43 neurosurgeons and the computed coordinates of MC, STN, Vim and GPi based on the manually selected commissures from the respective ground truths for (a) Patient1 and (b) Patient2.

Accuracy (mm) with respect to median of 43 surgeon selections						
	(a) Patient1					
	AC	PC	MC	STN	Vim	GPi
Atlas	0.48	0.74	0.17	0.45	0.85	0.47
Manual	1.25	1.42	0.91	1.55	1.66	1.90
	(b) Patient2					
	AC	PC	MC	STN	Vim	GPi
Atlas	0.54	0.63	0.27	0.24	0.44	0.10
Manual	1.01	1.27	0.80	0.90	1.11	0.95

III.3.2 Validation against manual selections by two neurosurgeons in 60 patients in a clinical setting

Comparing single- and multiple-atlases-based predictions to clinical selections

The accuracy of the average of multiple-atlases-based predictions as well as of multiple-atlases-based predictions using STAPLE was evaluated with respect to clinical selections. These two methods of combining predictions were not statistically different for AC (p = 0.48) and MC (p = 0.49). For PC the average method produced smaller prediction error with respect to the clinical selection than the STAPLE method on 41 among the 60 patients (68%). This difference at PC was statistically significant ($p < 0.001$) based on a Wilcoxon signed-rank test, which takes into account the rank (1 or 2) within the pair (average and STAPLE) for each patient. The mean difference, however, is only 0.037 (95% Confidence Interval: 0.014 to 0.090). But, the average method led to large errors in one patient because one of the atlases registered poorly to this image volume. In this patient, the error using the average method was 8.40 mm at AC and 2.16 mm at PC while the error using the STAPLE for the same patient was 0.57 mm at AC and 0.93 mm at PC. Because the difference in accuracy between the STAPLE and the simple averaging method is very small and because the STAPLE method is better at eliminating outliers, it has been used in the rest of this study. Table 5 summarizes the prediction errors for individual atlases and for multiple-atlases-based prediction using STAPLE with respect to clinical selections on 60 patients. The median error with the lower and upper quartile values are provided. The p-values comparing the prediction errors of individual atlas predictions with those of multiple-atlases-based predictions using STAPLE are also given. Superiority of the multiple-atlases-based method using STAPLE is highly statistically significant over atlas 1 for AC and MC, and over atlases 2, 3, and 4 for PC.

Comparison of the atlas-based predictions and clinical selections against silver standards

Figure 5 shows representative results for the selection of AC. It shows the STAPLE based atlas prediction (1), the gold standard (2) defined as the average between the careful selections by the two neurosurgeons (silver standards) (4) and the clinical selection (3), projected on the sagittal (left panel) and axial (right panel) slice passing through the gold standard point.

Table 6 summarizes distances between pairwise combinations of multiple-atlases-based automatic predictions, clinical selections and the two silver standards. It reports, for AC, PC and MC, the median and the lower and upper quartiles of the Euclidian distance in millimeter, between (a) the two silver standards (careful manual selections by the two surgeons), (b-c) the STAPLE based atlas predictions and the two silver standards, and (d-e) the clinical points and the two silver standards. The silver standards comparison (a) reflects the inter-surgeon variability while carefully selecting the points manually.

Table 5. The errors (mm) of individual atlas predictions as well as of multiple-atlases-based predictions using STAPLE with respect to clinical selections in 60 patient volumes are summarized with the medians (lower quartile, upper quartile). The p-values of Wilcoxon signed-rank test comparing the STAPLE based prediction errors and individual atlas-based predictions errors with respect to clinical selections are shown.

	Multiple-atlases-based prediction using STAPLE	Atlas1-based prediction	Atlas2-based prediction	Atlas3-based prediction	Atlas4-based prediction
AC	1.07 (0.70, 1.43)	1.21 (1.02,1.69) $p < 0.001$	1.04 (0.69,1.42) $p = 0.95$	1.03 (0.68,1.48) $p = 0.15$	1.21 (0.70,1.52) $p = 0.02$
PC	0.94 (0.66,1.21)	1.02 (0.72,1.39) $p = 0.52$	1.03 (0.71,1.38) $p = 0.008$	1.10 (0.70,1.58) $p = 0.008$	1.11 (0.76,1.39) $p < 0.001$
MC	0.82 (0.55,1.14)	1.06 (0.78,1.32) $p < 0.001$	0.91 (0.55,1.29) $p = 0.05$	0.87 (0.55,1.22) $p = 0.36$	0.83 (0.64,1.13) $p = 0.10$

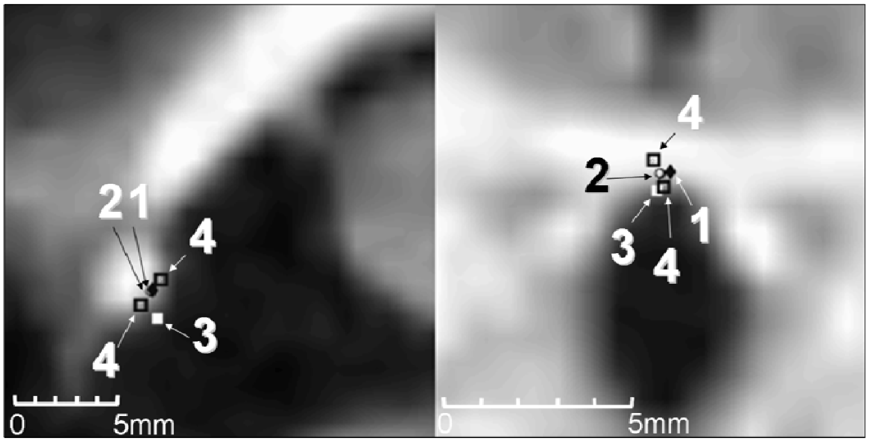

Figure 5. Representative AC selections. The figure shows (1) the STAPLE based prediction using multiple atlases, (2) the gold standard, (3) the clinical selection and (4) the careful selections by the two neurosurgeons, projected on the sagittal (left panel) and axial (right panel) slices passing through the gold standard point.

The p-values comparing (a) with (b, c, d and e) using Wilcoxon signed-rank tests are also reported in Table 6. The differences between clinical selections and the silver standards were statistically significant, thus indicating that clinical selection is sub-optimal. On the contrary, no statistical significance was found for the difference between the two silver standards (a) and that between STAPLE based atlas predictions and silver standards (b and c). Although, no conclusion can be drawn from large p-values, based on these findings, it may be conjectured that the atlas-based predictions are similar to an experienced neurosurgeon carefully selecting the points manually.

Table 6. Median (lower quartile, upper quartile) of the Euclidian distances between various types of selections; namely, silver standards (SlvStd1 and SlvStd2), multiple-atlases-based predictions using STAPLE (Atlas) and clinical selections, of the AC, PC and MC points over 20 patient volumes. Distances in columns (b – e) are compared to distances in (a) using a Wilcoxon signed-rank tests, and the corresponding p-values are shown in the cells.

	SlvStd1 vs. SlvStd2 (a)	SlvStd1 vs. Atlas (b)	SlvStd2 vs. Atlas (c)	SlvStd1 vs. Clinical (d)	SlvStd2 vs. Clinical (e)
AC	0.56 (0.44,0.87)	0.82 (0.57,0.92) p = 0.048	0.59 (0.43,0.92) p = 0.220	1.19 (1.00,1.57) p < 0.001	1.29 (0.89,1.60) p = 0.001
PC	0.55 (0.38,0.91)	0.63 (0.45,0.97) p = 0.598	0.57 (0.42,0.80) p = 0.812	1.08 (0.97,1.27) p = 0.001	1.00 (0.79,1.19) p = 0.030
MC	0.51 (0.34,0.58)	0.43 (0.33,0.50) p = 0.890	0.52 (0.27,0.64) p = 0.667	0.72 (0.60,1.14) p < 0.001	0.98 (0.72,1.30) p < 0.001

Accuracy of atlas-based predictions and clinical selections against gold standards

Table 7 summarizes the key findings of the study. It shows for the 20 volumes for which the AC and PC gold standards were available, the median Euclidean distances with the lower and upper quartiles, in millimeter, between (a) the automatic predictions and the gold standards, and (b) the clinical selections and the gold standards. These numbers are reported for the AC, PC and MC points. With respect to the gold standard, the median distances of atlas predictions are only about half of that of clinical selections. Highly statistically significant differences were found between the accuracy of atlas predictions and that of the clinical selections with respect to the gold standards for AC ($p = 0.007$), PC ($p < 0.001$), and MC ($p < 0.001$). The results also show that atlas-based predictions are significantly more accurate than clinical selections with respect to the gold standard.

Finally, 95% confidence intervals of the median accuracy of atlas-based predictions with respect to the gold standards are (0.56, 0.79), (0.46, 0.66) and (0.33, 0.50) mm, respectively for the AC, PC and MC. For the accuracy of clinical selections with respect to gold standards the 95% confidence intervals are (0.91, 1.47), (0.82, 1.26) and (0.68, 1.20) mm respectively for AC, PC and MC.

Table 7. Median (lower quartile, upper quartile) of the Euclidian distances between gold standards, clinical selections (Clinical), and multiple-atlases-based predictions using STAPLE (Atlas) for AC, PC, and MC points over 20 patient volumes. Distances shown in column (a) and (b) are compared using a Wilcoxon signed-rank tests, and the corresponding p-values are given.

	Atlas vs. Gold Standard (a)	Clinical vs. Gold Standard (b)
AC	0.65 (0.53,0.84)	1.21 (0.74,1.56) $p = 0.007$
PC	0.56 (0.42,0.70)	1.06 (0.81,1.25) $p < 0.001$
MC	0.41 (0.29,0.53)	0.84 (0.62,1.11) $p < 0.001$

Figure 6 shows the cumulative distributions of the differences between atlas predictions and clinical selections with respect to the gold standard over the 20 volumes. The horizontal axis represents the distance in mm between selections of a point (AC, PC or MC) using two different methods. The vertical axis represents the fraction of cases for whom the distance between the selections was less than or equal to the corresponding distance on the horizontal axis. Figure 6(a) shows that in about 80% of the cases the distance between atlas predictions and gold standard for AC is less than 1.0 mm which is true in only 25% of cases for the clinical selections. Figure 6(b) shows similar results for the PC. Figure 6(c) shows that in 100% of the cases the distance between atlas predictions and the gold standard for MC is sub-millimetric while it is only true in about 70% of the cases for the clinical selections. This figure also shows that manual selection can lead to relatively large errors in the selection of the MC, which is commonly used as the center of the coordinate system in stereotactic surgeries.

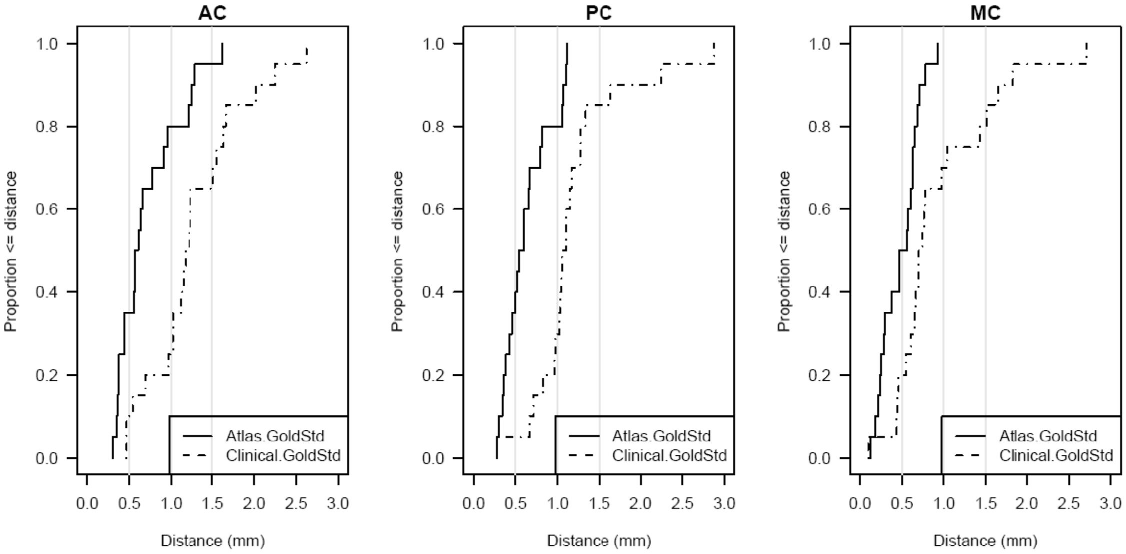

Figure 6. Cumulative distributions of the Euclidian distances between multiple-atlases-based predictions using STAPLE and gold standards (solid line) as well as between the gold standards and the points chosen clinically (dotted line) for (a) AC, (b) PC and (c) MC on 20 patients.

III.4 Discussion and Conclusions

The previous chapter showed that there was substantial inter-surgeon variability in the manual selection of AC and PC and that this had a substantial impact on AC-PC based manual localization of targets. In this chapter, an atlas-based technique [34] was applied to predict the commissures and the accuracy of the method was validated by comparing the predictions against careful manual selections by a large number of neurosurgeons, and against selections made in a clinical setting as well as against gold standards created in a non-clinical setting.

The results in this chapter demonstrate that by carefully creating atlases containing AC and PC selections and by combining predictions from multiple atlases, a system can be developed that is not only fully automatic but also produces results that are more accurate and reproducible than those obtained by experienced physicians in clinical practice. The error distribution shows that in most cases, the accuracy of the predictions is as good as what is achievable with the resolution of clinically acquired images. The statistical analysis shows a slight gain in performance when using more than one atlas. With current computer speeds and multi-core processors, multiple-atlas approaches are thus recommended. When the registrations were reasonable, the STAPLE-based approach used to weigh more those atlases that registered well did not produce statistically better predictions than the average of the multi-atlas predictions. However, when atlases registered poorly to a patient's images the STAPLE-based approach was able to eliminate the contribution of those atlases that registered poorly.

With respect to the median of the manual selection by 43 neurosurgeons from multiple centers, the atlas-based predictions were sub-millimetric for AC, PC, MC, STN, Vim and GPi on both the datasets. With respect to the gold standard built under laboratory controlled setting, the accuracy of AC, PC and MC predictions was sub-millimetric (0.65 mm, 0.56 mm and 0.41 mm for AC, PC and MC respectively) on 20 datasets. In a clinical setting, multiple-atlas-based prediction accuracy over 60 patients between 2 neurosurgeons was 1.07 mm, 0.94 mm and 0.82 mm for AC, PC and MC respectively. Comparing the careful manual selection by 2 neurosurgeons, their clinical selections and atlas-based predictions suggests that the atlas-based predictions are similar to an experienced neurosurgeon carefully selecting the points manually. Thus, an atlas-based technique was applied to standardize automatic selection of the commissures. Using a number of validation schemes it was shown that automatic selection of AC and PC with sub-millimetric accuracy and better than clinical selection by neurosurgeons is possible. Using such an approach, variability in communicating targets based on AC-PC can be reduced. This also directly impacts the accuracy of atlases that use AC-PC based normalization methods to populate statistical data from patients.

CHAPTER IV

A NEW KERNEL TO BUILD STATISTICAL MAPS OF STIMULATION RESPONSE

Abstract

Statistical maps of stimulation responses acquired during DBS surgeries have been built in the past by a number of groups including ours. More importantly, attempts have been made to use such maps to provide assistance to the surgical team. However, there is a problem with the way stimulation responses are modeled in these methods for building the maps. In this chapter, first a limitation of the model that has been used in the past is described. Second, a new model is proposed to overcome this limitation and maps generated by the two models are compared.

This work was published in Lecture Notes in Computer Science in the proceedings of Medical Image Computing and Computer Assisted Intervention (LNCS, MICCAI), 2008 [49].

IV.1 Introduction

As described in section I.3, a number of functional atlases and databases containing sub-cortical electrophysiological data of stimulation responses have been developed. Such data are typically acquired intra-operatively during the DBS procedure. In the past, our group has shown how a statistical map of stimulation response observations could be created [72, 73] by combining Gaussian (GAUSS) kernels centered at every location where stimulation response was recorded. Guo et al. [37] also built stimulation response maps using this method and used them for automatic target planning. For a given stimulation response observation, the Gaussian kernel model assigns the highest likelihood of producing the response to the location of the stimulation point itself and lower values to points further away from it. Also, the support of the kernel is made proportional to the stimulation amplitude. This means that the likelihood values at and around a stimulation point are higher if the response was observed at lower stimulation amplitude than if the response was observed at higher stimulation amplitude. Some other groups have also used this approach [37, 74]. However, the method used to build these maps has certain drawbacks as discussed below.

Figure 7 shows in one-dimension two Gaussian kernels centered at two stimulation points D_1 and D_2 where responses were observed at low amplitudes. Response at a low amplitude means that the region likely to have produced the response was located close to the stimulation point itself. Summing the two kernels in figure 7 produces two regions of high likelihood, one centered at D_1 and the other at D_2.

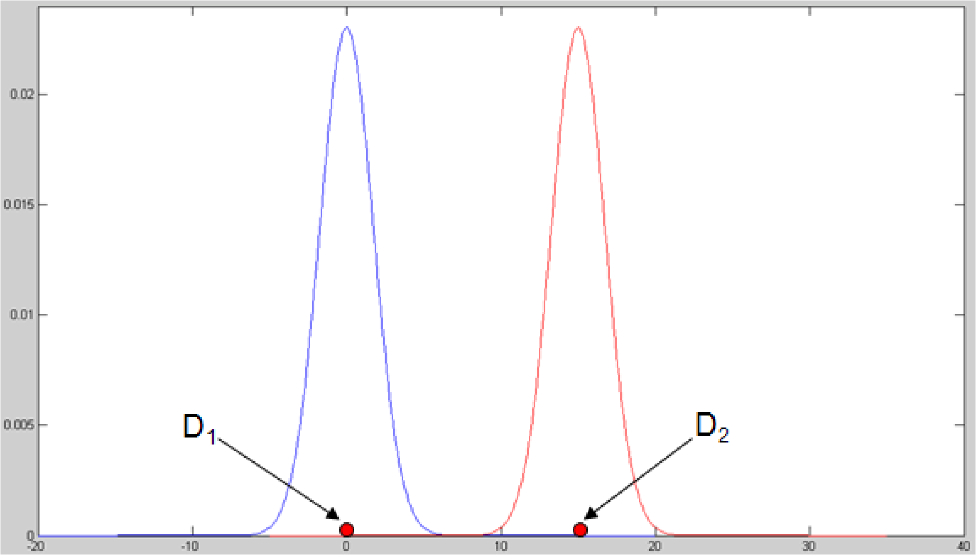

Figure 7. Gaussian kernels centered at two stimulation points D_1 and D_2 where stimulation responses were observed at low stimulation amplitudes.

However, there is a potential problem with this method. Consider the same two stimulation points D_1 and D_2 but with the same responses observed at higher stimulation amplitudes. The Gaussian kernels thus have larger supports as shown in figure 8(a). Since the responses were observed at higher stimulation amplitudes, the regions whose stimulation produced the responses are likely to be located further away from the stimulation points themselves. Let us assume for the sake of argument that this region is in between the stimulation points as shown by the dotted box in figure 8(a). This means that this region should be assigned higher likelihood of producing the response than the stimulation points themselves. However, summing the Gaussian kernels results in a function that assigns relatively smaller likelihood values to the region in between the two stimulation points than those at the points themselves as shown in figure 8(b).

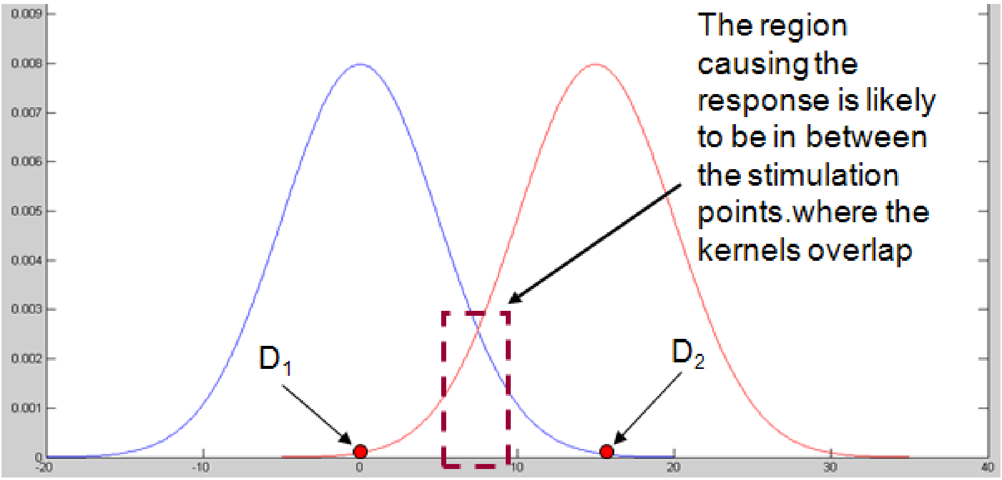

(a)

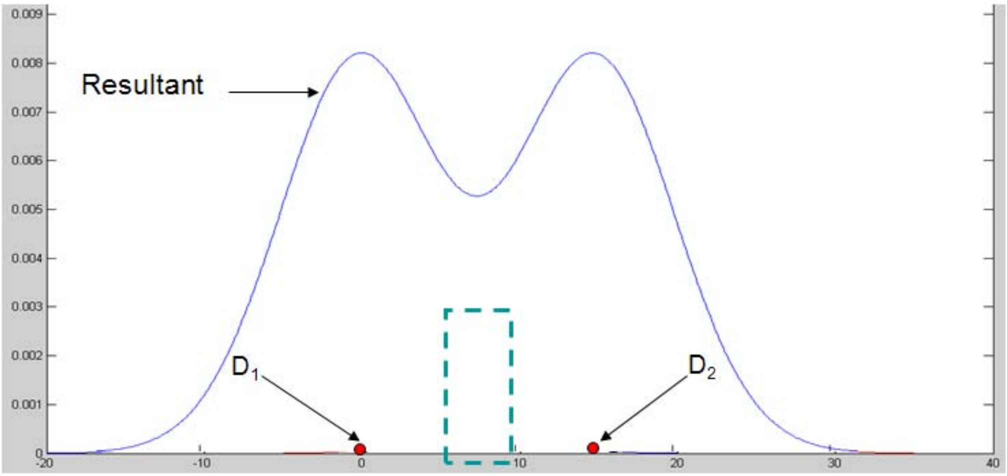

(b)

Figure 8. (a) The same two stimulation points D_1 and D_2 shown figure 7 but with stimulation responses observed at higher stimulation amplitudes. Corresponding Gaussian kernels with larger standard deviations are centered at the points. The result of summing the kernels in (a) is shown in (b).

IV.2 Data and Method

At Vanderbilt, DBS surgeries are performed using a miniature stereotactic frame, the StarFix microTargeting Platform® (501(K), Number K003776, Feb. 23, 2001, FHC, Inc., Bowdoin, ME) instead of a standard stereotactic frame. During surgery, a micro-positioning drive (microTargeting® drive system, FHC Inc., Bowdoin, ME) is mounted on the platform. Recording and stimulating leads are then inserted through the guiding tubes. Details on the platform, including a study of its accuracy demonstrating it to be at least as accurate as standard frames can be found in [75, 76]. Recent work on the clinical accuracy of this platform after accounting for intra-operative brain shift can be found in [77]. Using this system, the location of every intra-operative data point was converted to X, Y, Z coordinates in the patient's CT image space. Stimulation response data include the location of each stimulation point, observed percentage reduction in symptoms or efficacy (recorded based on subjective assessment by a neurologist) and the associated stimulation current, observed adverse effect (if any) and the associated current. 1512 stimulation data points from 92 PD patients and 950 stimulation response data points from 43 ET patients were available. Of these, only those where at least 50% efficacy was observed were chosen as efficacy data points. Using this approach, 730 efficacy data points from 78 PD implantations (STN DBS) and 572 efficacy data points from 36 ET implantations (Vim DBS) were populated and projected onto an MRI atlas. An efficacy threshold of 50% was chosen in consultation with the surgical team as the minimum acceptable efficacy. Choosing a threshold was necessary to normalize the variability between neurologists in the subjective assessment of efficacy (e.g. an assessment of 70% by neurologist A may correspond to 50% by neurologist B).

IV.2.1 Spherical shell kernel

To address the problem shown in figure 8 and discussed in section IV.1, an alternative model is proposed based on the approach that is used in surgery to test for stimulation response. During the surgery, stimulation current is gradually increased in steps until a response is observed. If a response occurs at stimulation current I and not at the previous step I–ε, then it is intuitive to assume that the responsive neurons were activated between current amplitudes I–ε and I, where ε is a positive real number. Thus, it can be assumed that the responsive neurons lie in a region that is activated by current I but not by current I–ε. Assuming the activation field to be isotropic and the material properties of the brain to be homogeneous, this region would be an annulus in 2D or a spherical shell in 3D. Thus, a uniform probability density function is associated with the neurons in the spherical shell. Summing over a number of such spherical shell kernels and normalizing them yields a likelihood map of regions responsive to stimulation. The relationship used between stimulation current and the radius (R) of the spherical region of activated by it is based on the data published by Butson et al. [58] for monopolar stimulation using a DBS electrode with standard stimulator settings in an isotropic medium. Typical radii values are 2.2 mm for 1 mA, 2.6 mm for 1.5 mA, 3 mm for 2 mA. At our center, stimulation is applied in steps of 0.5 mA, but, in order to account for potential delay between the application of stimulation and the occurrence of response ε was chosen to be 1.

Specifically, let a patient P_1 have N_1 stimulation data points D_1, D_2, …, D_{N_1}. Let data point D_1 from patient P_1 be mapped to the location ($X_A^{P_1 D_1}$, $Y_A^{P_1 D_1}$, $Z_A^{P_1 D_1}$) in the atlas via non-rigid registration between the patient and atlas MRIs. If D_1 produces a stimulation response at I mA, the spherical shell kernel will have outer radius $r_1 = f(I)$ and inner radius $r_2 = f(I - 1)$, where f is the function that relates stimulation current to the radius of the spherical region activated by it. Let Ω_{P_1,D_1} be the set of all voxels inside the spherical shell due to data point D_1 from patient P_1 as defined in equation 1. Let Θ_{P_1,D_1} be the set of voxels inside the inner sphere (radius r_2) for data point D_1 as defined in equation 2. For data points $D_1, D_2, \ldots, D_{N_1}$ from patient P_1, let Θ_{P_1} be the set of all voxels in the inner spheres as defined in equation 3. $F'_{P_1,D_1}(x_A, y_A, z_A)$ represents the map value at point (x_A, y_A, z_A) in the atlas due to stimulation response data projected from data point D_1 of patient P_1 as defined in equation 4. The statistical map of stimulation response built by combining several data points from a population of patients using spherical shell kernels is represented by F^{SS}. The value of F^{SS} at any point (x_A, y_A, z_A) due to L patients $P_1, P_2, \ldots, P_L$ contributing $N_1, N_2, \ldots, N_L$ data points respectively is represented as $F^{SS}(x_A, y_A, z_A)$ and computed based on equation 5.

$$\begin{aligned}\Omega_{P_1,D_1} = \{(x_A, y_A, z_A) \in R^3 \mid \\ r_2^2 < (x_A - X_A^{P_1D_1})^2 + (y_A - Y_A^{P_1D_1})^2 + (z_A - Z_A^{P_1D_1})^2 \le r_1^2\}\end{aligned} \tag{1}$$

$$\Theta_{P_1,D_1} = \{(x_A, y_A, z_A) \in R^3 \mid (x_A - X_A^{P_1D_1})^2 + (y_A - Y_A^{P_1D_1})^2 + (z_A - Z_A^{P_1D_1})^2 \le r_2^2\} \tag{2}$$

$$\Theta_{P_1} = \Theta_{P_1,D_1} \cup \Theta_{P_1,D_2} \cup \ldots \cup \Theta_{P_1,D_{N_1}} \tag{3}$$

$$F'_{P_1,D_1}(x_A,y_A,z_A)=\begin{cases}\dfrac{1}{n(\{\Omega_{P_1,D_1}-\Theta_{P_1}\})} \\ when\,(x_A,y_A,z_A)\in\{\Omega_{P_1,D_1}-\Theta_{P_1}\}, \\ \\ 0 \; otherwise\end{cases} \quad (4)$$

$n(S)$ *is the number of elements in the set S*

$$F^{SS}(x_A,y_A,z_A)=\frac{1}{\sum_{i=1}^{L}N_i}\left(\sum_{i=1}^{L}\sum_{j=1}^{N_i}F'_{P_i,D_j}(x_A,y_A,z_A)\right) \quad (5)$$

IV.2.2 Gaussian smoothed spherical shell (GSSS) kernel

The problem with the spherical shell kernel is that it produces unrealistic maps which have numerous small fragments of high likelihood regions as shown in figure 9(b) for the organization of stimulation data points shown in figure 9(a). This shows that the constraint of the spherical shell model that none of the neurons in the inner sphere can produce the observed response is too strict. A possible scenario when some of the neurons inside the inner circle may be required is shown in figure 10. Therefore, it is not appropriate to assign zero likelihood of producing the stimulation response to the region inside the inner sphere.

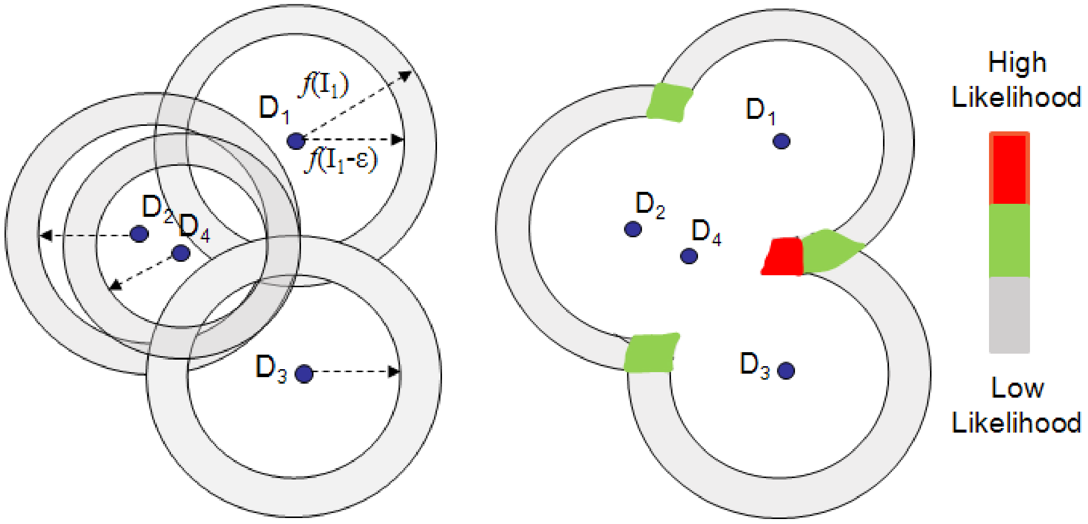

(a) (b)

Figure 9. (a) Organization of 4 stimulation data points D_1, D_2, D_3 and D_4 and their associated annulus kernels. *f* is the function that relates stimulation current to the radius of the region activated by it, and ε is a positive real number. (b) Resulting map built using the method based on the spherical shell described in section IV.2.1.

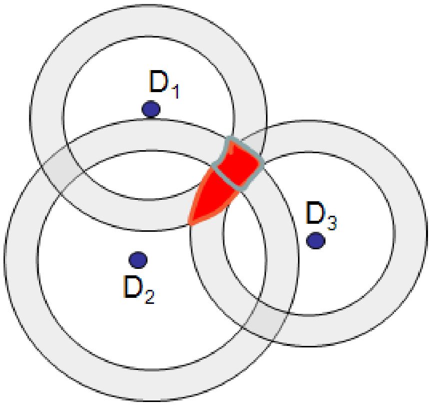

Figure 10. Problem with the spherical shell model assigning zero likelihood of producing a stimulation response to the region inside the inner sphere. The region producing the stimulation response is plausible to be the entire region shown in red. The map built using the spherical shell kernel would only include the intersection of the three kernels (the part of the red region outlined in gray).

To account for this, the spherical shell model is modified. It is smoothed by convolution with a Gaussian kernel. The standard deviation of the Gaussian kernel used for smoothing was chosen to be 0.5 mm (which approximately corresponds to the shell width for a 1 mA increment in stimulation current) and the support was made proportional to the stimulation current producing the stimulation response. The equations of the spherical shell model from section IV.2.1 change as follows by applying Gaussian smoothing by convolution with a 3D Gaussian kernel f_G. Let Ω_{P_1,D_1} be the set of all voxels inside the spherical shell due to data point D_1 from patient P_1 as defined in equation 1, where D_1 is a data point from patient P_1 mapped to the location ($X_A^{P_1 D_1}$, $Y_A^{P_1 D_1}$, $Z_A^{P_1 D_1}$) in the atlas. Equation 4 that defined the values of the spherical shell kernel F'_{P_1,D_1}, changes to F''_{P_1,D_1} defined in equation 6, where voxels of a spherical shell kernel lying inside the inner spheres of other spherical shell kernels are not eliminated. The Gaussian smoothed spherical shell kernel due to data point D_1 from patient P_1 is represented by $F^{GSSS}_{P_1,D_1}$ and defined in equation 7.

$$F''_{P_1,D_1}(x_A, y_A, z_A) = \left\{ \begin{array}{l} \dfrac{1}{n(\Omega_{P_1,D_1})} \\ when\ (x_A, y_A, z_A) \in \Omega_{P_1,D_1}, \\ \\ 0\ otherwise \end{array} \right\} \quad (6)$$

$$n(S)\ is\ the\ number\ of\ elements\ in\ the\ set\ S$$

$$F^{GSSS}_{P_1,D_1} = f_G * F''_{P_1,D_1} \quad (7)$$

Two-dimensional surface plots comparing the cross-sections from spherical shell and GSSS kernels are shown in figure 11.

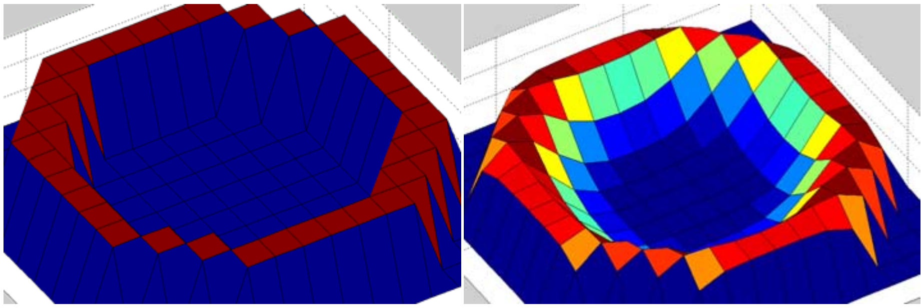

Figure 11. Two-dimensional surface plots comparing cross-sections from (a) spherical shell and (b) GSSS kernels.

The statistical map of stimulation response built by combining several data points from a population of patients using Gaussian smoothed spherical shell kernels is represented by F^{GSSS}. The value of F^{GSSS} at any point (x_A, y_A, z_A) due to L patients P_1, P_2, …, P_L contributing N_1, N_2, …, N_L data points respectively is represented as $F^{GSSS}(x_A, y_A, z_A)$ and computed based on equation 8.

$$F^{GSSS}(x_A, y_A, z_A) = \frac{1}{\sum_{i=1}^{L} N_i}\left(\sum_{i=1}^{L}\sum_{j=1}^{N_i} F_{P_i,D_j}^{GSSS}(x_A, y_A, z_A)\right) \quad (8)$$

IV.2.3 Comparing efficacy maps built using the previously used Gaussian kernel (GAUSS) and those built using the new Gaussian Smoothed Spherical Shell (GSSS)

Simulation

Figure 12(a) shows an example arrangement of three stimulation response data points. The spherical shell corresponding to the region activated by the amplitude producing the response and not by the previous no-response amplitude is shown for each data point.

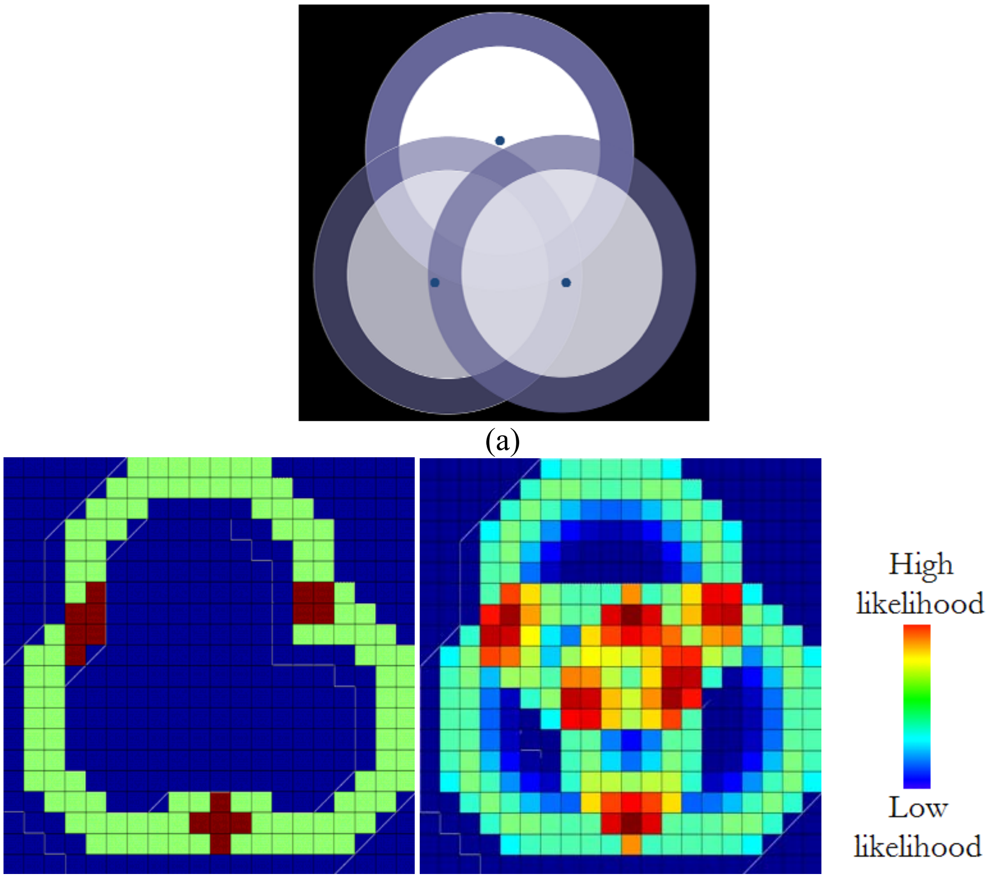

(a)

(b) (c)

Figure 12. (a) An example arrangement of three stimulation response data points with the corresponding spherical shells in 2D, (b) resultant map built by combining the spherical shells, (c) resultant maps built by combining the shells after Gaussian smoothing (GSSS).

The resultant maps based on combining the spherical shells without Gaussian smoothing (section IV.2.1) and with Gaussian smoothing (section IV.2.2) are shown in figure 12(b) and 12(c). Figure 12(b) shows an unrealistic map with the region common to the three data points being completely eliminated. On the other hand, the map built using the GSSS shown in figure 12(c) associates high likelihood with the common region and is more realistic.

Using real patient data

Statistical maps of efficacy were built using stimulation response data from PD (STN DBS) and ET (Vim DBS) patients using the previously used Gaussian (GAUSS) kernel as well as the proposed Gaussian Smoothed Spherical Shell (GSSS) kernel. The average of surgical electrode placement positions in a population of patients was taken as the ground truth referred to as the mean Intra-Operative Implant Position (IOIP). The centroids of the high likelihood regions for the efficacy maps generated using the two kernels were compared against it. The high likelihood region (HLR) of a map is defined as the region of the map containing voxels with values at least 70% of the maximum map value. This pipeline is shown in figure 13.

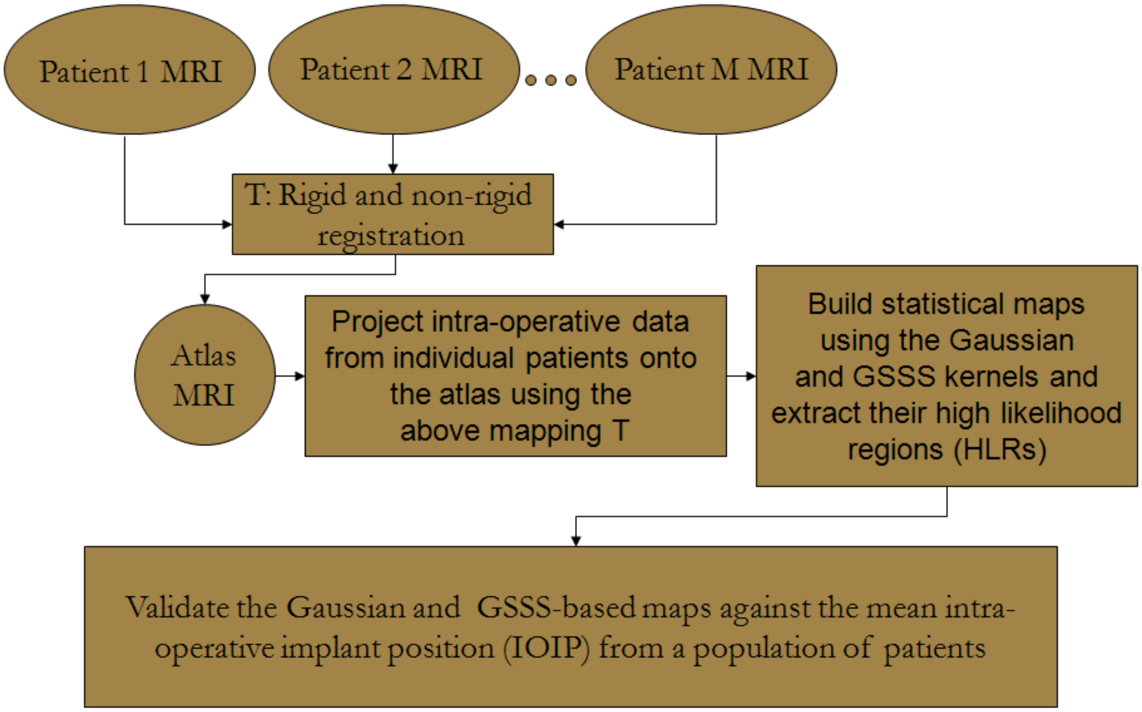

Figure 13. Pipeline to build statistical maps on an electrophysiological atlas using the Gaussian- and GSSS-based kernels and comparing them against the mean intra-operative implant position from a population of patients.

IV.3 Results

The PD and ET efficacy maps were overlaid on the MRI atlas and visualized along with the corresponding mean IOIP in a population of patients (ground truth). The results are shown in figures 14-16 below. Figure 14(a) shows that the centroid of the HLR of the PD efficacy map for the right side built using the new GSSS kernel is in close proximity to the ground truth. On the other hand, figure 14(b) shows that the HLR of the GAUSS-kernel-based PD efficacy map is further away from the ground truth. Similar results can be seen in figure 15 (left brain PD), figure 16 (right brain ET) and figure 17 (left brain ET).

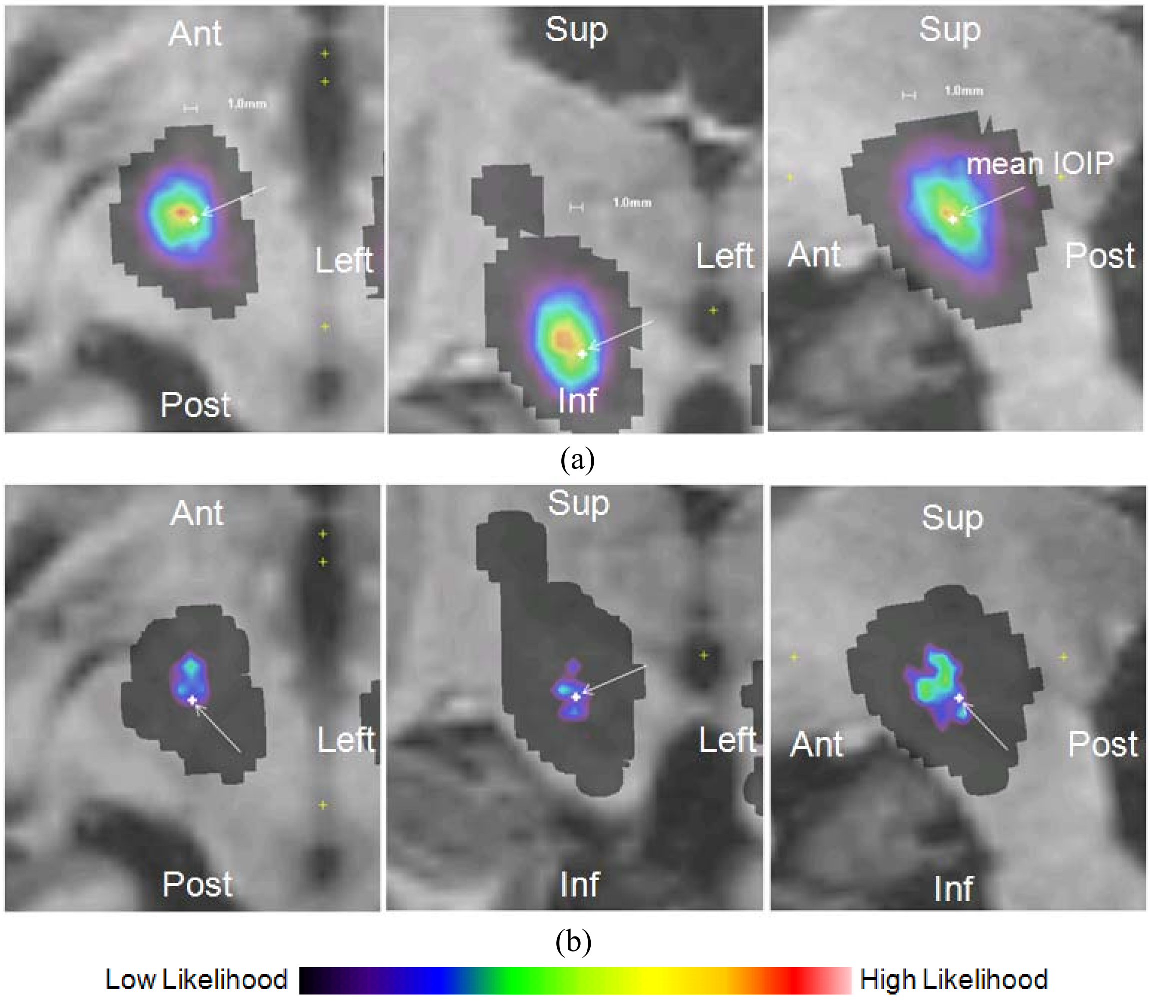

(a)

(b)

(c)

Figure 14. Axial, coronal and sagittal slices of PD efficacy maps for the right side built using (a) GSSS kernel and (b) GAUSS kernel, overlaid on the MRI atlas. (c) Color scale for the likelihood values. The mean IOIP (ground truth) is shown as a white crosshair.

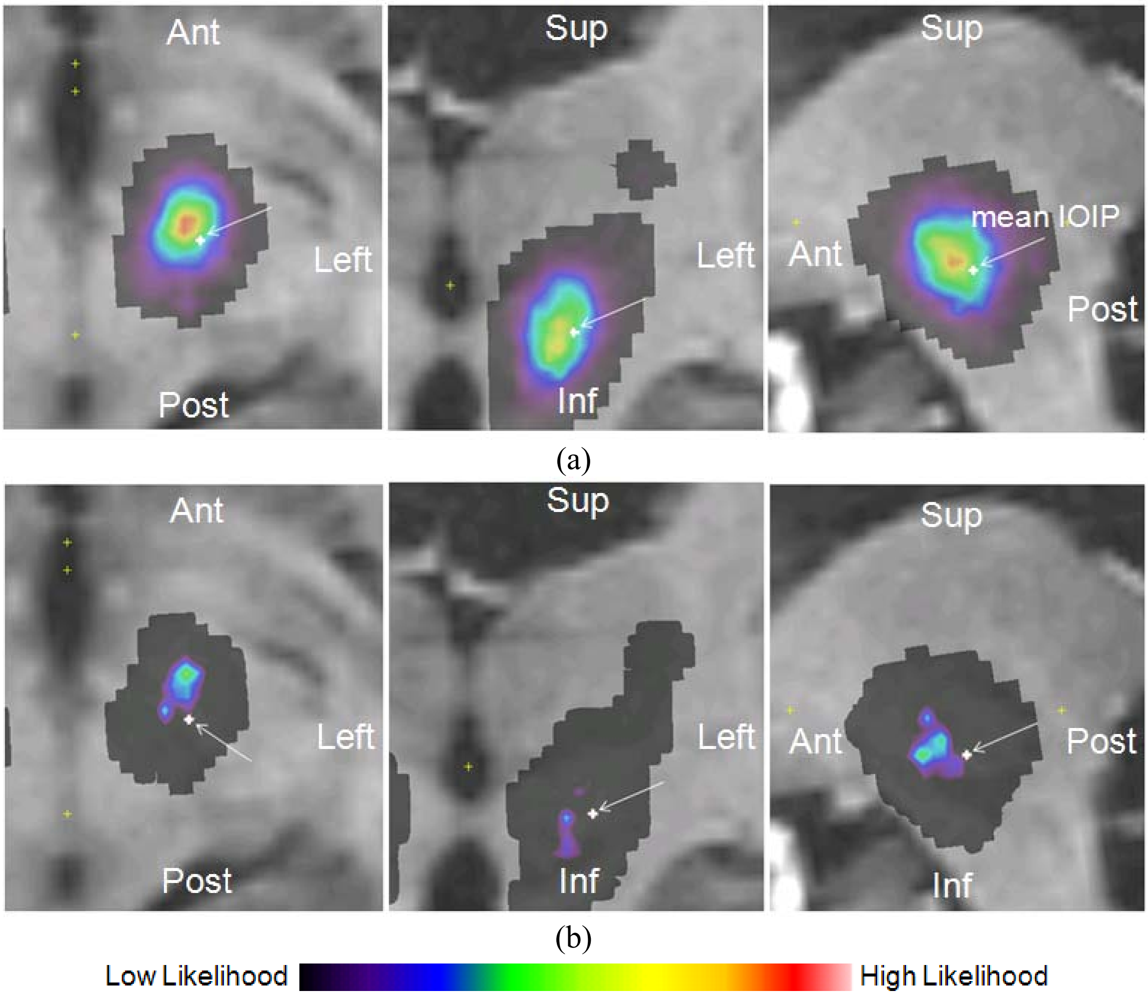

(a)

(b)

(c)

Figure 15. Axial, coronal and sagittal slices of PD efficacy maps for the left side built using (a) GSSS kernel and (b) GAUSS kernel, overlaid on the MRI atlas. (c) Color scale for the likelihood values. The mean IOIP (ground truth) is shown as a white crosshair.

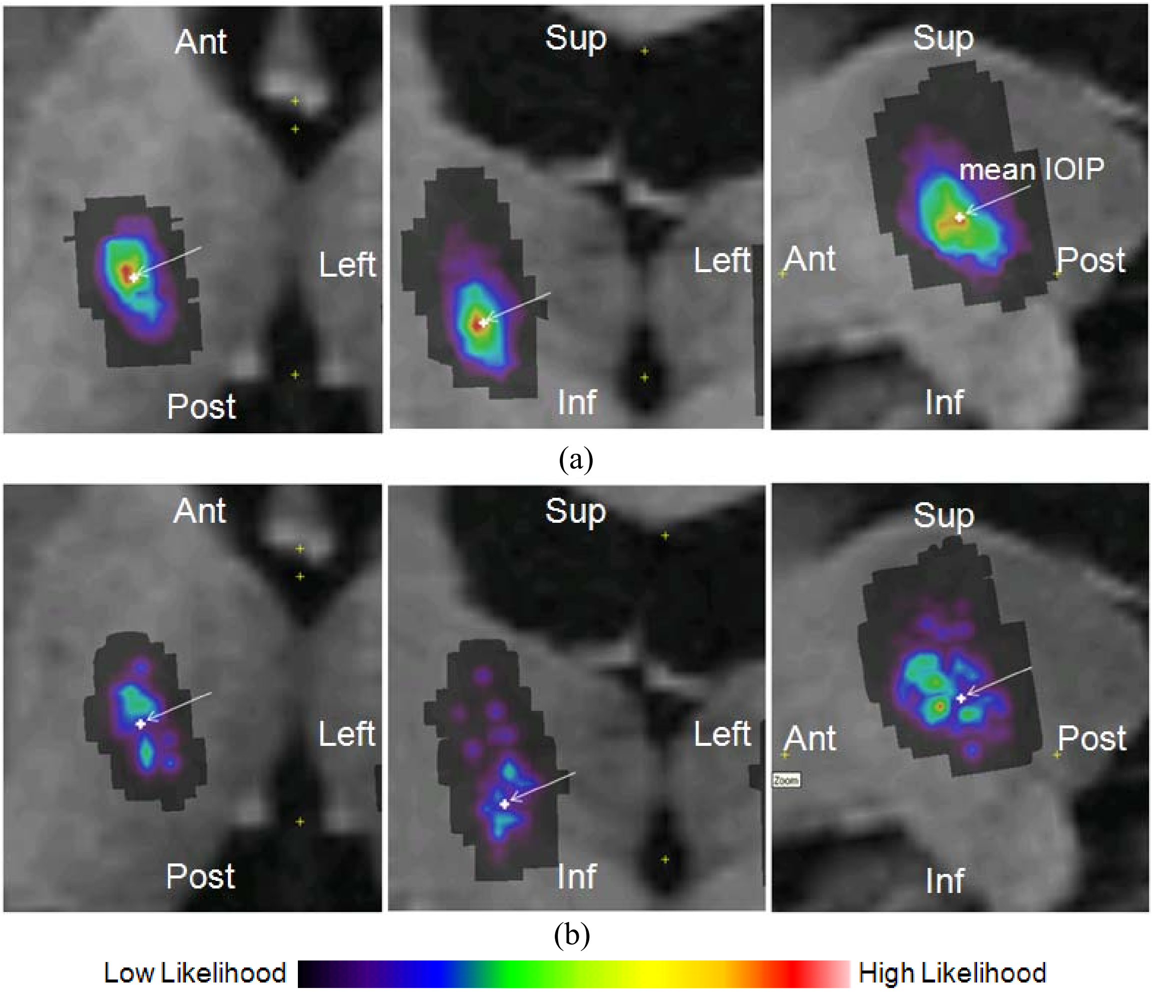

(a)

(b)

(c)

Figure 16. Axial, coronal and sagittal slices of ET efficacy maps for the right side built using (a) GSSS kernel and (b) GAUSS kernel, overlaid on the MRI atlas. (c) Color scale for the probability values. The mean IOIP (ground truth) is shown as a white crosshair.

The AC-PC coordinates (in mm) of the mean IOIPs and the centroids of the corresponding efficacy maps for and the distances between them are shown in table 8. The GAUSS-kernel-based maps produce multiple high likelihood regions. These are denoted as Region1, Region2 and so on. Table 8 shows that the centroids of the HLRs of the old GAUSS-kernel-based maps were further away from the corresponding mean IOIPs than were the HLR centroids for the new GSSS-kernel-based maps. The table also shows that the GAUSS-kernel-based maps produced multiple HLRs as shown in figure 18.

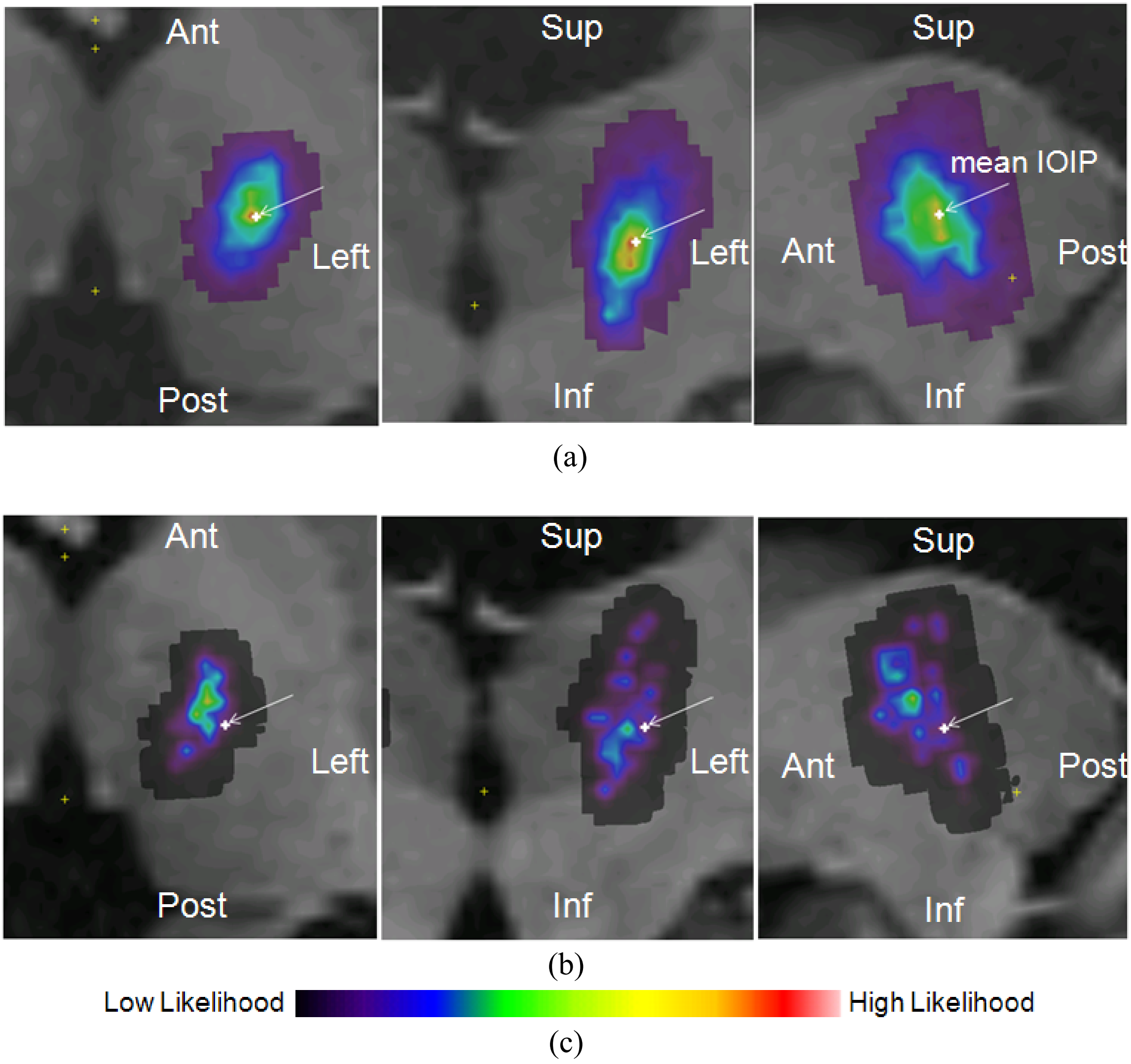

Figure 17. Axial, coronal and sagittal slices of ET efficacy maps for the left side built using (a) GSSS kernel and (b) GAUSS kernel, overlaid on the MRI atlas. (c) Color scale for the probability values. The mean IOIP (ground truth) is shown as a white crosshair.

Table 8. AC-PC coordinates (in mm) of the mean IOIPs and the centroids of the HLRs of the GAUSS- and GSSS-kernel-based efficacy maps, and the distances between them. GAUSS-kernel-based maps produce multiple HLRs (Region1, Region2, etc).

		Left	Anterior	Inferior	Distance from mean IOIP
mean IOIP	LSTN	10.28	-3.35	3.86	0.00
GAUSS	LSTN	9.99	0.35	3.67	3.72
GSSS	LSTN	9.37	-2.07	3.67	1.58

		Left	Anterior	Inferior	Distance from mean IOIP
mean IOIP	RSTN	-10.92	-2.41	3.53	0.00
GAUSS (Region1)	RSTN	-11.05	-0.28	2.64	2.31
GAUSS (Region2)	RSTN	-11.05	-1.34	1.01	2.74
GSSS	RSTN	-11.98	-1.83	3.03	1.31

		Left	Anterior	Inferior	Distance from mean IOIP
mean IOIP	LVim	13.51	-5.15	-5.38	0.00
GAUSS (Region1)	LVim	11.05	-4.32	-4.41	2.77
GAUSS (Region2)	LVim	12.00	-3.27	-4.91	2.45
GAUSS (Region3)	LVim	12.15	-6.22	-4.45	1.96
GAUSS (Region4)	LVim	11.07	-2.87	-1.04	5.47
GAUSS (Region5)	LVim	13.94	-2.87	-7.93	3.45
GAUSS (Region6)	LVim	10.99	-3.41	-7.16	3.54
GSSS	LVim	13.18	-5.21	-4.64	0.81

		Left	Anterior	Inferior	Distance from mean IOIP
mean IOIP	RVim	-13.44	-3.30	-4.67	0.00
GAUSS (Region1)	RVim	-13.44	-1.61	-4.09	1.78
GAUSS (Region2)	RVim	-13.27	-1.22	-5.95	2.44
GAUSS (Region3)	RVim	-14.28	-0.37	-6.49	3.55
GSSS	RVim	-13.97	-2.85	-4.32	0.77

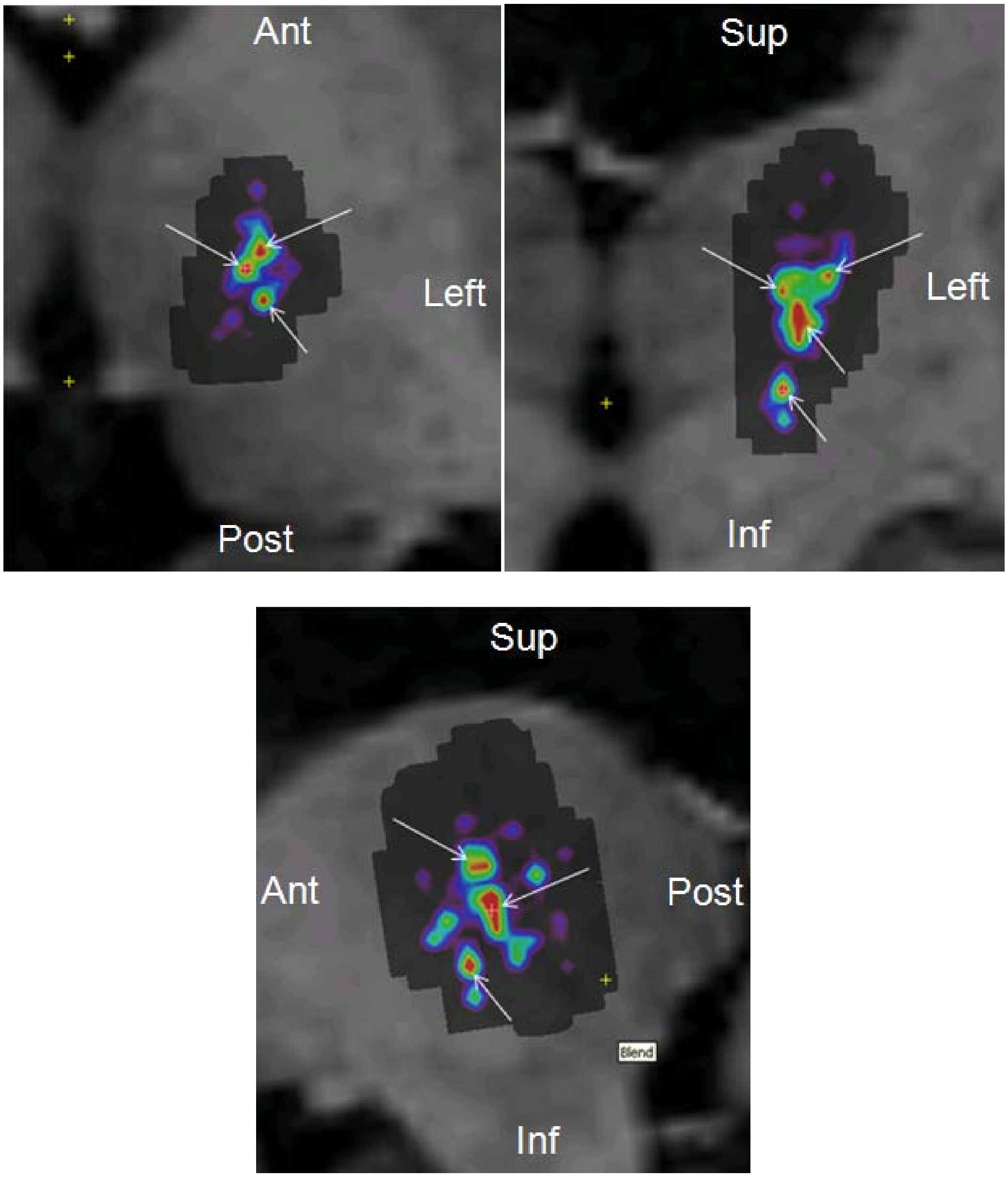

Figure 18. Axial, coronal and sagittal slices of the Vim efficacy map built using the GAUSS kernel show disconnected high likelihood regions.

Furthermore, table 8 shows that all of the multiple HLRs of the old GAUSS-kernel-based maps were farther from the corresponding mean IOIP than were the HLRs of the new GSSS-kernel-based maps. Specifically, the centroid of the high likelihood region (HLR) of the proposed GSSS-kernel-based PD efficacy map for the left side was 1.58 mm away from the mean IOIP while that of the old GAUSS-kernel-based PD efficacy map was 3.72 mm away. For the right side, the HLR centroid of the GSSS-kernel-based PD efficacy map was 1.31 mm away while the GAUSS-kernel-based PD efficacy map for the right side produced two HLRs which were on average 2.53 mm (SD 0.3 mm, maximum 2.74 mm) away from the corresponding mean IOIP. The HLR centroid of the GSSS-kernel-based ET efficacy map for the left side was 0.81 mm from the mean IOIP while the GAUSS-kernel-based ET efficacy map for the left side produced six HLRs which were on average 3.27 mm (SD 1.23 mm, maximum 5.47 mm) away from the corresponding mean IOIP. The HLR centroid of the GSSS-kernel-based ET efficacy map for the right side was 0.77 mm from the mean IOIP while the GAUSS-kernel-based ET efficacy map for the right side produced three HLRs which were on average 2.59 mm (SD 0.9 mm, maximum 3.55 mm) away from the corresponding mean IOIP.

IV.4 Discussion and Conclusions

The idea of using no-response-points (NRPs) was also investigated in this study and is discussed here. When application of stimulation at a point from 0 mA to the maximum amplitude applicable by the stimulator does not produce any response that data point is referred to as no-response-point. It was deemed logical that the maps could be further refined by using such information. For example, using data points where no efficacy was observed, efficacy maps may be trimmed. Similarly, using data points where no adverse effects were observed, adverse effect maps may be trimmed.

Specifically, let a patient P_1 have N_1 efficacious stimulation data points D_1, D_2, …, D_{N_1} as noted earlier. Let P_1 also have NE_1 no-efficacy data points Q_1, Q_2, …, Q_{NE_1}. If Q_1

was stimulated up to I_{Q_1} mA, then the corresponding radius of activated spherical region would be $r_{Q_1} = f(I_{Q_1})$ where f is the function referred earlier that relates stimulation amplitude to radius of the activated spherical region. Let the coordinates of Q_1 mapped to the atlas be $(X_A{}^{P_1Q_1}, Y_A{}^{P_1Q_1}, Z_A{}^{P_1Q_1})$. Equation 9 defines Ψ_{P_1,Q_1} as the set of voxels in the atlas activated by the maximum stimulation applied at Q_1. Let the no-efficacy-mask Ψ_{P_1} defined in equation 10 be the set all voxels in the region activated by all no-efficacy stimulation points in patient P_1. The set of points in the "trimmed" spherical shell due to efficacious stimulation at D_1 and the no-efficacy mask Ψ_{P_1} is $\Omega T_{P_1,D_1}$ defined in equation 11. $FT'_{P_1,D_1}(x_A, y_A, z_A)$ represents the map value at point (x_A, y_A, z_A) in the atlas due to efficacious stimulation response data point D_1 from patient P_1 after voxels overlapping with the no-efficacy mask have been eliminated from map-building. This is defined in equation 12. FT_{P_1,D_1} represents the trimmed kernel after Gaussian smoothed by convolution with f_G and its value at any point (x_A, y_A, z_A) in the atlas is defined in equation 13.

$$\Psi_{P_1,Q_1} = \{(x_A, y_A, z_A) \in R^3 \mid (x_A - X_A{}^{P_1Q_1})^2 + (y_A - Y_A{}^{P_1Q_1})^2 + (z_A - Z_A{}^{P_1Q_1})^2 \le r_{Q_1}{}^2\} \quad (9)$$

$$\Psi_{P_1} = \Psi_{P_1,Q_1} \cup \Psi_{P_1,Q_2} \cup \ldots \cup \Psi_{P_1,Q_{NE_1}} \quad (10)$$

$$\Omega T_{P_1,D_1} = \{(x_A, y_A, z_A) \in R^3 \mid r_2^2 < (x_A - X_A{}^{P_1D_1})^2 + (y_A - Y_A{}^{P_1D_1})^2 + (z_A - Z_A{}^{P_1D_1})^2 \le r_1^2\} - \Psi_{P_1} \quad (11)$$

$$FT^{'}_{P_1,D_1}(x_A, y_A, z_A) = \begin{Bmatrix} \dfrac{1}{n(\Omega T_{P_1,D_1})} \\ when\,(x_A, y_A, z_A) \in \Omega T_{P_1,D_1}, \\ \\ 0\ otherwise \end{Bmatrix} \quad (12)$$

$$n(S)\ is\ the\ number\ of\ elements\ in\ the\ set\ S$$

$$FT_{P_1,D_1} = f_G * FT^{'}_{P_1,D_1} \text{ where } f_G \text{ is a 3-D Gaussian kernel} \quad (13)$$

The statistical map of stimulation response built by combining several data points from a population of patients using Gaussian smoothed spherical shell kernels after trimming them using no-efficacy (or no-adverse-effect) data is represented by FT^{GSSS}. The value of FT^{GSSS} at any point (x_A, y_A, z_A) due to L patients P_1, P_2, …, P_L contributing N_1, N_2, …, N_L data points respectively is represented as $FT^{GSSS}(x_A, y_A, z_A)$ and computed based on equation 14.

$$FT^{GSSS}(x_A, y_A, z_A) = \frac{1}{\sum_{i=1}^{L} N_i}\left(\sum_{i=1}^{L}\sum_{j=1}^{N_i} FT_{P_i,D_j}(x_A, y_A, z_A)\right) \quad (14)$$

While this method was conceived as an approach to further improve the GSSS kernel based maps, it is not used in the rest of the dissertation as it is extremely sensitive to the data. This is because the mask which includes all regions activated by no-efficacy mask (or no-adverse-effect mask) zeroes out overlapping regions activated by efficacious (or adverse effect) observations. As with any real measurements, measurement errors or noise are possible during the surgery due to a number of factors including assessment errors, hardware errors and personnel errors. While such errors can also happen with efficacious observations, a few erroneous efficacious measurements cannot have a drastic effect on the maps because of the way the maps are built. However, even a single erroneous no-efficacy or no-adverse-effect observation can have a substantial effect on the efficacy or adverse effect map respectively because it forces the overlapping regions of the map to zero. One such case is shown in the example in figure 19. Figure 19(a) shows sagittal, axial and coronal slices of a GSSS-kernel-based efficacy map built using efficacious data points based on the method in section IV.2.2. In figure 19(b) the same sagittal, axial and coronal slices of the no-efficacy mask is shown. In figure 19(c), the same slices of the efficacy map built after trimming the individual GSSS kernels placed at efficacious data points using the no-efficacy mask is shown. In this particular case, the no-efficacy mask almost completely enclosed the efficacy map possibly due to erroneous no-efficacy measurements and therefore the efficacy map was almost completely eliminated. Thus, while the idea of using no-efficacy and no-adverse-effect data to trim maps seems reasonable, it may be useful only when such data is completely reliable. For the rest of the dissertation, GSSS-kernel-based maps built without trimming the kernels as described in section IV.2.2 are built and used.

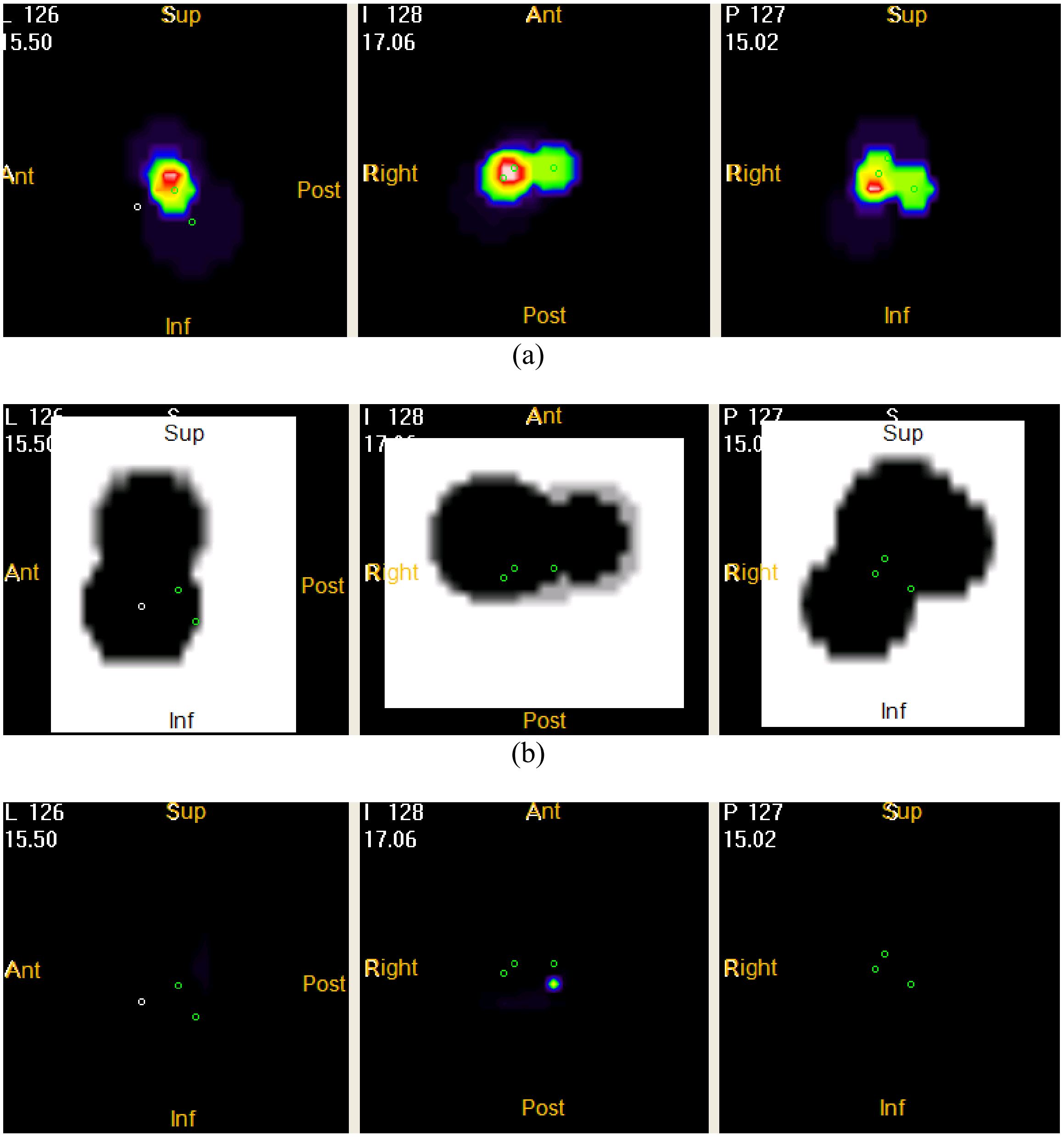

(a)

(b)

(c)

Figure 19. Demonstrating the problem with using no-efficacy data for trimming efficacy maps. Sagittal, axial and coronal slices of (a) GSSS-kernel-based efficacy map built based on the method in section IV.2.2, (b) no-efficacy mask shown in black built using no-efficacy data points, (c) efficacy map built after trimming the individual GSSS kernels placed at efficacious data points using the no-efficacy mask.

To conclude the chapter, a critical drawback of the previous GAUSS model was delineated and a new GSSS model was proposed as an improvement. The centroids of the high likelihood regions (HLR) of the PD and ET efficacy maps built using the new GSSS kernel were found to be substantially closer to the corresponding mean intra-operative implant positions (IOIP) from a population of patients than were the HLR centroids for the maps built using the old GAUSS kernel. Furthermore, the old GAUSS kernel produced multiple isolated HLRs all of which were farther away from the mean IOIP than were the HLR centroids for the GSSS-kernel-based maps. Further validation of the new kernel based maps is presented in chapter VI. A method to use no-efficacy and no-adverse-effect data to trim the efficacy and adverse effect maps respectively was proposed and its effects investigated. The results suggest that such an approach is highly sensitive to the reliability of the no-efficacy and no-adverse-effect data.

CHAPTER V

STUDYING THE EFFECT OF INTRA-OPERATIVE BRAIN SHIFT ON CREATION OF AN ELECTROPHYSIOLOGICAL ATLAS

Abstract

In stereotactic neurosurgery, an underlying assumption is that anatomical structures do not move between the time of the pre-operative image acquisition and the time of the surgery. However, this assumption is not valid. In this chapter, electrophysiological data acquired intra-operatively in a population of patients are used to show that intra-operative brain shift has a substantial effect on the creation of atlases of such data. The findings suggest that brain shift must be taken into account when creating such atlases.

This work was published in the International Journal of Computer Assisted Radiology and Surgery in 2009 [78-80].

V.1 Introduction

An underlying assumption in stereotactic neurosurgery is that anatomical structures do not move between the time of the pre-operative image acquisition and the time of the surgery. However, this assumption is not valid. Recently, by comparing pre- and post-operative images, Wester et al. [39], Winkler et al. [40] and Khan et al. [41] reported that brain tissues can in fact shift during DBS surgery. Intra-operative brain shift happens due to loss of cerebrospinal fluid, air invasion into the skull referred to as pneumocephalus, gravitational force [46] and forces due to insertion of the DBS lead. Although intra-operative neurophysiological techniques such as micro-electrode mapping and macro/semi-macro electrode stimulation may compensate for it, brain shift may require a greater number of test-electrode passes thereby lengthening the procedure, increasing the likelihood of complications, and potentially impacting the outcome. A review of STN-implanted patients in 2001 by the DBS-for-PD study group suggested that the higher the number of microelectrode passes the higher the risk of intracranial bleeding during DBS [47].

Brain shift can affect the accuracy of functional atlases, databases of intra-operative observations, and statistical maps of such data developed by various groups [27, 31, 34, 37, 48, 49]. This is because pre-operative image volumes are typically used to create such atlases whereas due to brain shift the pre- and intra-operative coordinates of anatomic structures may be different. Therefore, ignoring brain shift could lead to inaccuracies in the statistical atlases and maps and reduce the predictive value of the systems that use this information. In this study, using intra-operatively acquired electrophysiological data from a number of patients projected onto an atlas MRI it is shown that brain shift has a substantial effect on the creation of electrophysiological atlases. Therefore, it must be taken into account when building such atlases.

Figure 20(a) shows an axial slice of a pre-operative CT. On the corresponding slice in the post-operative CT acquired immediately after surgery, figure 20(b) shows pneumocephalus as well as posterior shift and shrinking of the ventricles.

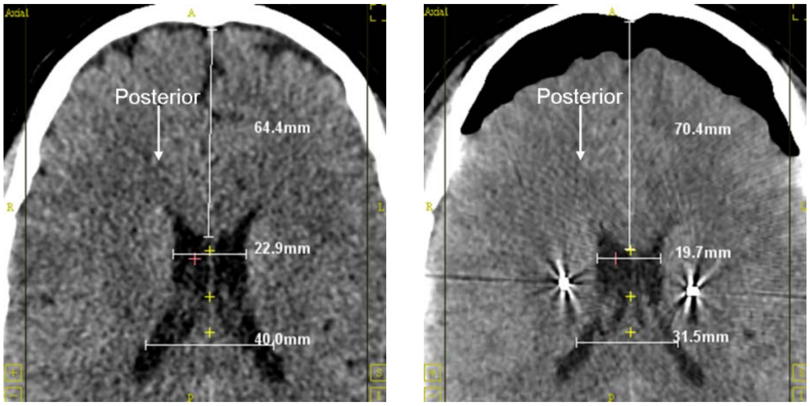

(a) (b)

Figure 20. Corresponding axial slices of (a) pre-operative CT and (b) post-operative CT acquired immediately after surgery. Measurements of the ventricles indicate posterior shift and shrinking or medial contraction of the ventricles post-operatively.

V.2 Data and Method

One pre-operative CT and one post-operative CT acquired on the day of the surgery (referred to as immediate CT) were acquired for each patient at kVp = 120 V, exposure = 350mAs and 512x512 pixels. In-plane resolution and slice thickness were approximately 0.5 mm and 0.75 mm respectively. Pre-operative MRI images were acquired using the

SENSE parallel imaging technique (T1W/3D/TFE) from Philips on a 3T scanner (TR 12.2 ms, TE 2.4 ms, 256x256x170 voxels, with typical voxel resolution of 1x1x1 mm^3).

Intra-operative somatotopy and stimulation responses were recorded for this study. Data were acquired during the surgery using the procedure described in section IV.1. Somatotopy is defined as the correspondence of receptors in regions or parts of the body via respective nerve fibers to specific functional areas of the cerebral cortex. A somatotopic response at a given location in the patient's brain during DBS refers to observing noticeable change in micro-electrode recordings when a stimulus like flexion or extension is applied to a body part like the elbow, shoulder or wrist. A total of 73 somatotopy data points from 24 STN implantations were used. Stimulation response data included the location of each stimulation point, efficacy (therapeutic response) observed as percentage reduction in symptoms and the associated stimulation current, adverse effect (if any) and the associated current. 1512 stimulation data points from 92 PD patients were available. Of these, only those where at least 50% efficacy was observed were chosen as efficacy data points. Using this approach, 754 efficacy data points from 78 PD implantations (STN DBS) were populated and projected onto an MRI atlas.

Rosenbaum *et al.* [81] showed that brain shift in the deep brain is proportional to the amount of air invasion or pneumocephalus. Therefore, after AC-PC alignment, each immediate CT (CT-PI) was carefully inspected for pneumocephalus and classified into one of 3 categories: low, medium and large brain displacement corresponding to average air pocket width at lead level of less than or equal to 3 mm, between 3 mm and 7 mm, and higher than 7 mm respectively. Figure 21 shows sagittal slices (containing the final implant) from immediate CTs of three different patients with low, medium and large average air pocket width. The air pockets were measured from the inner table of the calvarium in the frontal cortex as shown. The process flow for grouping a population of patients into the various shift groups is shown in figure 22. Electrophysiological data (somatotopy and stimulation response) from low-shift patients were mapped onto the atlas by rigid and non-rigid registration between the patient and atlas MRIs to form the low-shift electrophysiological atlas. Similarly, medium- and large-shift electrophysiological atlases were created. This is shown in figure 23 for low- and large-shift groups.

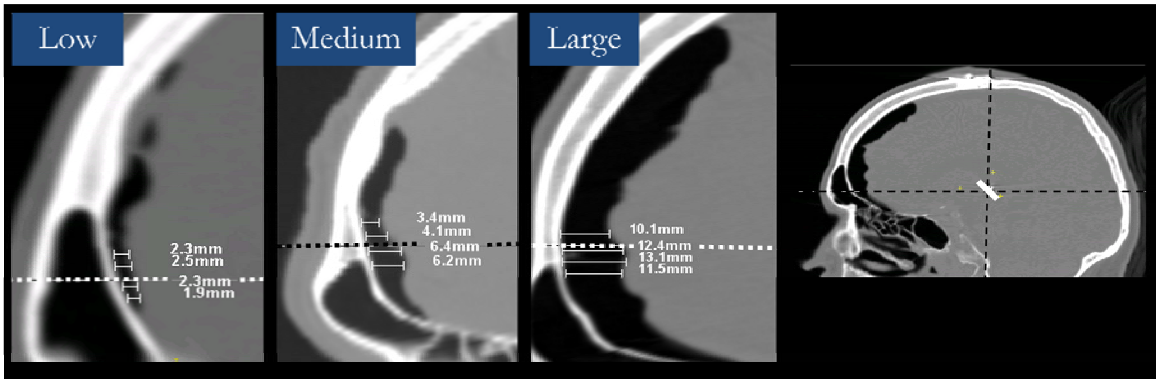

Figure 21. Sagittal slices containing the final implant for low-, medium- and large-shift patients classified based on the width of the air pocket in the immediate CT.

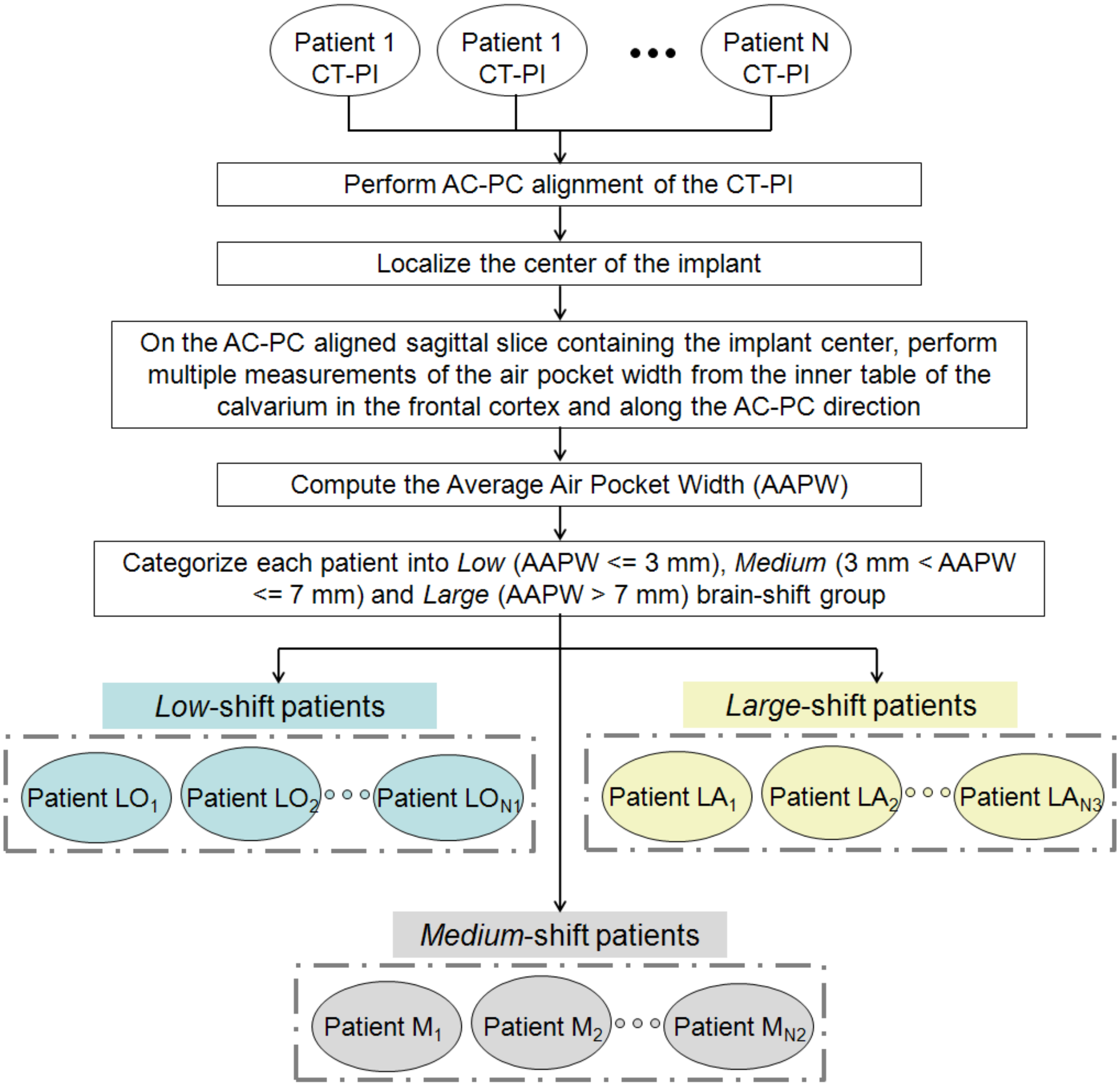

Figure 22. Grouping patients into low-, medium- and large- shift groups based on the average air pocket width at lead level as seen on the immediate CT.

Efficacy maps were built for the low-, medium- and large-shift-atlases based on the method described in section IV.2.2 using the Gaussian smoothed spherical shell kernel. The high likelihood regions (voxels with values at least 70% of the map maximum) of the efficacy maps were compared across the various brain shift groups.

Similarly, the locations of the somatotopy clusters were compared across the various brain shift groups.

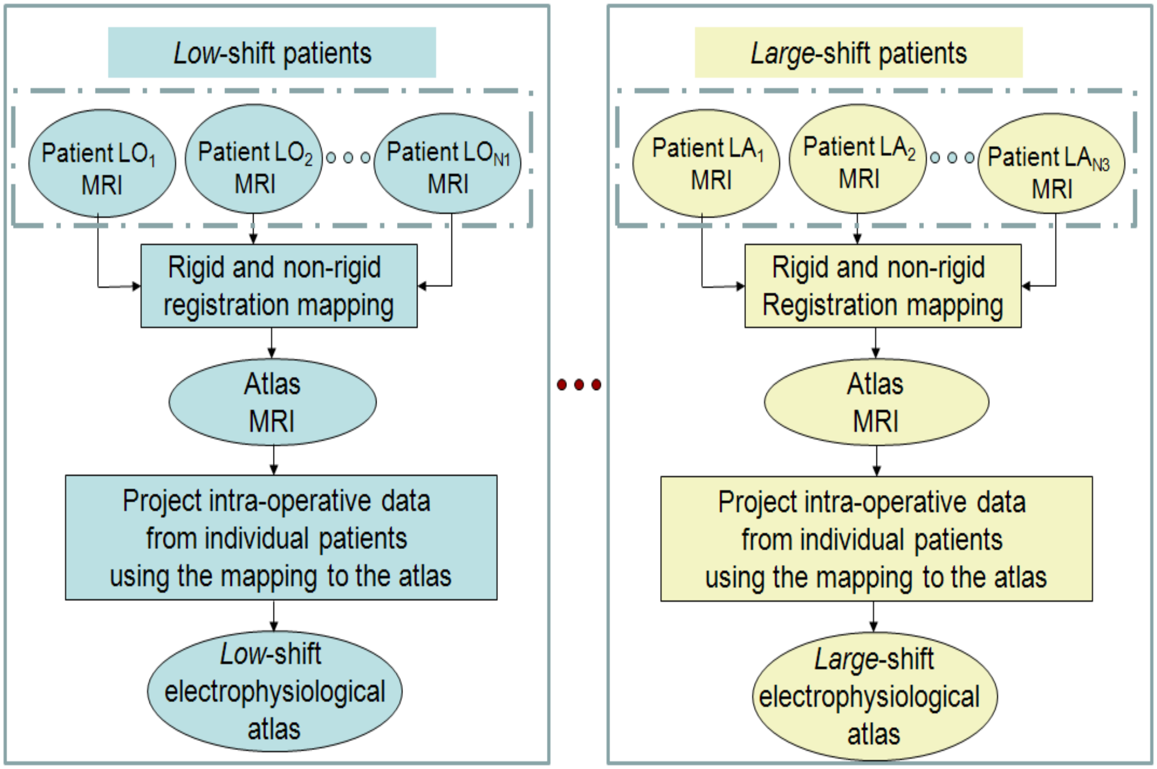

Figure 23. Flowchart for populating electrophysiological atlases of various brain shifts.

V.3 Results

V.3.1 Quantifying the effect of brain shift using somatotopy data

Grouping somatotopy data based on pneumocephalus following the flowchart in figure 22 resulted in 17, 47 and 9 data points in the low-, medium- and large-shift groups respectively. The coordinates (posterior, lateral, inferior) in mm of the centroids were (1.94, 13.92, 3.20), (2.90, 13.57, 4.53) and (3.06, 11.27, 5.36) for the low-, medium- and large-shift clusters respectively and shown in figure 24. The centroid of the medium-shift cluster was located posterior, inferior and medial to that of the low-shift cluster. Furthermore, the centroid of the large-shift cluster was posterior, inferior and medial to that of the medium-shift cluster.

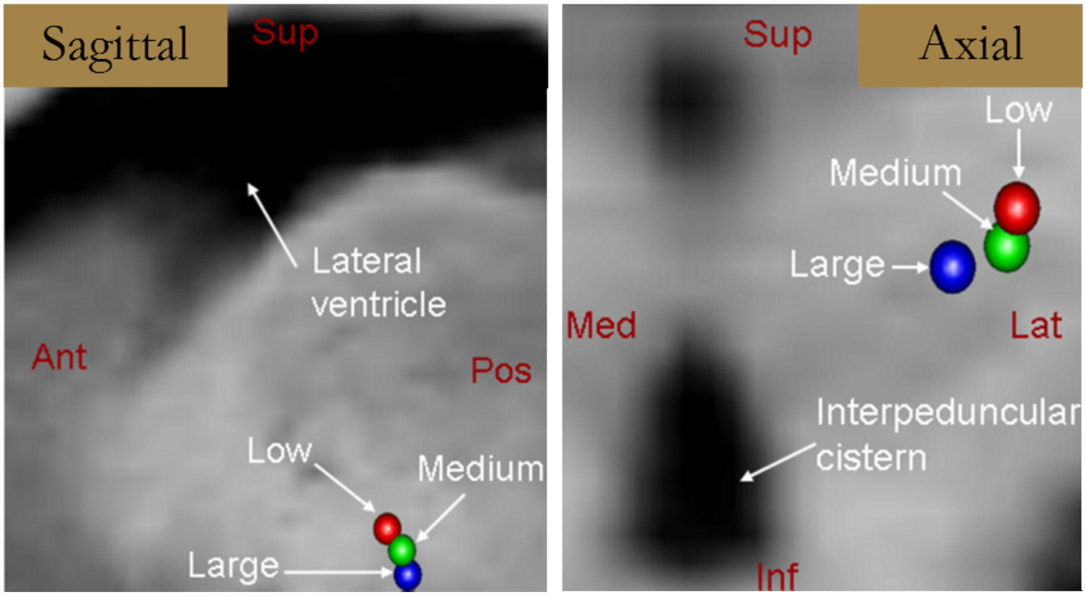

Figure 24. Centroids of the somatotopy clusters from low-, medium and large-shift electrophysiological atlases showing the larger shift clusters being medial, posterior and inferior to the lower shift clusters.

In table 9 Euclidean distances between centroids of various shift groups have been tabulated. The Euclidean distances between the centroids of low- and large-shift clusters, medium- and large-shift clusters, and low- and medium-shift clusters were 3.59 mm, 2.44 mm and 1.68 mm respectively.

Table 9. Euclidean distance between centroids of somatotopy data clusters of various brain shift groups.

Distance between Centroids (mm)			
	Low	Medium	Large
Low	0	1.68	3.59
Medium	1.68	0	2.44
Large	3.59	2.44	0

V.3.2 Quantifying the effect of brain shift using statistical maps of efficacious stimulation response

The stimulation response data consisted of 194 points from 20 implantations, 350 point from 38 implantations and 186 points from 20 implantations in the low-, medium- and large-shift groups respectively. PD efficacy maps created for each shift group overlaid on the atlas MRI are shown in figures 25 and 26 in (a) axial, (b) coronal and (c) sagittal orientations. The images are AC-PC aligned. Posterior, lateral and inferior measurements from fixed landmarks (yellow crosshairs) to the centers of the high likelihood regions for the various maps are also shown.

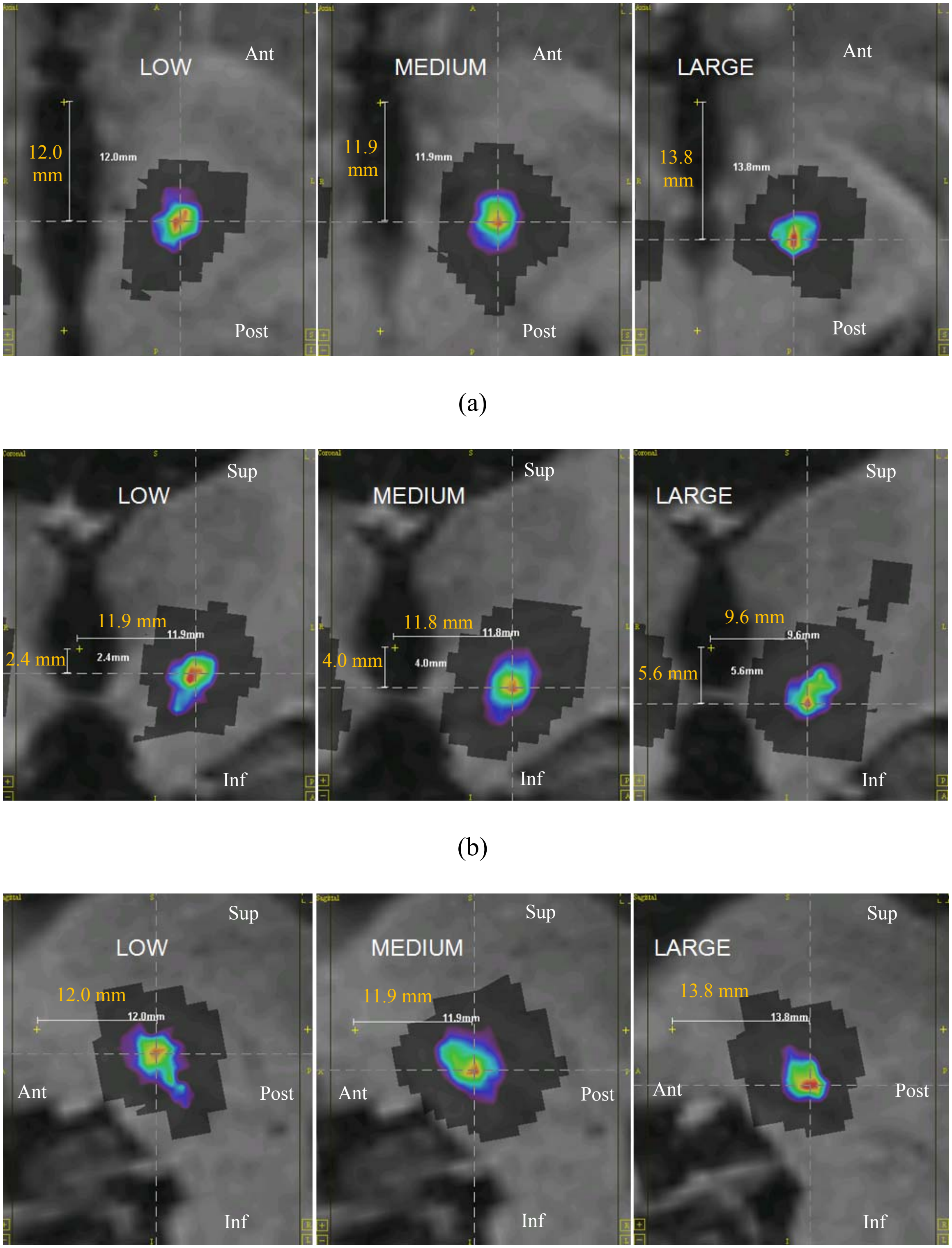

(a)

(b)

(c)

Figure 25. Low-, medium- and large-shift PD efficacy maps for the left brain overlaid on the MRI atlas shown in (a) axial, (b) coronal and (c) sagittal orientations.

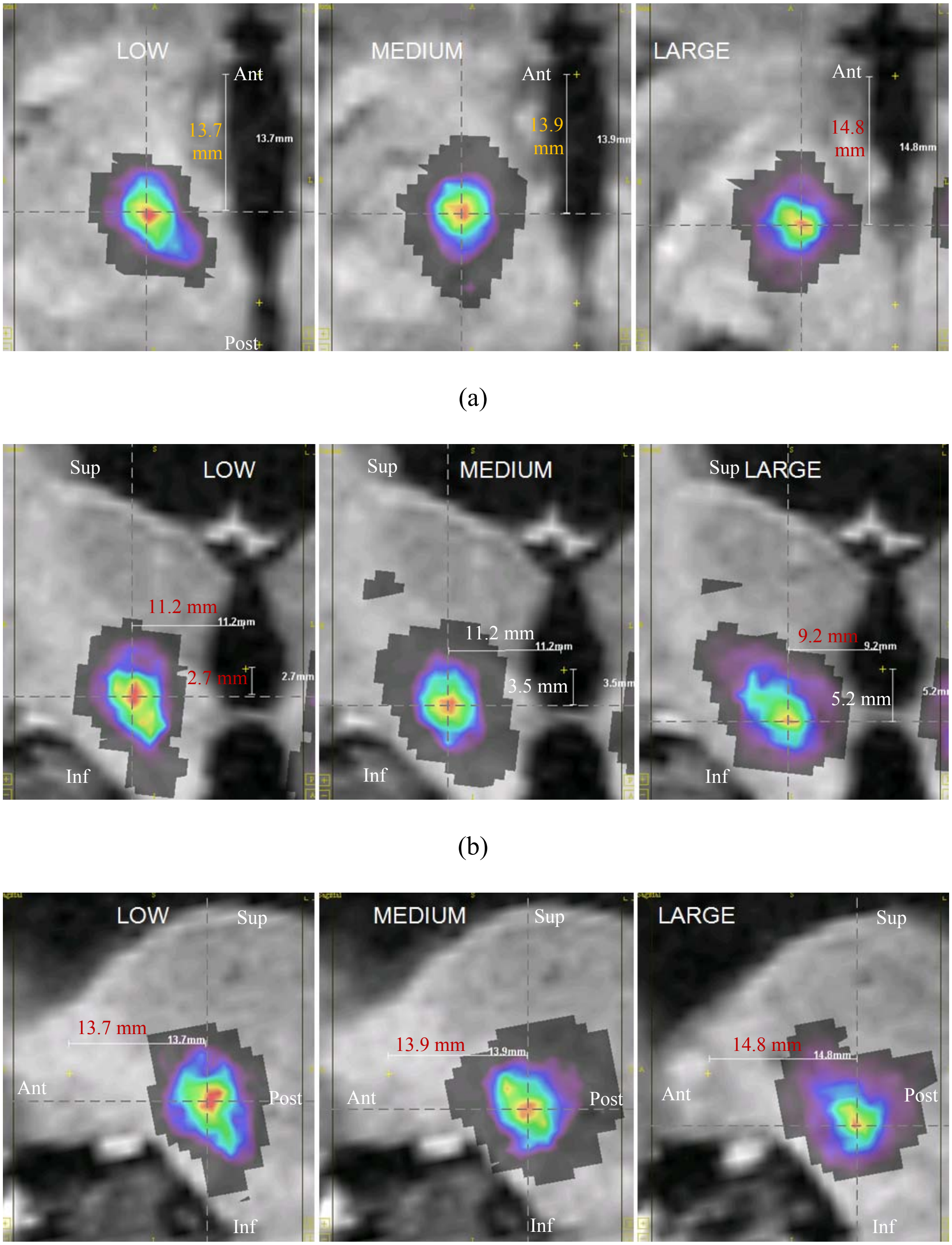

(a)

(b)

(c)

Figure 26. Low-, medium- and large-shift data based PD efficacy maps for right brain overlaid on the MRI atlas shown in (a) axial, (b) coronal and (c) sagittal orientations.

Tables 10 and 11 give the coordinates of the centroids of the high likelihood regions for the low-, medium- and large-shift efficacy maps. The coordinates show that the medium-shift efficacy maps were inferior to the low-shift efficacy maps by 0.77 mm and 1.1 mm for the right and left sides respectively. The large-shift efficacy maps were inferior to the low-shift efficacy maps by 2.47 mm and 2.83 mm for the right and left sides respectively. The low- and medium-shift efficacy maps were found to be quite similar in the anterior and lateral directions. The large-shift efficacy maps were posterior to the low-shift efficacy maps by 1.12 mm and 1.84 mm for the right and left sides respectively and medial to the low-shift efficacy maps by 1.93 mm and 2.20 mm for the right and left sides respectively.

Table 10. AC-PC coordinates (posterior, lateral, inferior) of the centroids of the high likelihood regions for the low-, medium- and large-shift PD efficacy maps (STN) for the right brain.

Right STN	Posterior	Lateral	Inferior
Low	0.21	11.38	2.79
Medium	0.33	11.61	3.56
Large	1.33	9.45	5.26

Table 11. AC-PC coordinates (posterior, lateral, inferior) of the centroids of the high likelihood regions for the low-, medium- and large-shift PD efficacy maps (STN) for the left brain.

Left STN	Posterior	Lateral	Inferior
Low	-1.62	11.90	2.80
Medium	-1.62	11.85	3.90
Large	0.22	9.7	5.63

Table 12 gives the Euclidean distances between the centroids of the high likelihood regions for the low-, medium- and large-shift PD efficacy maps. For the right side, the distances between the centroids of the low- and medium-shift PD efficacy maps, the medium- and large-shift PD efficacy maps, and the low- and large-shift PD efficacy maps were 0.81 mm, 2.92 mm and 3.33 mm respectively. For the left side, the distances between the centroids of the low- and medium-shift PD efficacy maps, the medium- and large-shift PD efficacy maps, and the low- and large-shift PD efficacy maps were 1.1 mm, 3.32 mm and 4.03 mm respectively.

Table 12. Euclidean distance between the centroids of the high likelihood regions for the PD efficacy maps (STN) for various shift groups for (a) right and (b) left sides.

(a) Distance between Centroids of high likelihood regions for the maps (mm)			
Right STN	**Low**	**Medium**	**Large**
Low	0	0.81	3.33
Medium	0.81	0	2.92
Large	3.33	2.92	0

(b) Distance between Centroids of high likelihood regions for the maps (mm)			
Left STN	**Low**	**Medium**	**Large**
Low	0	1.10	4.03
Medium	1.10	0	3.32
Large	4.03	3.32	0

V.4 Discussion and Conclusions

Earlier studies have reported on brain shift by comparing locations of anatomical landmarks like AC and PC between pre- and post-operative images. Such studies could have been affected by changes in patient posture between surgery and post-operative imaging. Their analyses could have also been affected by post-implantation brain shift as well as delay between implantation and post-operative imaging. Furthermore, their comparison was between landmarks that were not directly relevant to the outcome of the surgery. Of greater interest are the electrophysiological data that are used to guide the surgery towards the site of optimal therapeutic benefit and the atlases created using such data from a population of patients. In this study, electrophysiological data including somatotopy observations and stimulation responses recorded intra-operatively in a population of patients were used to investigate the effect of brain shift on the creation of electrophysiological atlases.

Analyses of clusters of somatotopy data as well as of maps of efficacious stimulation response built for the low-, medium- and large-shift groups showed that intra-operative brain shift had a substantial effect on the creation of electrophysiological atlases. The results indicated that considerable brain shift happened before micro-electrode recordings in DBS. Furthermore, the lower brain-shift electrophysiological atlases were anterior, lateral and superior to the larger brain-shift electrophysiological atlases. The low- and medium-shift efficacy maps were quite similar to each other whereas the large-shift efficacy maps were substantially far away from them.

It must be noted that a more reliable approach to group patients based on brain shift would be to use an intra-operative CT to capture snapshots of landmarks in the vicinity of the targets at various stages of the procedure, i.e., immediately after dura opening, before micro-electrode recordings, before micro/macro stimulation and after implantation of the final electrode. Most centers including ours do not have access to intra-operative imaging for DBS. The amount of pneumocephalus seen on the immediate CT provided an accessible solution to categorize patients into various brain shift groups.

In the recent past, a number of functional atlases and databases containing intra-operatively acquired sub-cortical electrophysiological data from a number of patients have been implemented to complement anatomical and histological atlases. Several groups have used such atlases to provide targeting predictions and intra-operative guidance. However, none of these atlases accounts for brain shift. Given that DBS requires precise targeting and implantation with millimetric accuracy, brain shift should be accounted for when building atlases of intra-operatively acquired electrophysiological data. Additionally, due to intra-operative brain shift caution should be used when using intra-operative recordings to validate anatomical atlases.

CHAPTER VI

BUILDING ELECTROPHYSIOLOGICAL ATLASES AFTER ACCOUNTING FOR BRAIN SHIFT

Abstract

The results from the previous chapter show that considerable brain shift happens before micro-electrode recordings in DBS and that brain shift should be accounted for when building atlases of intra-operatively acquired electrophysiological data. This chapter addresses the problem of building an electrophysiological atlas after accounting for brain shift. Statistical maps built using the stimulation response data from such an atlas are validated in this chapter.

This work was published in Lecture Notes for Computer Science in the proceedings of Medical Image Computing and Computer Assisted Intervention (LNCS, MICCAI), 2009 [82].

VI.1 Introduction

The results from the previous chapter indicate that considerable brain shift happens before micro-electrode recordings in DBS. This affects the accuracy of electrophysiological atlases and databases of intra-operative observations developed by various groups because to create such atlases pre-operative image volumes are used, whereas, due to brain shift the pre- and intra-operative coordinates of anatomic structures are different. Therefore, brain shift should be accounted for in order to build accurate electrophysiological atlases. If intra-operative imaging were available then brain shift could be measured during surgery and the coordinates of all intra-operative data could be corrected using this information. In the absence of intra-operative imaging (which is typically the case for DBS surgeries) other approaches are needed. While model-driven brain shift compensation techniques [50] have been used in open craniotomies, these are difficult to implement in burr hole surgeries such as DBS due to very limited brain surface deformation information. In this chapter, the problem of building an electrophysiological atlas after accounting for brain shift is addressed. Statistical maps built using stimulation response data populated on such an atlas are validated.

VI.2 Data and Method

Intra-operative data was acquired using the procedure described in section IV.1. Data used in this study includes 544 efficacy points from 58 Parkinson's disease (PD) implantations, 280 efficacy points from 20 Essential tremor (ET) implantations and 266 paresthesia adverse effect points from 37 implantations.

VI.2.1 Eliminating large brain shift patients from the atlas-building process

Electrophysiological atlases can be built after accounting for brain shift by eliminating large-shift patients from the process of atlas-building. Patient selection depending on the amount of brain shift can be based on the amount of pneumocephalus seen on the immediate CT as described in the previous chapter. Specifically, by using data from only low-shift patients an atlas minimally affected by brain shift can be created. This means that data from a number of patients belonging to the medium- and large-shift groups cannot be used. Results on the effect of brain shift on atlas creation discussed in the previous chapter show little difference between the low- and medium-shift efficacy maps whereas they show substantial difference between the low and large-shift efficacy maps. Specifically, the distance between the high likelihood regions for the low- and medium-shift efficacy maps was approximately 1 mm, which was one-third that between the medium- and large-shift efficacy maps and one-fourth that between low- and large-shift efficacy maps. Therefore, to reduce loss of data without compromising on brain shift, patients from the low- and medium-shift groups can be combined. Thus, an electrophysiological atlas can be built after accounting for brain shift by projecting data from only low- and medium-shift patients onto the atlas. In the rest of this document, such an atlas is referred to as a low-shift-atlas and statistical maps built using such an atlas are referred to as low-shift statistical maps. The flowchart for building a low-shift electrophysiological atlas and validating the statistical maps built using stimulation response data from such an atlas is shown in figure 27.

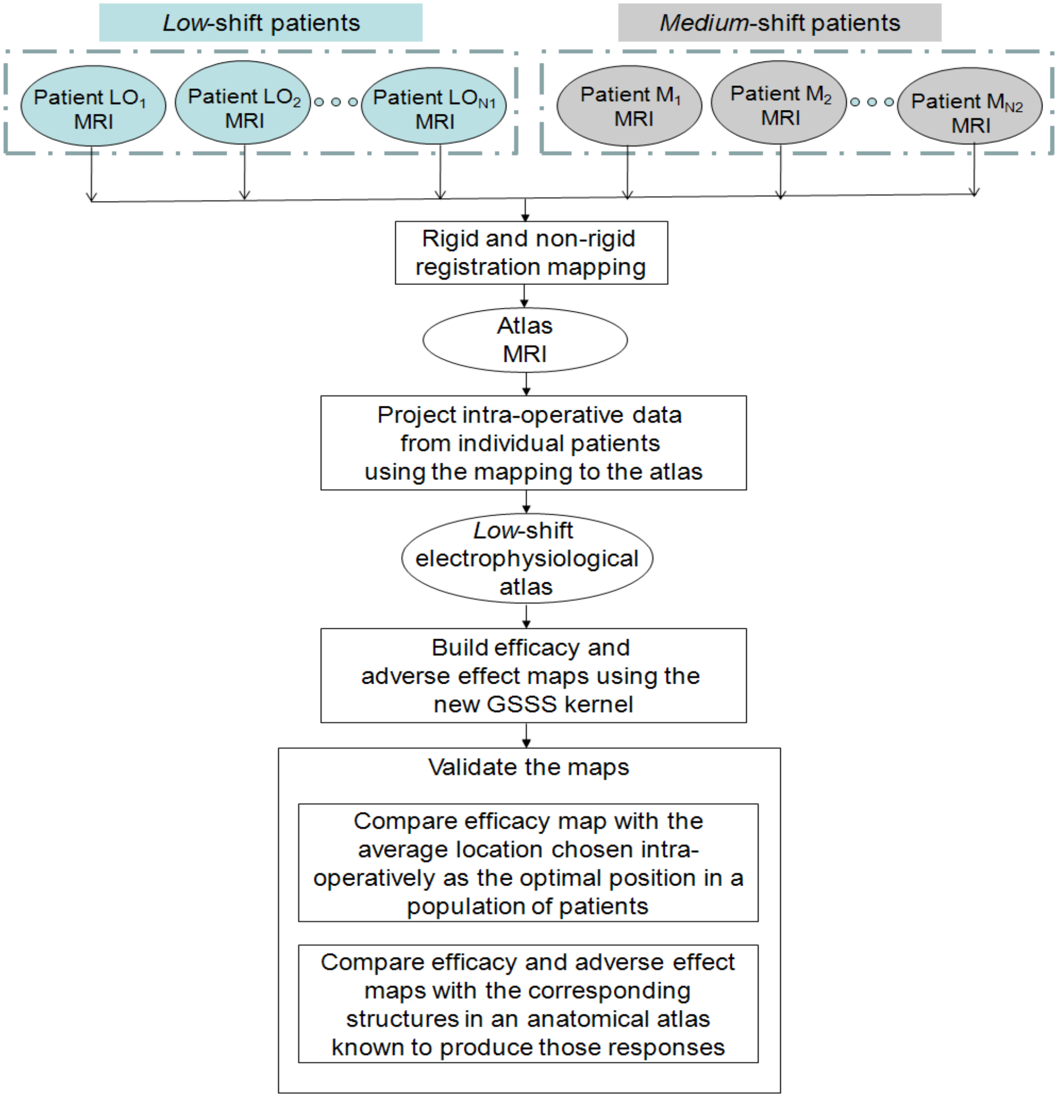

Figure 27. Flowchart for building a low-shift electrophysiological atlas and validating the statistical maps built using stimulation response data from such an atlas.

VI.2.2 Validating the maps built after eliminating large-shift patients

Statistical maps of efficacy and adverse effects built using the low-shift-atlas based on the flowchart in figure 27 were validated in two ways. First, the final implant positions chosen intra-operatively from a population of low- and medium-shift patients were projected onto the atlas and the centroid of that cluster was computed. This was referred to as the mean intra-operative implant position (mean IOIP) and taken as the ground truth against which low-shift efficacy maps were compared. Second, the high likelihood regions for the efficacy and paresthesia maps were overlaid on the Schaltenbrand-Wahren (S-W) atlas and compared against anatomical structures known to produce the corresponding stimulation response as shown in figure 28.

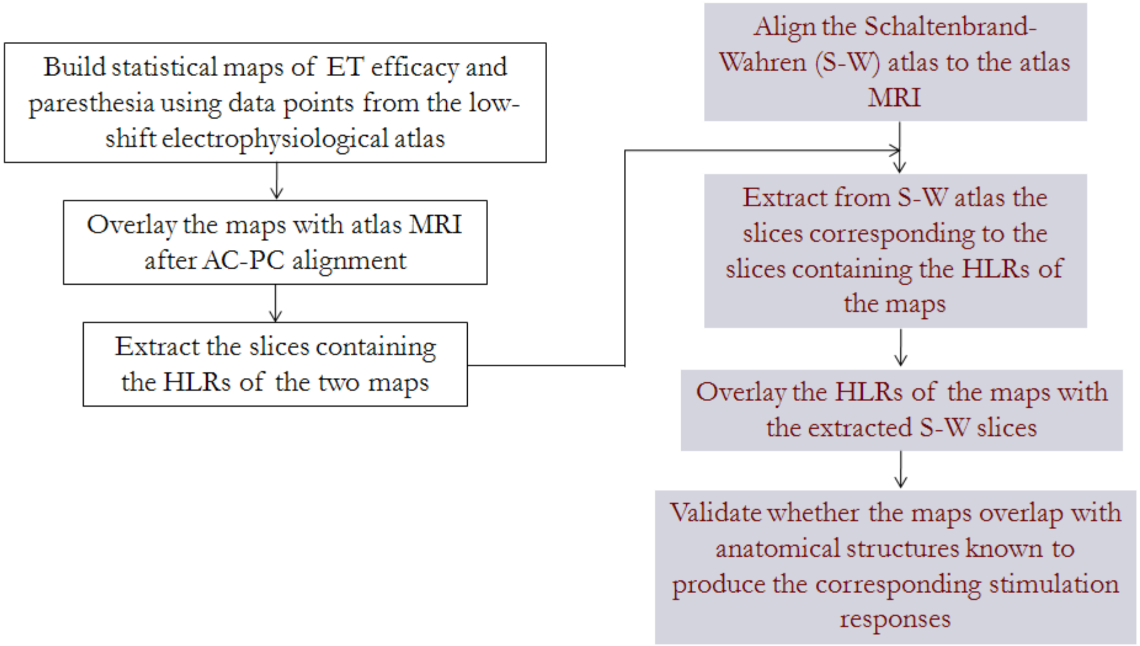

Figure 28. Flowchart for validating statistical maps against anatomical atlases.

This was done by first aligning the maps with respect to the AC and PC of the atlas MRI. Then the S-W atlas was then aligned to the atlas MRI by using the AC and PC landmarks and piecewise-linear scaling to account for the differences in the overall brain size and orientation. The slices of the aligned S-W atlas corresponding to the high likelihood regions for the maps were then extracted. The slices from the maps were overlaid on these anatomical slices and compared against the locations of the structures known to produce the corresponding stimulation response.

VI.3 Results

VI.3.1 Validating low-shift efficacy maps by comparing them against the mean intra-operative implant position from a population of patients

The low-shift PD and ET efficacy maps were overlaid on the MRI atlas and visualized along with the corresponding mean IOIP (ground truth). The centroids of the high likelihood regions for the PD and ET efficacy maps for both sides were found to be in close proximity to the ground truth as shown in figures 29 and 30. Table 13(a) shows the AC-PC coordinates (in mm) of the mean IOIP positions for PD and ET patients for the left and right sides. Table 13(b) shows the AC-PC coordinates of the centroids of the high likelihood regions (HLRs) for the corresponding efficacy maps. The Euclidean distances (mm) of the HLR centroids from the corresponding mean IOIPs are given in table 13(c). Table 13 shows that the HLR centroids for the efficacy maps are in close proximity to the corresponding mean IOIP locations. The left and right PD efficacy maps are 1.58 mm and 1.31 mm away respectively from the corresponding mean IOIPs. The left and right ET efficacy maps are 0.81 mm and 0.77 mm away respectively from the corresponding mean IOIPs.

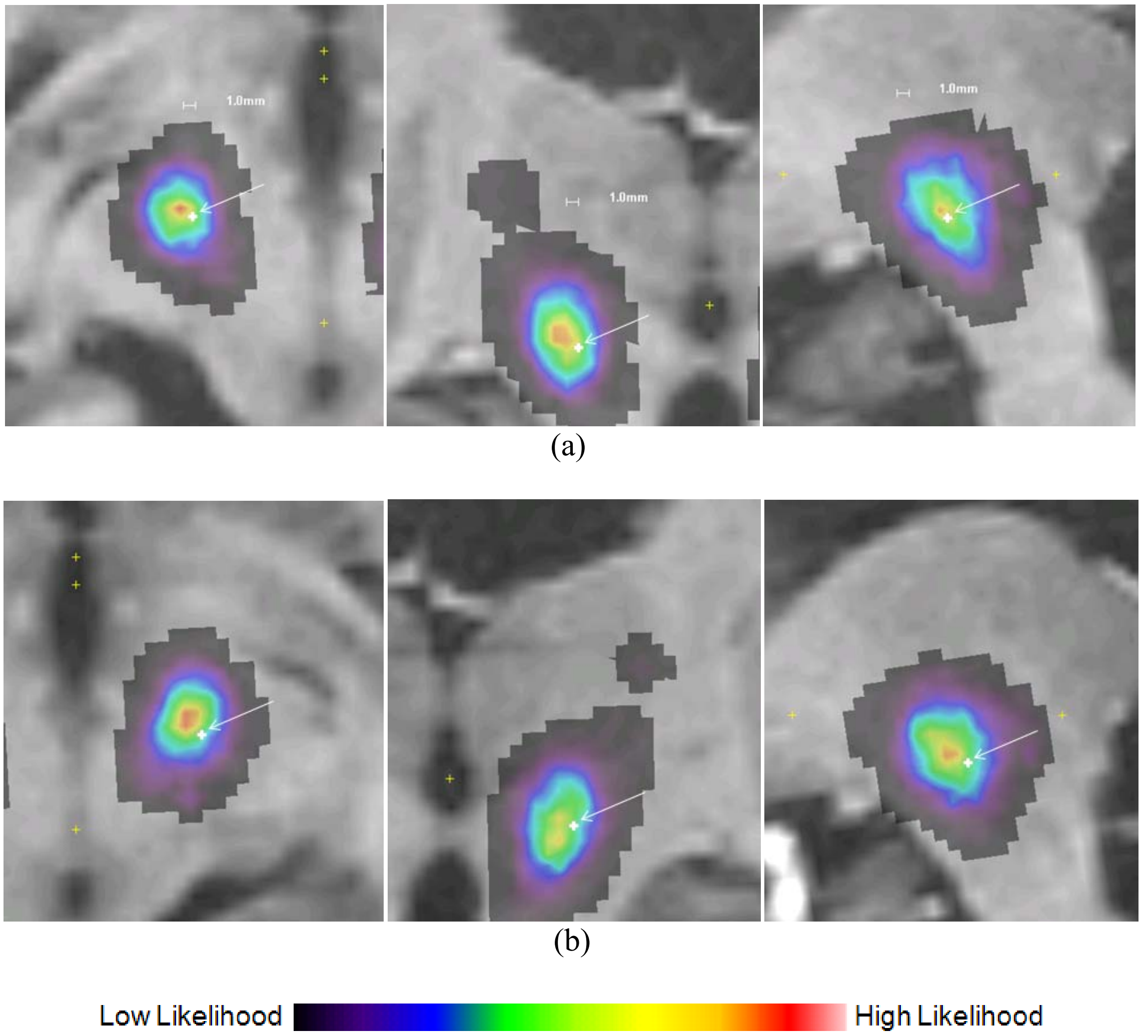

(a)

(b)

(c)

Figure 29. Axial, coronal and sagittal slices of PD efficacy maps for (a) right side (b) left side. (c) Color scale. The mean final implant position from a population of PD patients is shown as a white crosshair.

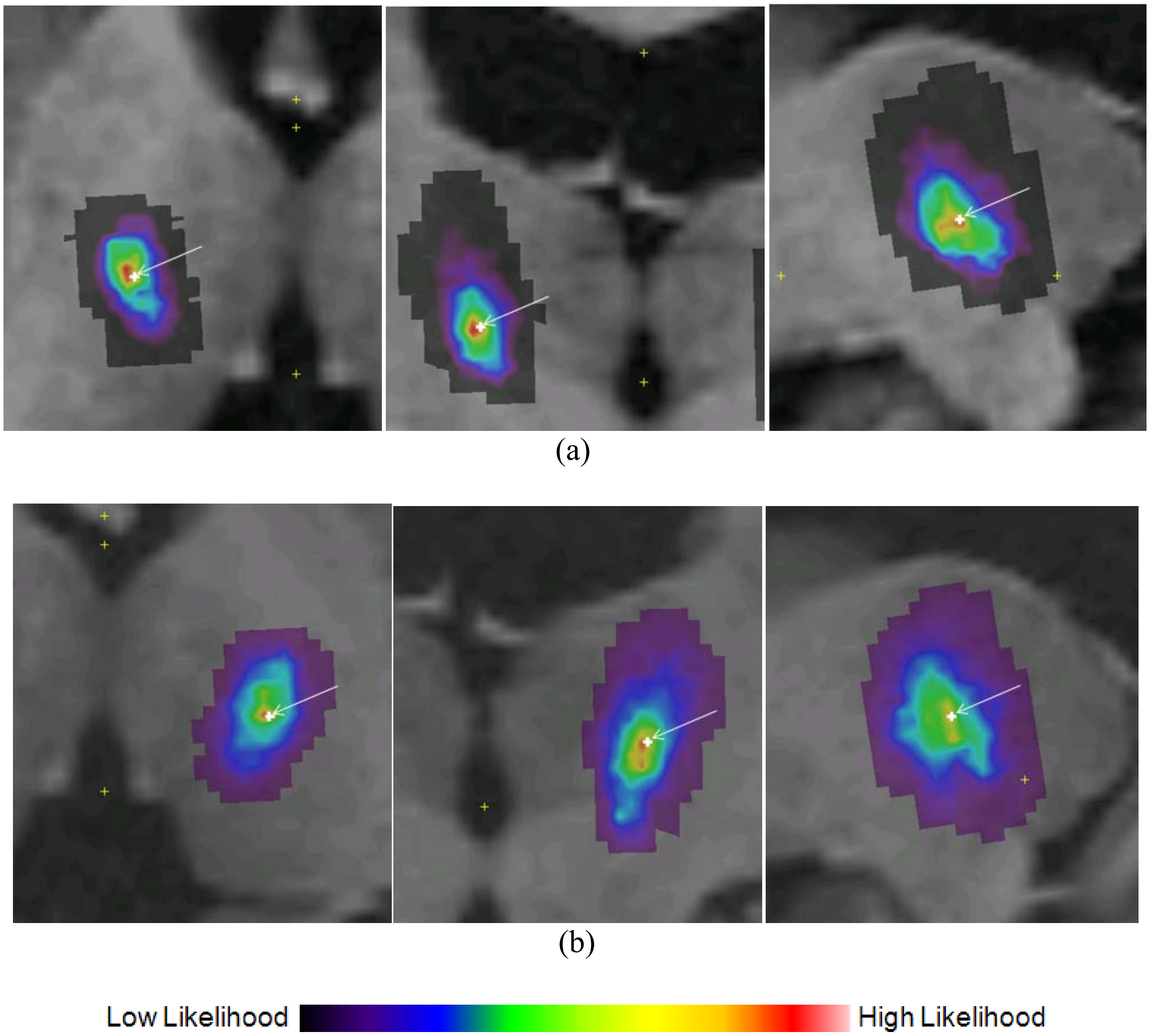

(a)

(b)

(c)

Figure 30. Axial, coronal and sagittal of ET efficacy maps for (a) right side (b) left side. (c) Color scale. The mean final implant position from a population of ET patients is shown as a white crosshair.

Table 13. (a) AC-PC coordinates (lateral, anterior, inferior) in mm of the mean IOIP positions for PD (STN DBS) and ET (Vim DBS) for the left and right sides, (b) AC-PC coordinates of the HLR centroids for the corresponding efficacy maps. (c) The Euclidean distances (mm) of the centroids from the corresponding mean IOIPs.

mean IOIP			
	Lateral (mm)	**Anterior (mm)**	**Inferior (mm)**
Left STN	10.28	-3.35	3.86
Right STN	10.92	-2.41	3.53
Left Vim	13.51	-5.15	-5.38
Right Vim	13.44	-3.3	-4.67

Centroid of high likelihood Efficacy map			
	Lateral (mm)	**Anterior (mm)**	**Inferior (mm)**
Left STN	9.37	-2.07	3.67
Right STN	11.98	-1.83	3.03
Left Vim	13.18	-5.21	-4.64
Right Vim	13.97	-2.85	-4.32

Distance (mm) between high likelihood Efficacy map and mean IOIP	
Left STN	**1.58**
Right STN	**1.31**
Left Vim	**0.81**
Right Vim	**0.77**

VI.3.2 Validating low-shift maps by comparing them against the Schaltenbrand-Wahren anatomical atlas

Figure 31 shows the axial slice containing the high likelihood region of the low-shift ET efficacy map overlaid on top of the corresponding slice of the S-W atlas. The high likelihood region of the efficacy map was in the anatomical Vim (split into Vim.i and Vim.e for internal and external respectively) as shown in the yellow contour. This is consistent with the literature reporting Vim as the widely accepted DBS target for successful essential tremor relief. A European multi-center six year follow-up study of thalamic stimulation recommended Vim stimulation for persistently effective treatment of essential tremor [83]. Lozano [84] also reported that Vim DBS has unequivocal functional benefit in patients with essential tremor. This confirms that the high likelihood region of the low-shift ET efficacy map correlates strongly with the anatomical structure known to produce therapeutic benefit for ET.

Figure 32 shows the axial slice containing the high likelihood region of the paresthesia adverse effect map overlaid on the S-W atlas. The high likelihood region of the paresthesia map was found to be posterior to the efficacy map and in the ventro-caudalis nucleus or the Vc (split into Vc.i and Vc.e for internal and external respectively). This is consistent with information well-documented in literature. Electrophysiology data in the Schaltenbrand atlas [12] show sensory effects like paresthesia in the Vc. The main sources of sensory information are the medial lemniscus and spinal lemniscus which feed into the Vc [85]. Wallace et al. [86] refer to the Vc as a paresthesia-producing stimulation target. Fukushima et al. [87] reported shortest latency in evoked potentials recorded from the Vc due to somatosensory stimulation. This confirms that the high likelihood region of the low-shift paresthesia map correlates strongly with the anatomical structure known to produce paresthesia stimulation response.

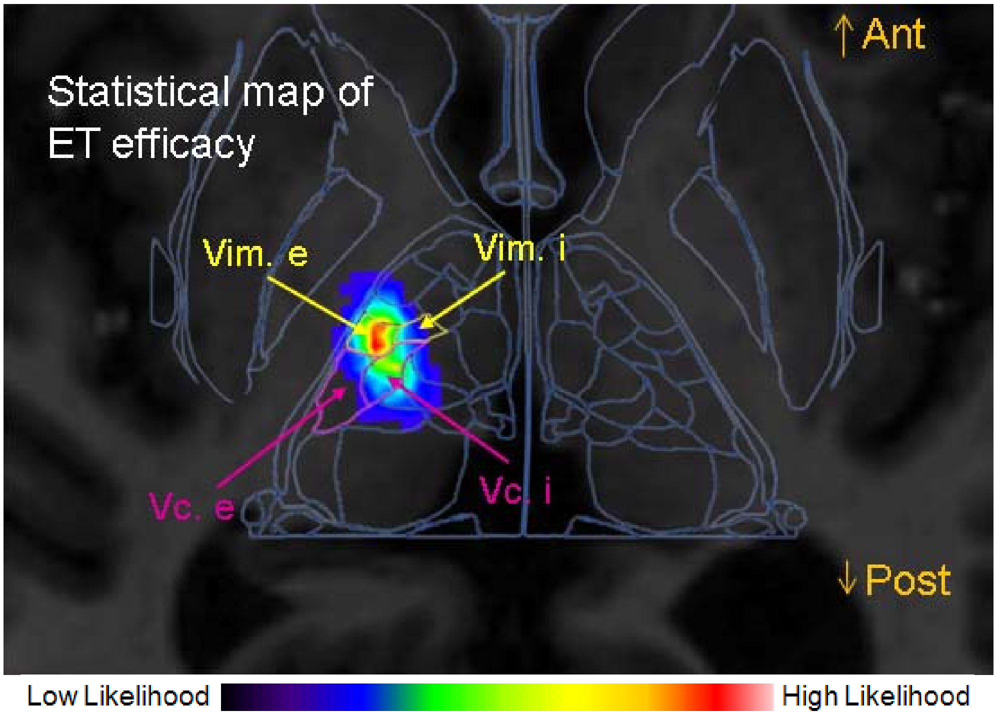

Figure 31. Axial slice containing the high likelihood region of the Vim efficacy map overlaid on the corresponding slice in the Schaltenbrand Wahren (S-W) atlas.

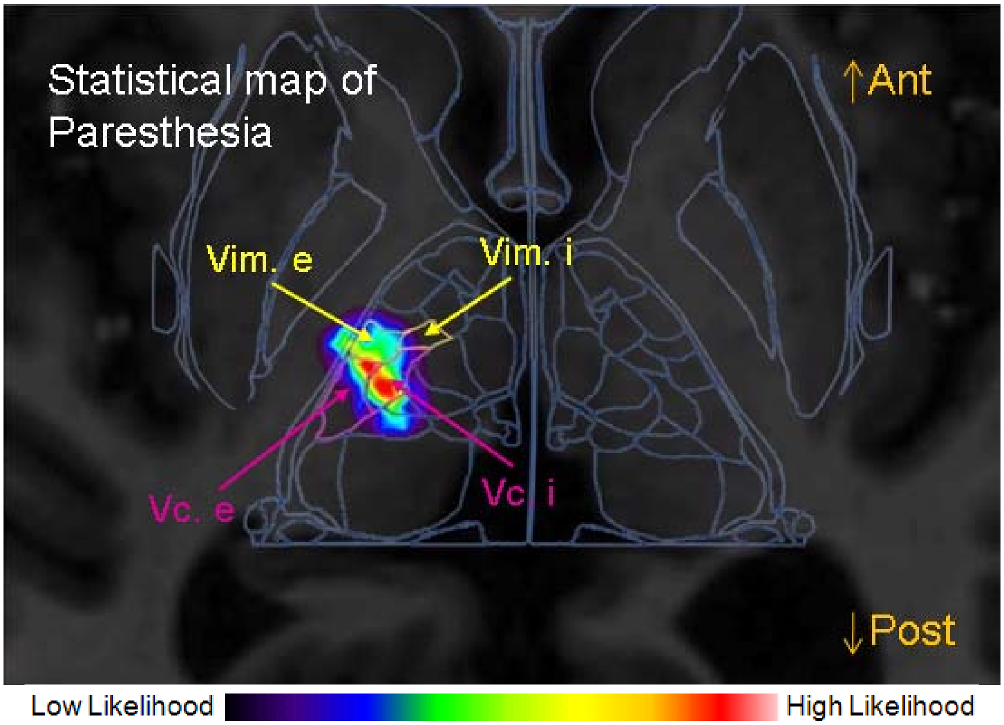

Figure 32. Axial slice containing the high likelihood region of the paresthesia map overlaid on the corresponding slice in the Schaltenbrand Wahren (S-W) atlas.

VI.4 Discussion and Conclusions

Following results from chapter V showing that substantial brain shift happens before micro-electrode recordings during DBS surgery, an approach to build electrophysiological atlases after accounting for brain shift was proposed in this chapter. Using the post-operative immediate CT to categorize patients into various brain shift groups, patients with large brain shift were eliminated from the atlas building process to populate a low-shift-atlas. Efficacy and paresthesia adverse effect maps were built using this atlas and validated. The PD and ET efficacy maps were found to be in close proximity to the corresponding mean intra-operative implantation position in a population of patients. The best anatomical location for successful PD relief is debatable but there is clear consensus that the Vim is the best anatomical target for ET relief. The high likelihood region of the efficacy map built using successful ET relief data was found to be localized inside the Vim visible on the Schaltenbrand atlas. Similarly, it is well-documented in the neuro-electrophysiology community that stimulation in the Vc produces paresthesia. The high likelihood region of the paresthesia map was found to be localized inside the Vc visible on the Schaltenbrand atlas.

A limitation of this approach where the large shift patients are eliminated is that data from a number of patients cannot be used. Ideally, it is valuable to be able to use as much data as possible when building statistical atlases. Therefore, a brain shift correction scheme that can overcome this limitation would be valuable. A preliminary approach for shift-correction is discussed here which will be validated in the future.

Shift-correction using the stabilized implant position

An approach for shift-correction could be developed by understanding the various stages of brain shift. A likely scenario is presented in figure 33. Figure 33(a) shows the pre-operative stage where target selection is performed based on the patient’s images. Figure 33(b) shows the first intra-operative stage when the dura is opened resulting in air invasion or pneumocephalus in the frontal lobe. At this stage the first intra-operative brain shift can be expected to happen. Figure 33(c) shows cannulae inserted into the brain for holding the test electrodes. These cannulae can be expected to act like a fork and hold the brain in place. Figure 33(d) shows the final implant inserted into the brain after electrophysiological mapping while the cannulae are still in the brain. The brain continues to be held in place but pneumocephalus continues to grow. Figure 33(e) shows the final implant in place but the cannulae removed. Since the final implant is a flexible wire the brain is now free to move under the effects of the pneumocephalus. Figure 33(f) shows the brain when the post-operative stable scan is taken a couple of weeks after surgery. By this time the pneumocephalus is completely resolved and the brain is expected to have returned to its pre-operative state after complete brain shift recovery.

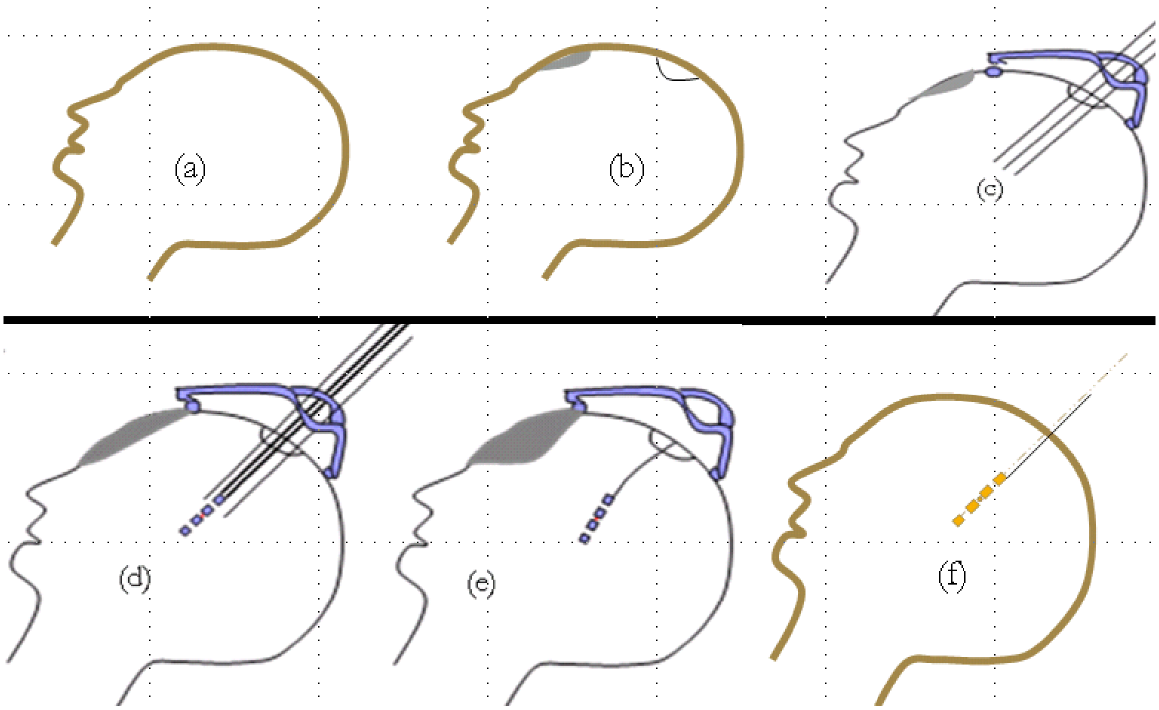

Figure 33. Various stages of brain shift in DBS. (a) Pre-Operative imaging, (b) Intra-operative: Dura opening causing air invasion and brain shift, (c) Intra-operative: platform mounted, cannulae inserted and ready for electrophysiological mapping, (d) Intra-operative: final electrode implanted with cannulae remaining in, (e) Intra-operative: cannulae removed leaving the flexible final implant in allowing the brain to move, (f) Post-operative stable imaging: stable lead position in place after shift recovery.

Assuming that the brain indeed returns to its pre-operative state following complete brain shift recovery by the time of post-operative CT acquisition a few weeks after surgery (stable CT), the position of the implant in the stable CT can be used for shift-correction. Based on this, the following model is proposed. Figure 34(a) shows a detailed model of various brain shift components. During the procedure, the Optimal Target (OT) where the implant should be placed gets displaced due to Brain Shift Before Implantation (BSBI). Ideally, by electrophysiological mapping the displaced OT is identified and the electrode is implanted at that location. This implanted location is the Intra-Operative Implant Position (IOIP).

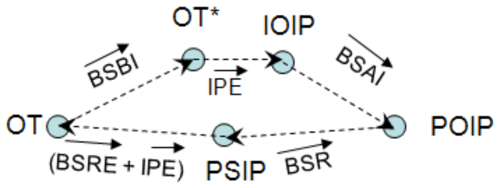

(a) Various brain shift components and stages

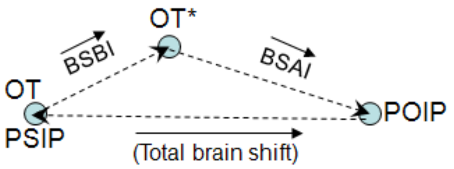

(b) Approximate model assuming IPE and BSRE are negligible

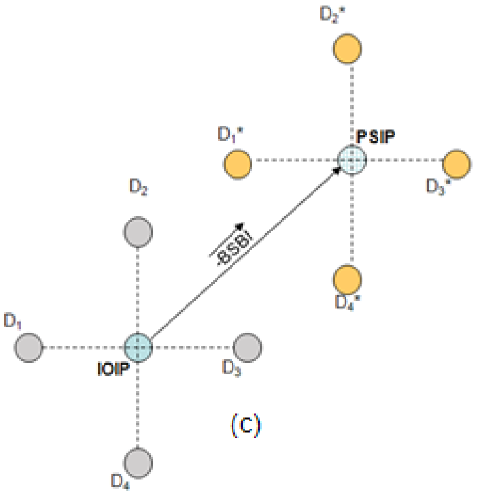

Figure 34. (a) Detailed model of various brain shift components, (b) approximate model assuming that the brain recovers to exact pre-operative state by the time of the stable CT and that IPE is zero, (c) demonstrating how data points D_1, D_2, D_3 and D_4 are corrected for brain shift to arrive at D_1*, D_2*, D_3*, D_4* using the model in (b). OT is the optimal target, BSBI is brain shift before implantation and is referred to as the intra-operative brain shift, BSAI is the brain shift after implantation, BSR is the brain shift recovery vector and BSRE is the brain shift recovery error.

Implant placement error (IPE) due to the finite accuracy of the stereotactic system and/or manual errors results in the implant being placed at a slightly different location (IOIP*). Brain Shift After Implantation (BSAI) causes the implant to move further to the Post-operative Immediate Implant Position (PIIP) which can be seen in the post-operative CT acquired immediately after surgery (immediate CT). Finally, the lead stabilizes at the Post-operative Stable Implant Position (PSIP) by the time the stable CT is acquired. The difference between PSIP and OT is because of IPE and/or Brain Shift Recovery Error (BSRE) due to the brain not recovering exactly to its pre-operative state. If we assume that BSRE and IPE are negligible, the model reduces to the simpler formulation shown in figure 34(b) where PSIP returns to OT.

Using this model, brain shift could be accounted for when populating atlases since the relative positions of all intra-operative data points are known with respect to the IOIP. By changing the reference from IOIP to PISP and maintaining the same relative positions for the data points, their coordinates can be corrected for brain shift. This is illustrated in figure 34(c) for four points. By populating electrophysiological atlases using these transformed coordinates, shift-corrected atlases could be populated using data from all patients irrespective of the amount of brain shift they suffered. While this preliminary model seems promising, the validity of the underlying assumptions needs to be verified and the atlases built using this method validated. Therefore, only maps built by eliminating large shift patients have been validated in section VI.3 are used in the rest of the work.

CHAPTER VII

PRELIMINARY STUDY ON THE CLINICAL USEFULNESS OF AN ELECTROPHYSIOLOGICAL ATLAS FOR POST-OPERATIVE PROGRAMMING ASSISTANCE FOR DBS

Abstract

In this chapter, a preliminary study on the clinical usefulness of statistical maps of stimulation response for post-operative DBS programming assistance is presented. The Gaussian smoothed spherical shell kernel proposed in chapter IV was used to build the maps. The maps were built using data from the low-shift electrophysiological atlas built and validated in chapter VI.

VII.1 Introduction

Post-operative neurological management of DBS patients is a complex and dynamic process. It involves selecting an optimal contact from the 4 contacts (numbered 0, 1, 2 and 3, with 0 being the most ventral contact and 3 being the most dorsal contact) available on an implant and optimizing the stimulator programming parameters to alleviate symptoms. Symptom alleviation (efficacy) is desired with decrease in medication while avoiding adverse effects. This is referred to as therapeutic benefit. The difference in the stimulation amplitude producing efficacy and the larger stimulation amplitude inducing adverse effect is referred to as the therapeutic window. Additionally, the neurologists also have to try to minimize energy consumption of the stimulator to prolong battery life. In clinical practice, finding the optimal contact and programming parameters can be a challenging and time-consuming process. Furthermore, neurologists programming the DBS implant must have expert knowledge of the electrophysiology of the area neighboring the implant.

Generally, a neurologist conducts the first programming session approximately two weeks after implantation. This allows the patient to recover from surgery and provides enough time for the transient lesion effects to resolve. Detailed principles and methods used to select the optimal programming parameters have been presented by different authors [88, 89]. Briefly, the first step in post-operative programming is the examination of efficacy and adverse effects induced by stimulation. The contacts are individually evaluated in an effort to determine the one that produces the best therapeutic benefit. Frequency and pulse width are typically kept at constant settings of 130-180 Hz and 60-120 μs respectively. These are similar to the settings used intra-operatively. Amplitude is steadily increased to the tolerance level of the patient or until adverse effects occur. As the stimulation amplitude is increased, repeated motor evaluation is performed to assess the efficacy of stimulation. Typically, ten to fifteen minutes are to be allowed to pass between trials of separate contacts to allow the effects from previous stimulations to disappear. The initial programming session as described above can take several hours and requires continuous feedback from the patient to ascertain the degree of benefit and to identify any adverse effects. This can be very taxing, especially when the patient is kept off medication for long periods of time. Furthermore, finding the optimal settings may take several trials over many months which can be frustrating.

Using efficacy maps, D'Haese et al. [73] have shown that it is feasible to provide assistance for the selection of optimal contact for DBS programming. However, in that work adverse effect maps were not used. Furthermore, the value of the efficacy map at the location of each contact was the only feature used to identify the optimal contact. There are certain limitations to this approach as illustrated in figure 35. Figure 35(a) shows an efficacy map overlaid on an implant with 4 contacts labeled 0, 1, 2 and 3. If only the value of the efficacy map at each contact is chosen as a discriminator to choose the optimal contact then contact 3 would be the optimal contact. In the case of figure 35(b), based solely on the value of the efficacy map at each contact, contact 3 would be the optimal contact. But, based on visual examination contact 2 may be preferred over contact 3 due to its closer proximity to the high likelihood region of the efficacy map. Figure 35(c) shows the case where based on proximity to the high likelihood region of the efficacy either contact 1 or contact 2 can be chosen. Figure 35(d) shows the same case as in figure 35(c) but with the additional information of an adverse effect map (labeled

AE). The overlap of the high likelihood region of the adverse effect map with contact 2 suggests that contact 1 should be preferred over contact 2. Thus, using more than one type of statistical map and multiple features from such maps may be useful in predicting the optimal contact. In this chapter, a preliminary investigation on the usefulness of such a system for DBS programming assistance is described. Such a system may facilitate the programming process and impact the outcome of the surgery.

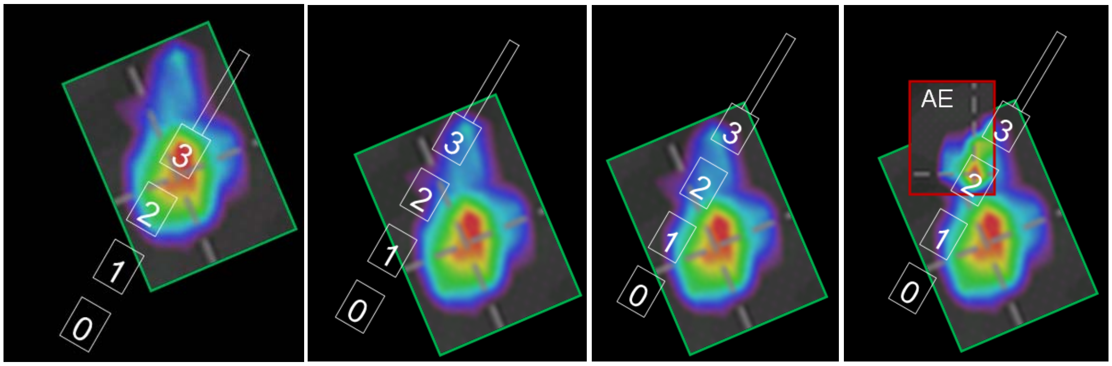

(a) (b) (c) (d)

Figure 35. Illustrating optimal contact prediction based on the interaction between statistical maps and the implant. (a) Contact 3 is the optimal contact based solely on the value of the efficacy map at the contact, (b) Contact 2 is the optimal contact based on its proximity to the high likelihood region of the efficacy map, (c) Either contact 1 or contact 2 may be the optimal contact based on their proximity to the high likelihood region of the efficacy map, (d) Same as case (c), but, the additional information provided by the high likelihood region of the adverse effect (AE) map overlapping with contact 2 helps choose contact 1 as the optimal contact.

VII.2 Data and Method

The study was carried out on 23 STN DBS implantations for Parkinson's disease patients. Patient selection was based on two criteria, namely, availability of the post-operative stable CT (CT-PS) as well as good therapeutic response to the programming session. Efficacy (544 points from 58 implantations), paresthesia (202 points from 41 implantations) and dysarthria (98 points from 20 implantations) data points were projected from the low-shift electrophysiological atlas onto each patient MRI using non-rigid registration. From the patient MRI they were projected onto the patient's post-operative stable CT (CT-PS) using rigid registration. For every case, the implant in CT-PS was extracted and each of the 4 contacts was localized. Efficacy, paresthesia and dysarthria statistical maps were created for each case using the method described in section IV.2.2 based on the Gaussian smoothed spherical shell kernel. Each statistical map was normalized so that the map maximum was set to 1. The high likelihood regions (HLR) for the maps were extracted. HLR of a map as defined earlier is the region of the map containing voxels with values at least 70% of the map maximum. The intensity centroid (similar to the center of mass) of the HLR was computed for each map. For every case, the following were computed for each of the 4 contacts: 1) value of each map at the location of the contact, 2) closest distance from the contact to the HLR of each map, 3) distance from the contact to the intensity centroid of the HLR of each map, 4) distance from the contact to the maximum value of each map. Using a combination of these, heuristic feature values (FV) were computed for predicting the optimal contact for every case. The predicted contact was compared against the clinically selected contact. This pipeline is shown in the flowchart in figure 36.

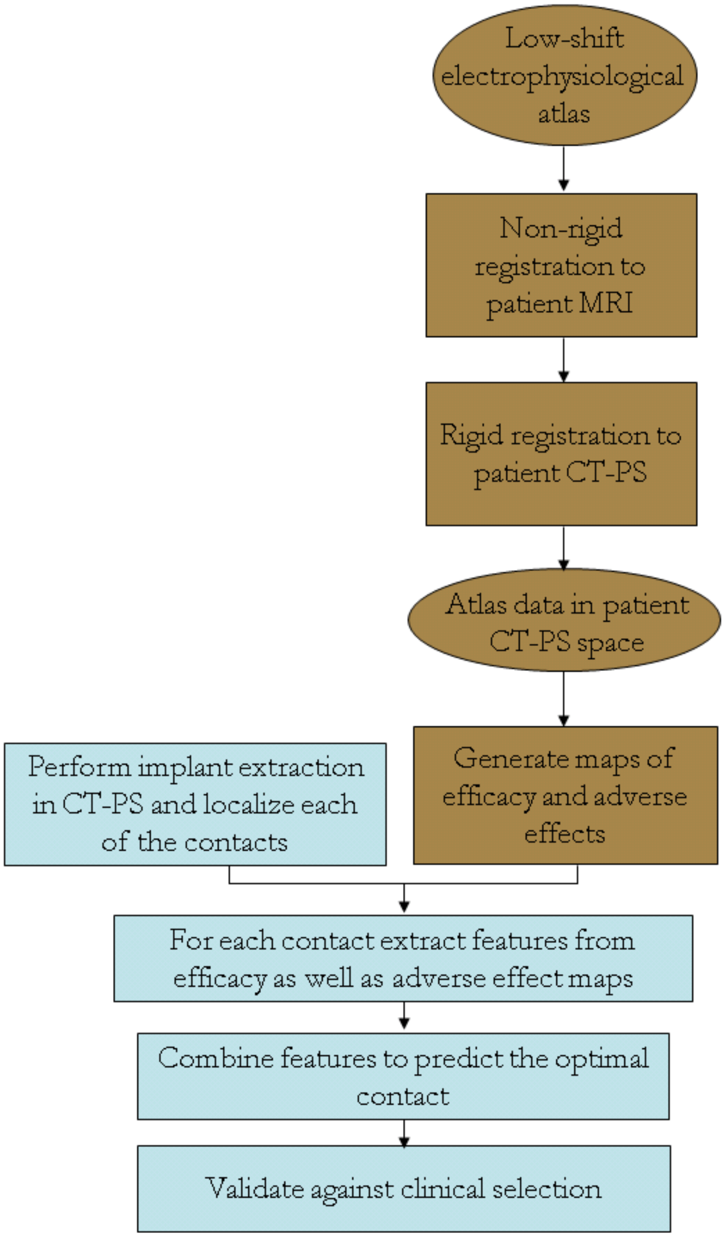

Figure 36. Pipeline to predict the optimal contact for DBS programming using statistical maps of efficacy and adverse effects.

Since efficacy is the primary measure of the success of programming, a component of efficacy was used in every feature value. The following heuristic feature values were computed for each of the 4 contacts on the implant, and the contact with the maximum value for a given feature was predicted as the optimal contact based on that feature.

1. FV_1: This feature value uses only the efficacy map and is simply the value of the efficacy map at the location of the contact (EFF_C).
2. FV_2: This feature also uses only the efficacy map. It is motivated by the heuristic that even if the high likelihood region of the map does not overlap with the contact, the information it provides about the proximity of the region likely to produce the corresponding stimulation response is valuable. Therefore, the closest distance from the contact to the HLR of the efficacy map (*EFF_HLR_closest_dist*) was chosen as a feature to identify the contact that could be most efficacious.
3. FV_3: As a variant of FV_2, this heuristic feature is examined based on the idea that the intensity centroid of the HLR of a map may represent greater confidence in producing the corresponding stimulation response than a point on the periphery of the HLR of the map. Therefore, the distance from the contact to the intensity centroid of the HLR of the efficacy map (*EFF_HLR_IntCentr_dist*) was chosen as a feature.
4. FV_4: This heuristic feature is the distance from the contact to the maximum value in the efficacy map (*EFF_MAX_dist*) and is examined because the location with the maximum map value represents the location that is statistically the most likely to produce the corresponding stimulation response.
5. FV_5: This feature combines the efficacy and dysarthria maps. It is based on the idea that it is desirable to have a larger efficacy map value (EFF_C) than dysarthria map value (DYS_C) at the contact, a large therapeutic window i.e. a

large separation between the HLR of the efficacy map (*EFF_HLR_closest_dist*) and the HLR of the dysarthria map (*DYS_HLR_closest_dist)*, and that the HLR of the efficacy map is closer to the contact than is the HLR of the dysarthria map. This is shown in equation 15 below.

$$FV_5 = \begin{Bmatrix} \dfrac{EFF_C}{DYS_C} * (DYS\_HLR\_closest\_dist - EFF\_HLR\_closest\_dist) \\ if \quad (DYS\_HLR\_closest\_dist - EFF\_HLR\_closest\_dist) > 0 \\ \\ 0, otherwise \end{Bmatrix} \quad (15)$$

6. FV$_6$: This feature is based on the same idea as FV$_5$ except that instead of the dysarthria map the paresthesia map is used as shown in equation 16 below. The paresthesia map value at the contact is referred to as PAR$_C$ and the HLR of the paresthesia map is referred to as *PAR_HLR_closest_dist*.

$$FV_6 = \begin{Bmatrix} \dfrac{EFF_C}{PAR_C} * (PAR\_HLR\_closest\_dist - EFF\_HLR\_closest\_dist) \\ if \quad (PAR\_HLR\_closest\_dist - EFF\_HLR\_closest\_dist) > 0 \\ \\ 0, otherwise \end{Bmatrix} \quad (16)$$

7. FV$_7$: This feature value defined in equation 19 uses all three maps (efficacy, dysarthria and paresthesia) together as shown in the equation below. T$_1$ is defined in equation 17 such that it is maximum when the efficacy map value at the contact is maximum and both the adverse effect maps have minimum values at the contact. T$_2$ defined in equation 18 is maximized when the distances between the contact and the HLRs of both adverse effects are

maximum and the distance between the contact and the HLR of the efficacy map is minimum. In T_2, the closest distances from the contact to the HLRs of each of the adverse effect maps are multiplied so that if the HLR of even one of the adverse effect maps is very close to the contact the feature value is smaller.

$$T_1 = \frac{EFF_C}{(DYS_C + PAR_C)} \quad (17)$$

$$T_2 = DYS\_HLR\_closest\_dist * PAR\_HLR\_closest\_dist - FV_2 \quad (18)$$

$$FV_7 = T_1 * T_2 \quad (19)$$

8. FV_8: This feature is an extension of FV_5 and FV_6. It uses all three maps (efficacy, dysarthria and paresthesia) together as shown in equation 20 below.

$$FV_8 = FV_5 + FV_6 \quad (20)$$

Predictions were first made using only the efficacy-map-based features (FV_1-FV_4) and their performance was evaluated. The prediction error was measured as the number of contacts by which the predicted contact was off from the clinically selected active contact. If the predicted contact matched exactly with the clinically selected contact then the error was referred to as 0-error. If the predicted contact was off by 1 contact then the error was referred to as 1-error. Similarly, 2-error and 3-error were defined. The efficacy-map-based feature that produced the best results was combined with the features of the adverse effect maps in multiple ways (FV_5-FV_8) to compute the predictions for all the cases. Then, the performance of all the features (FV_1-FV_8) was evaluated. For every feature, the mean, median and mode of the prediction error was computed. A cumulative distribution function showing the percentage of cases predicted within 0, 1, 2 and 3 contacts from the clinically selected contact was generated for each feature. An error of at most 1 contact (0-error or 1-error) is referred to as '<= 1-error'. Similarly, '<= 2-error' and '<= 3-error' are defined.

Additionally, for the feature that had the lowest prediction error, the second-best optimal contact was also predicted and the performance of the system when both the predictions are made available was evaluated.

VII.3 Results

Figure 37 shows the cumulative distribution of the optimal contact prediction error in 23 STN implants using efficacy-map-based features (FV_1, FV_2, FV_3 and FV_4). FV_2 had the best 0-error performance. Therefore, FV_2 was combined with features based on the adverse effect maps to compute FV_5, FV_6, FV_7 and FV_8. Figure 38 shows the mean, median and mode of prediction errors in 23 STN implants using each of the 8 features (FV_1 – FV_8). Both features FV_7 and FV_8 that used a combination of all the maps (efficacy, dysarthria and paresthesia) had marginally better performance on the mean prediction error than all the other features. The only clear improvement in using FV_7 or FV_8 over the other features is seen in the mode. Both had mode of 0. All other features had mode of 2 and FV_5 had mode of 1.

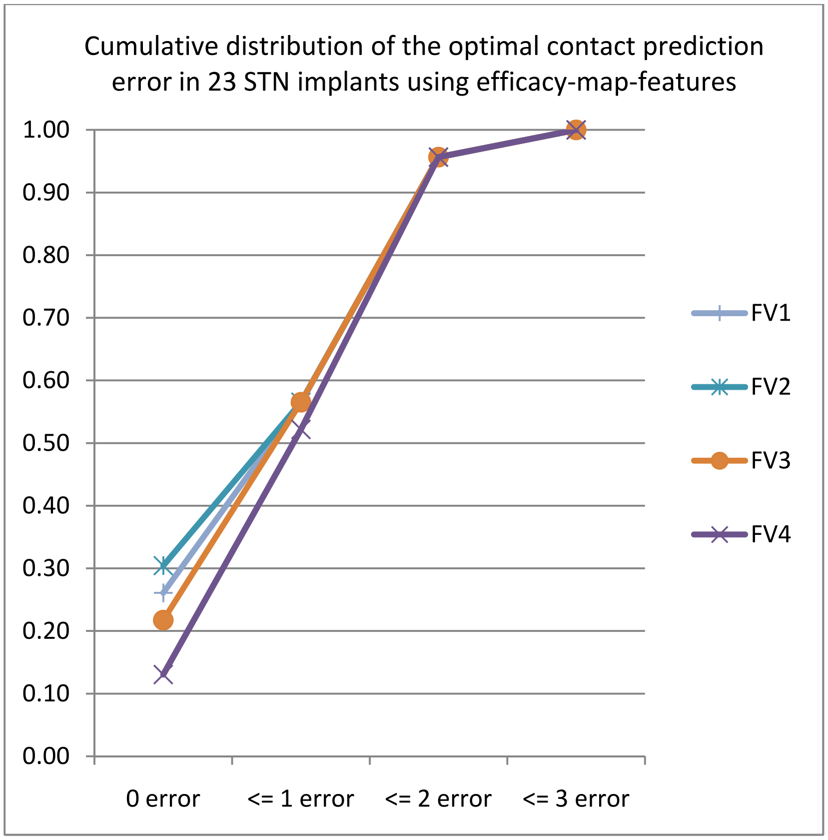

Figure 37. Cumulative distribution of the optimal contact prediction error in 23 STN implants for the efficacy-map-based features (FV_1, FV_2, FV_3 and FV_4).

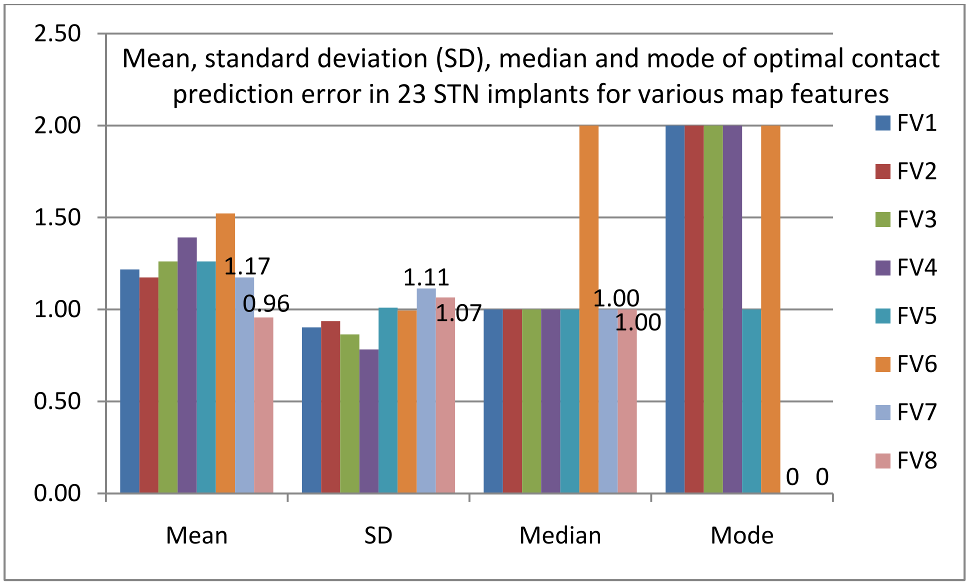

Figure 38. Bar graph showing the mean, standard deviation, median and mode of the optimal contact prediction errors for all the features.

Figure 39 shows the cumulative distribution of the prediction error in 23 STN implants for all the features (FV_1-FV_8). FV8 had more cases with 0 contact error than any other feature. FV_8 also had the more cases with at most 1 contact error than any other feature. Figure 40 shows the cumulative distribution of the prediction error in 23 STN implants when the best and second-best contacts predicted using FV_8 were compared with the clinically active contact. The predictive performance of feature FV_8 improved to 74% of the cases for 0-error and to 94% of the cases for at most 1 contact error.

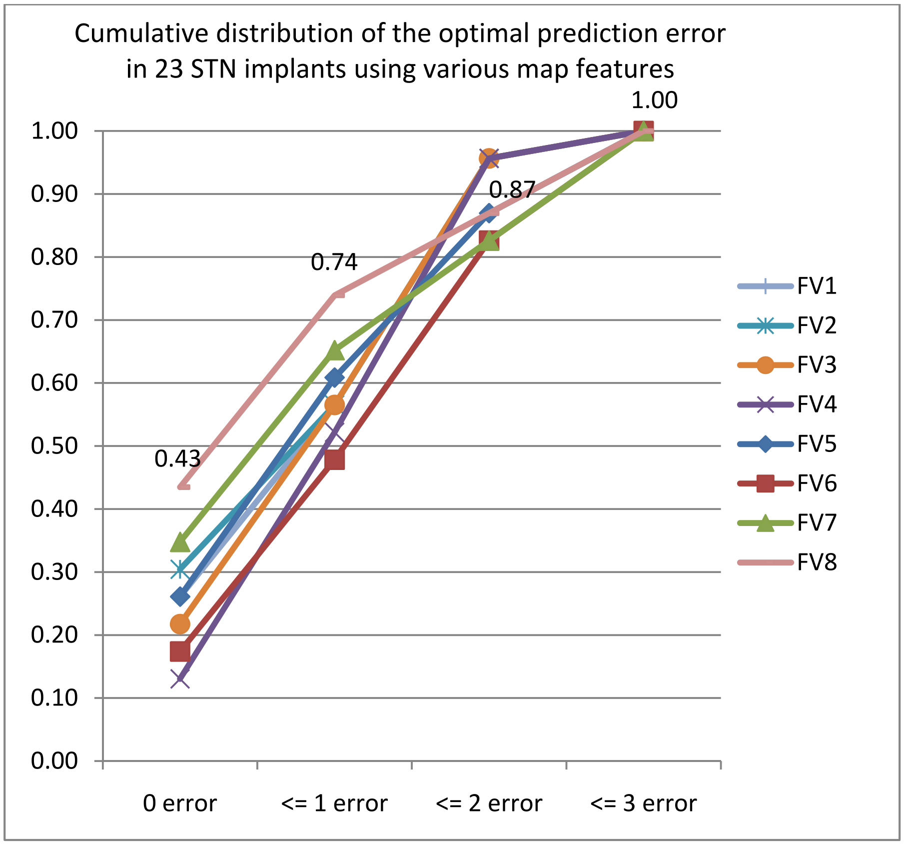

Figure 39. Cumulative distribution of the optimal contact prediction error in 23 STN implants for all the features.

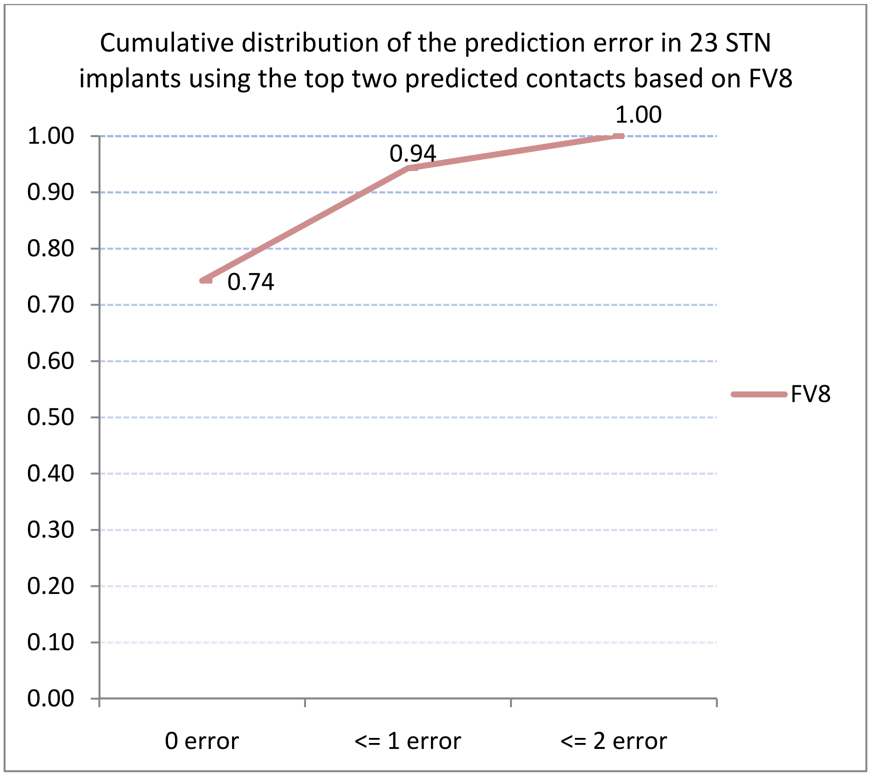

Figure 40. Cumulative distribution of the prediction error in 23 STN implants when the best and second-best contacts predicted using FV_8 were compared with the clinically active contact.

VII.4 Discussion and Conclusions

Randomly choosing one of the 4 contacts

When heuristic features are used in a predictive system, the baseline performance is typically established based on making selections at random. Let the automatic random predictions be denoted by 'A' and the neurologist's clinical selection be denoted by 'N'. The implant has 4 contacts labeled 0, 1, 2 and 3. Let $P_A(i)$ represent the probability of automatically choosing contact i. Let $P_N(j)$ represent the probability of the neurologist choosing contact j. Let E denote the prediction error defined as the absolute difference between the automatic random prediction and the neurologist's selection: $E = |i - j|$. For the random model it is assumed that every choice for A and N is equally likely. A random model is a good first approximation. Depending on the surgical practices of lead implantation it is possible that certain contacts are preferred over others. For instance, at Vanderbilt, the implant is typically centered at the optimal target with 2 contacts superior to it and 2 contacts inferior to it. This may prompt the neurologist to prefer the center two contacts over the bottommost and topmost contacts. However, the existence of such preference is not yet obvious in our data. It may be possible to extract reliable preferential patterns after grouping data by the operating surgeon and the programming neurologist over a period of time when practices remained unchanged.

Thus,

$$P_{\mathrm{A}}(i) = P_{\mathrm{N}}(j) = \frac{1}{4} \tag{21}$$

$$\text{where } i = 0, 1, 2, 3 \text{ and } j = 0, 1, 2, 3$$

Zero error (*E* = 0) occurs when both the atlas and the neurologist choose the same contact (*i* = *j*). Therefore,

$$P(E = 0) = \sum_{i=0}^{3} P_{\mathrm{A}}(i) P_{\mathrm{N}}(i) \tag{22}$$

Similarly,

$$P(E = 1) = P_{\mathrm{A}}(0)P_{\mathrm{N}}(1) + P_{\mathrm{A}}(1)P_{\mathrm{N}}(2) + P_{\mathrm{A}}(1)P_{\mathrm{N}}(0) + P_{\mathrm{A}}(2)P_{\mathrm{N}}(3) + P_{\mathrm{A}}(2)P_{\mathrm{N}}(1) + P_{\mathrm{A}}(3)P_{\mathrm{N}}(2) \tag{23}$$

$$P(E = 2) = P_{\mathrm{A}}(0)P_{\mathrm{N}}(2) + P_{\mathrm{A}}(1)P_{\mathrm{N}}(3) + P_{\mathrm{A}}(2)P_{\mathrm{N}}(0) + P_{\mathrm{A}}(3)P_{\mathrm{N}}(1) \tag{24}$$

$$P(E = 3) = P_{\mathrm{A}}(0)P_{\mathrm{N}}(3) + P_{\mathrm{A}}(3)P_{\mathrm{N}}(0) \quad (25)$$

$$P(E \leq 1) = P(E = 0) + P(E = 1) \quad (26)$$

$$P(E \leq 2) = P(E \leq 1) + P(E = 2) \quad (27)$$

$$P(E \leq 3) = P(E \leq 2) + P(E = 3) \quad (28)$$

Using equation 21 in equations 22 to 28, the cumulative distribution of the errors of automatic random predictions can be computed. Figure 41 compares the cumulative distribution of the optimal prediction results in 23 STN implants obtained using FV_8 and that obtained when making random predictions. FV_8 performs better than randomly choosing a contact both on the zero-error and at-most-one-error measures while the performance is almost the same for the two for the at-most-2- and at-most-3-error measures.

The mean error and the standard deviation (std) when making random selections are computed as follows:

$$\mathrm{mean}(E) = \sum_{i=0}^{3} \sum_{j=0}^{3} P_{\mathrm{A}}(i)P_{\mathrm{N}}(j)|i - j| \quad (29)$$

$$\mathrm{variance}(E) = \sum_{i=0}^{3} \sum_{j=0}^{3} P_{\mathrm{A}}(i)P_{\mathrm{N}}(j)\big(|i - j| - \mathrm{mean}(E)\big)^2 \quad (30)$$

$$\mathrm{std}(E) = \sqrt{\mathrm{variance}(E)} \quad (31)$$

The mean error when making random selections is 1.25. The mean error for feature FV_8 is 0.96, which represents a 23% advantage over random selection. The standard deviations of the two are comparable at 1.0 for random selection and 1.07 for FV_8.

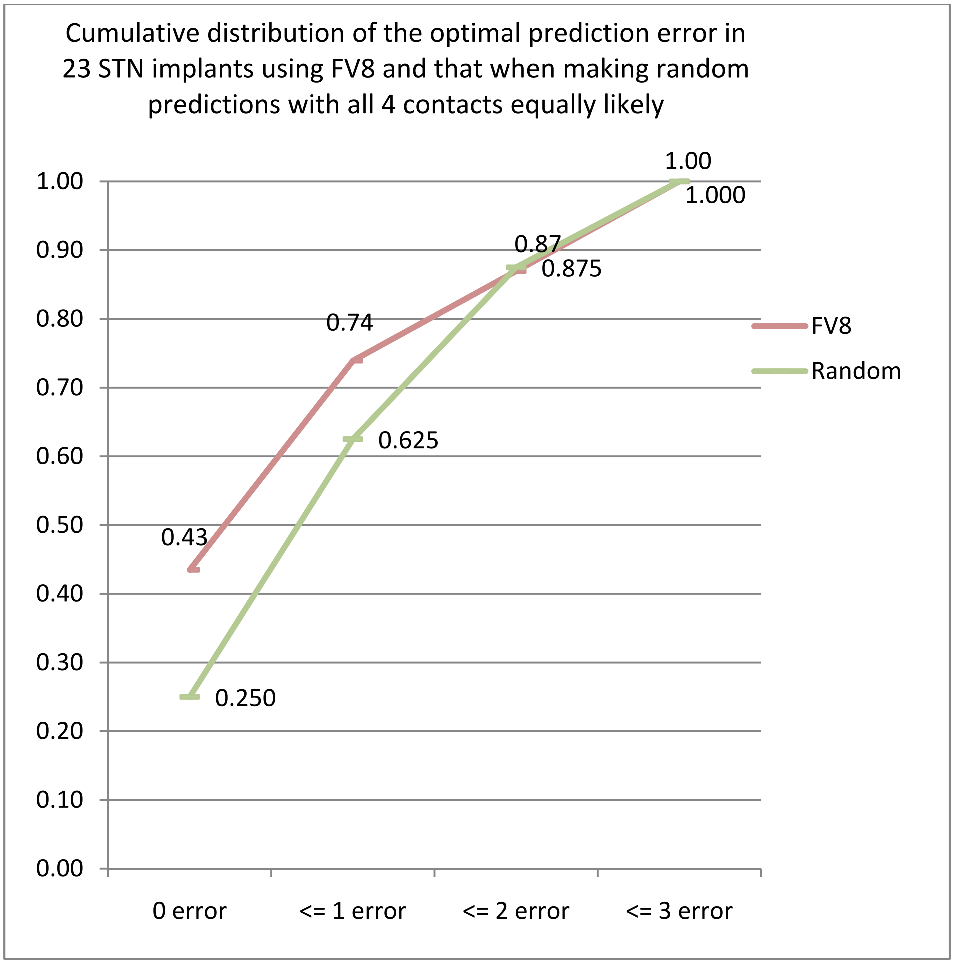

Figure 41. Cumulative distribution of the optimal prediction error in 23 STN implants using FV_8 and that obtained when making random predictions with all 4 contacts equally likely to be chosen.

To summarize, finding the optimal contact and programming parameters to maximize therapeutic benefit to the patient can be a challenging and time-consuming process in clinical practice. This is also taxing for the patient as the patient is required to be off medication during programming. Furthermore, neurologists programming the DBS implant must have expert knowledge of the electrophysiology of the area neighboring the implant. A system that can predict the optimal contact may be clinically useful to the neurologist and beneficial to the patient as well. In this chapter, statistical maps of stimulation response built using the new Gaussian smoothed spherical shell kernel and data from the low-shift electrophysiological atlas have been used for predicting the optimal contact in a population of patients. Although preliminary, the results suggest that using adverse effect maps in conjunction with the efficacy map reduces the optimal contact prediction error compared to that achieved by using only the efficacy map. Using a combination of efficacy, paresthesia and dysarthria maps, when the best and the second-best predicted contacts were used, in 74% of those cases there was 0-error with respect to the clinically selected contact. This suggests 50% reduction in programming time in those cases, but, these are preliminary results and it is difficult to draw strong conclusions from them. Predictions based on FV_8 were substantially better both on the 0-error and at-most-1-error measures than making random predictions.

Using statistical maps and other electrophysiological data projected on the patient using non-rigid registration holds promise for a number of reasons including the fact that it accounts for anatomical variability between patients. It also permits the possibility of not only predicting the optimal contact but also of providing the stimulation amplitude and stimulator settings needed to achieve the therapeutic benefit. More importantly, while choosing a single optimal contact manually for monopolar stimulation is a demanding task in itself, it is extremely complicated to arrive at an appropriate multipolar selection manually. Such a task may be feasible algorithmically based on the interaction of the region activated by multipolar stimulation with statistical maps and other forms of electrophysiological data. Therefore, a controlled experiment is needed which can help improve the predictive performance of the system. This can be done by having the statistical maps available during the programming sessions and comparing the information they provide with the actual clinical observations as well as by using the insight of the neurologists on the art of programming. The shortcoming and strengths of the system can thus be assessed and necessary changes can be made to improve the system.

While the results need further improvement and validation, it is important to note that there are certain issues surrounding the selection of the ground truth (clinical selection) itself and this impacts the assessment of the predictive performance of the system. Programming PD patients is complicated by the fact that in order to see the effects of stimulation the patients are made to go off medication for 24 hours prior to programming. This can be very stressful to them. Furthermore, it is not clear if 24 hours are sufficient to reduce the effects of medication to the extent that they do not interfere with the programming. If there is any interference from medication it has a direct effect on the patient's exam as well as on the patient's feedback to stimulation. Both of these can impact the selection of the optimal contact. Also, it is necessary to leave enough time between stimulating individual contacts in order to avoid transient effects from previously tested contacts from interfering with stimulation at the contact being tested currently. This not practical in the clinic due to limited time available for programming as well as due to patient discomfort from being off medication. There is also the possibility of inter-neurologist variability in defining the desired outcome. For instance, some neurologists choose a contact that produces the best efficacy while others prefer a contact with slightly inferior efficacy but larger therapeutic window. Also, it is often unclear from neurologist notes why a particular contact was preferred over another when both had similar performance. All these scenarios have a direct effect on the accuracy of the ground truth against which the predictions are compared and thus impact the evaluation of the predictive performance of the system. A prospective study is required where such variables can be controlled in order to have a robust and realistic assessment of the prediction performance of the system. Such a study can provide a reliable assessment of the clinical usefulness of such a system across a number of parameters including savings in programming time which is beneficial both to the patient and the neurologist, savings in battery life as well as the therapeutic benefit to the patient in the short and long terms.

CHAPTER VIII

SUMMARY AND FUTURE WORK

This chapter summarizes the main findings of this dissertation and discusses their implications. Several ideas for future research are also explored.

Chronic Deep Brain Stimulation (DBS) has been a rapidly evolving area of neurotherapeutics since its initial introduction for the treatment of Parkinson’s disease and essential tremor in the 1990s. For these conditions, DBS is now considered accepted therapy for patients failing to adequately respond to medical treatment. Since the 1990s, new clinical indications, anatomical targets, and technologies have contributed to an expanding role for DBS in the treatment of other movement disorders such as Dystonia and Tourette syndrome as well as for other neurologic disorders such as epilepsy and cluster headache. Early experience has also been reported for psychiatric syndromes, such as obsessive-compulsive disorders and depression [90]. With DBS attaining widespread acceptance, in the recent past, there has been active research to improve the outcome of the procedure as well as to make it more accessible to patients. To that end, a part of this dissertation is motivated by recent findings by other researchers [24, 26, 27, 34, 40, 43, 44, 58, 91-100] and contributes to the field of stereotactic functional neurosurgery in several ways.

This work can be broadly categorized into two parts. The first is motivated by a lack of standardization in the localization of popular landmarks used to indirectly localize as well as communicate the locations of stereotactic targets. The second is motivated by shortcomings and inaccuracies in existing methods to populate statistical atlases of electrophysiological data acquired intra-operatively during DBS surgeries. A general introduction to DBS as well as a survey of existing related works and their limitations was detailed in chapter I.

VIII.1 Standardizing AC-PC based indirect targeting in DBS surgery

Common targets of interest for DBS are poorly visible in current imaging modalities. Therefore, in normal clinical practice neurosurgeons pre-operatively localize targets indirectly. They do this by first selecting the anterior and posterior commissures (AC and PC) which are visible in the images. The targets are then localized based on their relative locations with respect to the AC and PC. The coordinates of the relative location can be from a variety of sources including a specific atlas or average location from a population of patients.

In chapter II, the variability in manual AC and PC selections by 43 neurosurgeons specialized in stereotactic neurosurgery from multiple centers was investigated. The impact this variability has on the localization of three popular DBS targets (STN, Vim and GPi) was also evaluated. The results presented in chapter II showed that inter-surgeon variability in manual selection of the AC and the PC was substantial and that this had a substantial impact on AC-PC based target localization. The mid-commissural point (MC) was found to be a more consistent reference point than AC and PC and was recommended as the preferred origin of the stereotactic reference system for communication of targets. It was found that based solely on the error in determining AC and PC, two neurosurgeons on average would select STN, Vim and GPi 2.64 mm, 2.75 mm and 3.31 mm apart respectively. This variability is substantial because the distance between adjacent contacts on a standard DBS electrode is only 1.5 mm. Variability in selection of the mid-plane (which was held constant in the original experiment) added a further 0.44 mm, 0.43 mm and 0.71 mm variability in selecting STN, Vim and GPi respectively. The images used in this study were high quality images and additional variability can be expected with poor image quality. Thus, in chapter II, the difficulty in establishing a common reference system to communicate locations of target points by manually selecting AC and PC on MRI images was highlighted. This study attains significance in the context of widespread use of AC and PC as stereotactic reference points. It serves to alert the surgical community to be cognizant of the potential effects of lack of standardization in selecting these points on contemporary images.

In Chapter III, an atlas-based technique [34] was applied to predict the locations of the commissures. The accuracy of the method was evaluated by comparing the predictions against 1) manual selections by 43 neurosurgeons from multiple centers, 2) a gold standard computed based on careful selections in a laboratory setting using 20 patients, and 3) manual selections by two neurosurgeons in a clinical setting over 60 patients.

With respect to the median of the manual selection by 43 neurosurgeons, the atlas-based predictions had sub-millimetric accuracy for AC, PC and MC, and consequently for AC-PC based localization of STN, Vim and GPi. With respect to the gold standard designed under laboratory controlled settings, the accuracy of AC, PC and MC predictions was sub-millimetric in 20 datasets. In a clinical setting, atlas-based prediction accuracy over 60 patients between 2 neurosurgeons was 1.07 mm, 0.94 mm and 0.82 mm for AC, PC and MC respectively. Statistical analysis suggested that atlas-based predictions were similar to an experienced neurosurgeon carefully selecting the points.

The results demonstrated that by carefully creating atlases containing AC and PC selections and by combining predictions from multiple atlases, a system could be developed that was not only fully automatic but also produced results that were more accurate and reproducible than those obtained by experienced physicians in clinical practice. This has a direct impact on the clinical practice of stereotactic neurosurgery as the AC-PC reference system continues to remain the popular choice for indirectly localizing and communicating targets. Using the approach validated in this chapter, variability in communicating targets based on AC-PC reference can be reduced. This may influence the outcome of procedures where AC-PC based targeting is used. Furthermore, using the standardized AC and PC predicted by this approach can impact the accuracy of atlases that use AC-PC based normalization methods to populate statistical data from patients.

VIII.2 Building accurate electrophysiological maps and atlases after accounting for intra-operative brain shift and using them for post-operative programming in DBS

In the recent past, a number of atlases and databases containing sub-cortical electrophysiological data of stimulation responses have been developed by various groups. A popular way to use such data from a population of patients was to combine them to create statistical maps that highlighted regions likely to produce a specific stimulation response. Previous method to build such maps using Gaussian kernels as proposed by our group [34] and used by others as well [37, 74] had certain limitations. In chapter IV, these shortcomings were identified and the Gaussian Smoothed Spherical Shell (GSSS) kernel was proposed as a new model to overcome them. Statistical maps built using the proposed GSSS kernels correlated strongly with a statistical ground truth, namely, the mean intra-operative implant position (IOIP) from a population of patients while those built using the previously used Gaussian (GAUSS) kernel correlated poorly. Specifically, the centroid of the high likelihood region (HLR) of the proposed GSSS-kernel-based PD efficacy map for the left side was 1.58 mm away from the mean IOIP while that of the old GAUSS-kernel-based PD efficacy map was 3.72 mm away. For the right side, the HLR centroid of the GSSS-kernel-based PD efficacy map was 1.31 mm away while the GAUSS-kernel-based PD efficacy map for the right side produced two HLRs which were on average 2.53 mm (SD 0.3 mm, maximum 2.74 mm) away from the corresponding mean IOIP. The HLR centroid of the GSSS-kernel-based ET efficacy map for the left side was 0.81 mm from the mean IOIP while the GAUSS-kernel-based ET efficacy map for the left side produced six HLRs which were on average 3.27 mm (SD 1.23 mm, maximum 5.47 mm) away from the corresponding mean IOIP. The HLR centroid of the GSSS-kernel-based ET efficacy map for the right side was 0.77 mm from the mean IOIP while the GAUSS-kernel-based ET efficacy map for the right side produced three HLRs which were on average 2.59 mm (SD 0.9 mm, maximum 3.55 mm) away from the corresponding mean IOIP. Additionally, the use no-efficacy as well as no-adverse-effect data to refine or trim the efficacy and adverse effect statistical maps respectively for better localization of the high likelihood regions was proposed. It was found to be very sensitive to the reliability of the no-response data.

Another problem with existing atlases of intra-operatively acquired data is that they all have an underlying assumption that anatomical structures do not move between the time of the pre-operative image acquisition and the time of the surgery. However, this assumption is not valid. Ignoring brain shift could lead to inaccuracies in the building of atlases and statistical maps built using data from such atlases. This can reduce the predictive value of systems that use such information. In chapter V, the effect of brain shift on the creation of atlases was studied using intra-operative electrophysiological data. In the absence of intra-operative imaging, a method to categorize patients into low, medium and large brain shift groups based on the amount of pneumocephalus seen on the CT acquired immediately after surgery was proposed. Clusters of micro-electrode recordings-based somatotopy data and stimulation response maps of efficacy for PD were analyzed for various brain shift groups. The results show that substantial brain shift happens before micro-electrode recordings in DBS. Specifically, the low-shift somatotopy cluster was 3.59 mm away from the large-shift cluster while it was 1.68 mm away from the medium-shift somatotopy cluster. Comparing the centroids of the HLRs, the low-shift efficacy map for right PD was 3.33 mm away from the large-shift efficacy map while it was 0.81 mm from the medium-shift efficacy map. For left PD, the low-shift efficacy map was 4.03 mm away from the large-shift efficacy map while it was 1.10 mm from the medium-shift map. Therefore, it was concluded that in order to build accurate atlases intra-operative brain shift that must be accounted for.

In chapter VI, the problem of accounting for intra-operative brain when building atlases of intra-operatively acquired electrophysiological data was addressed by eliminating patients with large brain shift from the atlas building process. Such an atlas was referred to as the low-shift-atlas. Also, the GSSS-kernel-based statistical maps built using data from the low-shift-atlas were validated in this chapter. The PD and ET efficacy maps were found to be in close proximity to the mean intra-operative implantation position (ground truth) from a population of patients projected onto the atlas MRI. The high likelihood region of the efficacy map built using successful ET relief data was found to be localized inside the Vim visible on the Schaltenbrand atlas. This is consistent with clear consensus in the stereotactic and functional neurosurgical community on Vim being the best anatomical target for ET relief. Similarly, it is well-understood in the neuro-electrophysiology community that stimulation in the Vc produces paresthesia. The high likelihood region of the paresthesia map was found to be localized inside the Vc visible on the Schaltenbrand atlas. Thus, in chapter VI, an approach to build electrophysiological atlases after accounting for brain shift was proposed and maps built using this method were validated. Additionally, a model showing the various stages and components of brain shift was described and a preliminary shift-correction scheme based the post-operative stable lead position was proposed.

In chapter VII, the use of statistical maps of efficacy and adverse effects for post-operative programming assistance was investigated. This preliminary study was motivated by the fact that in clinical practice finding the optimal contact and programming parameters to maximize therapeutic benefit to the patient is a challenging and time-consuming process to both the neurologist and the patient. A system that can predict the optimal contact may be clinically useful to the neurologist and beneficial to the patient as well. The results from this chapter suggested that using a combination of efficacy map in combination with maps of adverse effects like paresthesia and dysarthria produced better predictive performance than when only using efficacy maps. When the best and the second-best predicted contacts were compared against the clinically selected contact, prediction error was zero in 74% of the cases. While this may suggest 50% reduction in programming time in those cases, the results not only need further improvement and validation but they are also preliminary making it is difficult to draw strong conclusions from them. Furthermore, since the predictive system used heuristic features, its performance was compared against a system randomly selecting the optimal contact. The random selector had 0-error in 25% of the cases while the predictive system based on the statistical maps of efficacy and adverse effects had 0-error in 43% of the cases. For 1-error, these percentages were 62.5% and 74% for the random selector and the predictor based on statistical electrophysiological maps respectively.

VIII.3 Future work

The function governing the relationship between the stimulation amplitude and the radius of the spherical region activated by it that was used for building the statistical maps was based on data populated by Butson et al. for the Medtronic 3389 electrode which is a macro-electrode. However, the electrode used intra-operatively is a semi-macro electrode with slightly different dimensions and electrical properties. This can introduce some inaccuracies in the maps. A more precise function specific to the intra-operatively used electrode is required to improve the accuracy of the statistical maps. Another inaccuracy in the map building process is the assumption of isotropic tissue properties leading to the assumption of a spherical activation region. However, the electrical properties of brain tissue are not isotropic. To further improve the accuracy of the maps this has to be taken into account. The concept of a shell-based kernel will still remain valid except that the shape of the activation region may not necessarily be a sphere anymore.

To avoid eliminating large-shift patients from the process of building electrophysiological atlases least affected by brain shift, the brain shift recovery assumptions necessary for the use of the post-operative stable lead (section VI.4) for brain shift correction need to be validated. Additionally, it may be feasible to use intra-operative CTs to study the evolution of brain shift as the surgery progresses so that new models of brain shift can be developed and used to build more accurate shift-corrected atlases.

In the absence of intra-operative imaging, intra-operative electrophysiological recordings are the only source of information available to the surgical team to navigate towards the optimal target. In the event of large brain shift during the procedure these recordings can be expected to correlate poorly with the anatomical information available in the pre-operative images used for planning the procedure and can thus make it difficult for the surgical team to reach the optimal target. It may thus be beneficial to the surgical team if the occurrence of intra-operative brain shift can at least be detected, if not corrected automatically. One way to do that is to correlate the statistical electrophysiological maps built using data from the low-shift electrophysiological atlas with intra-operative observations. Preliminary results on the use of low-shift maps for intra-operative brain shift detection were presented recently [101]. Further work is necessary in this direction as well as towards intra-operative navigation using electrophysiological atlases.

Post-operatively, the severity of the disease can be assessed using scales like the UPDRS rating scale to objectively evaluate any differences in the therapeutic benefit to patient when using the predicted contact as opposed to a different clinically selected contact. Also, as discussed in section VII.4 there are issues surrounding the selection of the ground truth (clinical selection) that affect the assessment of the predictive performance of the system. A well-designed prospective study where these issues can be controlled is required to not only improve methods for using the statistical maps and other forms of electrophysiological data for post-operative programming assistance, but also to assess their predictive performance. Furthermore, neurologist typically use monopolar stimulation, i.e. they activate only one of the multiple contacts at a given time as this is already quite challenging because visualizing the electric field produced by the stimulation is not trivial especially when the spatially varying electrical properties of the brain tissue need to be taken into account. It is even more difficult to arrive at optimal multipolar stimulator settings because of the complexity of the interaction between the electric fields produced by the activation of more than one contact simultaneously. Thus, there is tremendous potential in the direction automatically predicting multipolar stimulation in order to modulate the electric fields so that they can be shaped to conform to the target known to produce efficacy while avoiding interaction with neighboring structures known to induce adverse effects.

REFERENCES

[1] Medtronic, "Movement disorders fact sheet," in © *Medtronic Inc.*, 2009.

[2] "Michael J. Fox Foundation and the Parkinson's Action Network."

[3] E. B. J. Montgomery and K. B. Baker, "Mechanisms of deep brain stimulation and future technical developments," *Neurol Res* vol. 22, p. 259:266, 2000.

[4] W. M. Grill, A. N. Snyder, and S. Miocinovic, "Deep brain stimulation creates an informational lesion of the stimulated nucleus," *Neuroreport* vol. 15, p. 1137:1140, 2004.

[5] J. E. Rubin and D. Terman, "High frequency stimulation of the subthalamic nucleus eliminates pathological thalamic rhythmicity in a computational model " *J Comput Neurosci* vol. 16, p. 211:235, 2004.

[6] B. Schrader, W. Hamel, D. Weinert, and H. M. Mehdorn, "Documentation of electrode localization," *Movement Disorders,* vol. 17:suppl 3, p. S167:S174, 2002.

[7] G. Deuschl, J. Volkmann, and P. Krack, "Deep brain stimulation for movement disorders," *Mov Disord,* vol. 17: S3, p. S1, 2002.

[8] G. Deuschl, R. Wenzelburger, F. Kopper, and J. Volkmann, "Deep brain stimulation of the subthalamic nucleus for Parkinson's disease: a therapy approaching evidence-based standards," *J Neurology,* vol. 250:[Suppl 1], p. I/43:I/46, 2003.

[9] P. A. Starr, "Placement of deep brain stimulators in subthalamic nucleus or globus pallidus internus: Technical approach," *Stereotact Funct Neurosurg,* vol. 79, p. 118:145, 2002.

[10] E. Papavassiliou, G. Rau, S. Heath, A. Abosch, N. M. Barbaro, P. S. Larson, K. Lamborn, and P. A. Starr, "Thalamic deep brain stimulation for essential tremor: relation of lead location to outcome," *Neurosurgery,* vol. 54, p. 1120:1130, 2004.

[11] J. Talairach and P. Tournoux, *Co-Planar Stereotaxic Atlas of the Human Brain*. Stuttgart, Germany: Thieme Publishing Group, 1988.

[12] G. Schaltenbrand and W. Wahren, *Atlas for stereotaxy of the human brain*. Stuttgart, Germany: Thieme: Thieme, 1977.

[13] J. Yelnik, E. Bardinet, D. Dormont, G. Malandain, S. Ourselin, D. Tandé, C. Karachi, N. Ayache, P. Cornu, and Y. Agid, "A three-dimensional, histological and deformable atlas of the human basal ganglia. I. Atlas construction based on immunohistochemical and MRI data," *Neuroimage,* vol. 34, p. 618:638, 2007.

[14] E. Bardinet, M. Bhattacharjee, D. Dormont, B. Pidoux, G. Malandain, M. Schüpbach, N. Ayache, P. Cornu, Y. Agid, and J. Yelnik, "A three-dimensional histological atlas of the human basal ganglia. II. Atlas deformation strategy and evaluation in deep brain stimulation for Parkinson disease," *J Neurosurg,* vol. 110, p. 208:219, 2009.

[15] M. M. Chakravarty, G. Bertrand, C. P. Hodge, A. F. Sadikot, and D. L. Collins, "The Creation of a Brain Atlas for Image guided Neurosurgery Using Serial Histological Data," *NeuroImage,* vol. 30:2, p. 359:376, 2006.

[16] M. M. Chakravarty, A. F. Sadikot, S. Mongia, G. Bertrand, and D. L. Collins, "Towards a multi-modal atlas for neurosurgical planning," in *Lecture Notes in Computer Science, MICCAI*. vol. 4191, 2006, p. 389:396.

[17] P. St-Jean, A. F. Sadikot, D. L. Collins, D. Clonda, R. Kasrai, A. C. Evans, and T. M. Peters, "Automated atlas integration and interactive 3-dimensional visualization tools for planning and guidance in functional neurosurgery," *IEEE Trans. Med. Imag,* vol. 17, p. 672:680, 1998.

[18] K. A. Ganser, H. Dickhaus, R. Metzner, and C. R. Wirtz, "A Deformable Digital Brain Atlas System according to Talairach and Tournoux," *Med. Imag. Analy.,* vol. 8:1, pp. 3-22, 2004.

[19] W. L. Nowinski, G. L. Yang, and T. T. Yeo, "Computer-Aided Stereotactic Functional Neurosurgery Enhanced by the Use of the Multiple Brain Atlas Database," *IEEE Trans. Med. Imag.,* vol. 19:1, p. 62:69, 2000.

[20] R. R. Tasker, L. W. Organ, and P. A. Hawrylyshyn, *The Thalamus and Midbrain of Man*. Springfield, IL: Charles C Thomas, 1982.

[21] M. M. Lanotte, M. Rizzone, B. Bergamasco, G. Faccani, A. Melcarne, and L. Lopiano, "Deep brain stimulation of the subthalamic nucleus: anatomical, neurophysiological, and outcome correlations with the effects of stimulation," *J Neurol Neurosurg Psychiatry,* vol. 72:1, p. 53:58, 2002.

[22] P. Plaha, Y. Ben-Shlomo, N. K. Patel, and S. S. Gill, "Stimulation of the caudal zona incerta is superior to stimulation of the subthalamic nucleus in improving contralateral parkinsonism " *Brain,* vol. 129, pp. 1732-1747, 2006.

[23] Y. M. Andrade-Souza, J. M. Schwalb, C. Hamani, H. Eltahawy, T. Hoque, J. Saint-Cyr, and A. M. Lozano, "Comparison of three methods of targeting the subthalamic nucleus for chronic stimulation in Parkinson's disease," *Neurosurgery,* vol. 62 (Suppl 2), p. 875:883, 2008.

[24] C. B. Maks, C. R. Butson, B. L. Walter, J. L. Vitek, and C. C. McIntyre, "Deep brain stimulation activation volumes and their association with neurophysiological mapping and therapeutic outcomes," *Neurol. Neurosurg. Psychiatry,* vol. Online: 16 Jan, 2009, DOI: 10.1136/jnnp.2007.126219, 2009.

[25] M. Zonenshayn, A. R. Rezai, A. Y. Mogilner, A. Beric, D. Sterio, and P. Kelly, "Comparison of anatomic and neurophysiological methods for subthalamic nucleus targeting," *Neurosurgery,* vol. 47 (2), p. 282:292, 2000.

[26] W. L. Nowinski, D. Belov, P. Pollak, and A. L. Benabid, "Statistical Analysis of 168 Bilateral Subthalamic Nucleus Implantations by Means of the Probabilistic Functional Atlas," *Neurosurgery,* vol. 57:4, p. 319:330, 2005.

[27] K. W. Finnis, Y. P. Starreveld, A. G. Parrent, A. F. Sadikot, and T. M. Peters, "Three dimensional database of subcortical electrophysiology for image-guided stereotactic functional neurosurgery," *IEEE Trans. on Medical Imaging,* vol. 22:11, p. 93:104, 2003.

[28] P.-F. D’Haese, E. Cetinkaya, P. E. Konrad, C. Kao, and B. M. Dawant, "Computer-Aided Placement of Deep Brain Stimulators: From Planning to Intraoperative Guidance," in *IEEE Trans. on Medical Imaging*. vol. 24 (11), 2005, p. 1469:1478.

[29] P.-F. D'Haese, S. Pallavaram, C. Kao, P. E. Konrad, and B. M. Dawant, "Automatic selection of DBS target points using multiple electrophysiological atlases," in *LNCS (MICCAI): 3750*. vol. 3750, 2005, p. 427:434.

[30] T. Guo, K. W. Finnis, S. C. L. Deoni, A. G. Parrent, and T. M. Peters, "Comparison of Different Targeting Methods for Subthalamic Nucleus Deep Brain Stimulation," in *MICCAI*: LNCS, 2006, pp. 4190: 768 – 775.

[31] K. W. Finnis, Y. P. Starreveld, A. G. Parrent, A. F. Sadikot, and T. M. Peters, "Application of a population based electrophysiological database to the planning and guidance of deep brain stereotactic neurosurgery," in *MICCAI*, 2002.

[32] F. J. Castro, C. Pollo, O. Cuisenaire, J.-G. Villemure, and J.-P. Thiran, "Validation of experts versus atlas-based and automatic registration methods for subthalamic nucleus targeting on MRI. ," *International Journal of Computer Assisted Radiology and Surgery,* vol. 1 (1), p. 5:12, 2006.

[33] F. J. Castro, C. Pollo, R. Meuli, P. Maeder, O. Cuisenaire, M. B. Cuadra, J.-G. Villemure, and J.-P. Thiran, "A cross validation study of deep brain stimulation targeting: from experts to atlas-based, segmentation-based and automatic registration algorithms," *IEEE Trans Med Imaging,* vol. 25(11), p. 1440:50, 2006, Nov.

[34] P.-F. D'Haese, E. Cetinkaya, P. E. Konrad, C. Kao, and B. M. Dawant, "Computer-Aided Placement of Deep Brain Stimulators: From Planning to Intraoperative Guidance," in *IEEE Trans. on Medical Imaging*. vol. 24 (11), 2005, p. 1469:1478.

[35] G. K. Rohde, A. Aldroubi, and B. M. Dawant, "The adaptive bases algorithm for intensity-based nonrigid image registration," *IEEE Trans. On Medical Imaging,* vol. 22:11, p. 1470:1479, 2003.

[36] J. P. Pluim, J. B. Maintz, and M. A. Viergever, "Mutual-Information-Based Registration of Medical Images: A Survey," *IEEE Trans Med Imaging,* vol. 22 (8), p. 986:1004, 2003.

[37] T. Guo, A. G. Parrent, and T. M. Peters, "Automatic target and trajectory identification for deep brain stimulation (DBS) procedures," *LNCS (MICCAI),* vol. 4791, pp. 483-490, 2007.

[38] F. U. Gerdes, G. Klein, M. Nadjmi, and G. Schaltenbrand, "[X-ray studies of the brain as a basis for stereotaxy (author's transl)]," *J Neurol,* vol. 210, p. 183:190, 1975.

[39] K. Wester and J. Krankenes, "Vertical displacement of the brain and the target area during open stereotaxic neurosurgery," *Acta Neurochir,* vol. 143, p. 603:606, 2001.

[40] D. Winkler, M. Tittgemeyer, J. Schwarz, C. Preul, K. Strecker, and J. Meixensberger, "The first evaluation of brain shift during functional neurosurgery by deformation field analysis," *J Neurol Neurosurg Psychiatry,* vol. 76, p. 1161:1163, 2005.

[41] M. F. Khan, K. Mewes, and O. Skrinjar, "Brain shift analysis for deep brain stimulation surgery," in *ISBI* Virginia, USA: IEEE, 2006, p. 654:657.

[42] A. J. Martin, P. S. Larson, J. L. Ostrem, W. Sootsman, P. Talke, O. M. Weber, N. Levesque, J. Myers, and P. A. Starr, "Placement of deep brain stimulator electrodes using real-time highfield interventional magnetic resonance imaging," *Magn Reson Med,* vol. 54, p. 1107:1114, 2005.

[43] M. F. Khan, K. Mewes, R. E. Gross, and O. Škrinjar, "Assessment of Brain Shift Related to Deep Brain Stimulation Surgery," *Stereotact Funct Neurosurgery,* vol. 86, pp. 44–53, 2008.

[44] Y. Miyagi, F. Shima, and T. Sasaki, "Brain shift: an error factor during implantation of deep brain stimulation electrodes," *Neurosurgery,* vol. 107, pp. 989–997, 2007.

[45] C. H. Halpern, S. F. Danish, G. H. Baltuch, and J. L. Jaggi, "Brain Shift during Deep Brain Stimulation Surgery for Parkinson's Disease," *Stereotact Funct Neurosurg,* vol. 86, pp. 37–43, 2008.

[46] T. Rohlfing, C. Maurer, D. Dean, and E. J. Maciunas, "Effect of changing patient position from supine to prone on the accuracy of a Brown-Roberts-Wells stereotactic head frame system," *Neurosurg Online,* vol. 52, p. 610:618, 2003.

[47] The_Deep-BrainStimulation_for_Parkinson's_Disease_Study_Group, "Deep-Brain Stimulation of the Subthalamic Nucleus or the Pars Interna of the Globus Pallidus in Parkinson's Disease," *N Engl J Med,* vol. 345, p. 956:963, 2001.

[48] W. L. Nowinski, D. Belov, and A. L. Benabid, "An Algorithm for Rapid Calculation of a Probabilistic Functional Atlas of Subcortical Structures from Electrophysiological Data Collected during Functional Neurosurgery Procedures," *NeuroImage,* vol. 18, p. 143:155, 2003.

[49] S. Pallavaram, P.-F. D'Haese, C. Kao, H. Yu, M. Remple, J. S. Neimat, P. E. Konrad, and B. M. Dawant, "A new method for creating electrophysiological

maps for DBS surgery and their application to surgical guidance," in *LNCS (MICCAI), Part1*. vol. 5241: Springer-Verlag, 2008, p. 670:677.

[50] O. Skrinjar, A. Nabavi, and J. Duncan, "Model-driven brain shift compensation," *Med Image Analysis,* vol. 6, p. 361:373, 2002.

[51] P. Limousin, P. Krack, P. Pollack, A. Benazzouz, L. Ardouin, D. Hoffman, and A. L. Benabid, "Electrical stimulation of the subthalamic nucleus in advanced Parkinson's disease," *N Engl J Med,* vol. 339, p. 1105:1111, 1998.

[52] M. I. Hariz, "Complications of deep brain stimulation surgery," *Mov Disord.,* vol. 17 (suppl 3), p. S167:S174, 2002.

[53] A. Gironell, G. Amirian, J. Kulisevsky, and J. Molet, "Usefulness of an Intraoperative Electrophysiological Navigator System for Subthalamic Nucleus Surgery in Parkinson's Disease," *Stereotact Funct Neurosurg,* vol. 83, p. 101:107, 2005.

[54] B. M. Dawant, P.-F. D'haese, S. Pallavaram, R. Li, H. Yu, J. Spooner, T. Davis, C. Kao, and P. E. Konrad, "The VU-DBS project: integrated and computer-assisted planning, intra-operative placement, and post-operative programming of deep-brain stimulators," in *SPIE Medical Imaging 2007: Visualization and Image-Guided Procedures*. vol. 6509, 2007, p. 650907.

[55] W. L. Nowinski, "Towards construction of an ideal stereotactic brain atlas," *Acta Neurochir (Wien),* vol. 150 (1), p. 1:13; discussion 13:14, 2008.

[56] C. R. Butson, S. E. Cooper, J. M. Henderson, and C. C. McIntyre, "Patient-specific analysis of the volume of tissue activated during deep brain stimulation," in *NeuroImage*. vol. 34, 2007, p. 661:670.

[57] C. R. Butson and C. McIntyre, "Role of electrode design on the volume of tissue activated during deep brain stimulation," in *Neural Eng*. vol. 3, 2006, p. 1:8.

[58] C. R. Butson and C. C. McIntyre, "Current steering to control the volume of tissue activated during deep brain stimulation," *Brain Stimulation,* vol. 1:1, p. 7:15, 2008.

[59] S. Pallavaram, H. Yu, J. Spooner, P.-F. D'Haese, B. Bodenheimer, P. E. Konrad, and B. M. Dawant, "Inter-surgeon variability in the selection of anterior and posterior commissures and its potential effects on target localization," *Stereotact Funct Neurosurgery,* vol. 86:2, p. 113:119, 2008.

[60] S. Pallavaram, H. Yu, J. Spooner, P.-F. D'Haese, T. Koyama, B. Bodenheimer, P. E. Konrad, and B. M. Dawant, "Automated selection of anterior and posterior commissures based on a deformable atlas and its evaluation based on manual selections by neurosurgeons," in *SPIE Medical Imaging*. vol. 6509 San Diego, USA, 2007, p. 65091C:1:9.

[61] P. Anbazhagan, A. Carass, P.-L. Bazin, and J. L. Prince, "Automatic estimation of midsagittal plane and AC-PC alignment based on nonrigid registration," in *IEEE Int Symp on Biomed Imaging* Arlington, 2006, p. 828:831.

[62] Y. Han and H. W. Park, "Automatic Brain MR Image Registration Based on Talairach Reference System," in *Int Conf on Image Processing (ICIP)*, 2003, p. I1097:I1100.

[63] L. Verard, P. Allian, J. M. Travere, J. C. Baron, and D. Bloyet, "Fully Automatic Identification of AC and PC Landmarks on Brain MRI using Scene Analysis," *IEEE Trans. Medical Imaging,* vol. 16, p. 610:616, 1997.

[64] S. Pallavaram, B. M. Dawant, T. Koyama, H. Yu, J. S. Neimat, P. E. Konrad, and P.-F. D’Haese, "Validation of a fully automatic method for the routine selection of the anterior and posterior commissures in MR images," *Journal of Stereotact Funct Neurosurg,* vol. 87, p. 148:154, 2009.

[65] F. Maes, A. Collignon, and P. Suetens, "Multimodality image registration by maximization of mutual information," in *IEEE Trans on Medical Imaging*. vol. 16 (2), 1997, p. 187:198.

[66] W. M. Wells, P. Viola, H. Atsumi, S. Nakajima, and R. Kikinis, "Multi-modal volume registration by maximization of mutual information," in *Medical Image Analysis*. vol. 1 (1), 1996, p. 35:52

[67] T. Rohlfing, D. B. Russakoff, and C. R. Maurer, "Performance-based classifier combination in atlas-based image segmentation using Expectation-Maximization parameter estimation," *IEEE Trans on Medical Imaging,* vol. 23:8, p. 983:994, 2004.

[68] S. K. Warfield, K. H. Zou, and W. M. Wells, "Simultaneous Truth and Performance Level Estimation (STAPLE): An algorithm for the validation of image segmentation," in *IEEE Trans on Medical Imaging*. vol. 23 (7), 2004, p. 903:921.

[69] A. Guimond, J. Meunier, and J. P. Thirion, "Average brain models: a convergence study," *Comput Vis Image Understand,* vol. 77:9, p. 192:210, 2000.

[70] P.-F. D'Haese, S. Pallavaram, K. Niermann, J. Spooner, C. Kao, P. E. Konrad, and B. M. Dawant, "Automatic selection of DBS target points using multiple electrophysiological atlases," *LNCS (MICCAI),* vol. 3750, pp. 427-34, 2005.

[71] R Development Core Team, "R: A language and environment for statistical computing.," in *R Foundation for Statistical Computing* Vienna, Austria, 2008.

[72] P.-F. D'Haese, "Creation of an electrophysiological atlas for the planning and guidance of Deep Brain Stimulators (DBS) implantation," in *School of Engineering (Communications and Remote Sensing Laboratory)*. vol. Ph.D. dissertation: Louvain-la-Neuve, Belgium: Université Catholique de Louvain, 2005.

[73] P.-F. D'Haese, S. Pallavaram, H. Yu, J. Spooner, P. E. Konrad, and B. M. Dawant, "Deformable Physiological Atlas-Based Programming of Deep Brain Stimulators: A Feasibility Study," in *LNCS (WBIR)*. vol. 4057 Utrecht, The Netherlands, 2006, p. 144:150.

[74] T. Guo, K. W. Finnis, A. G. Parrent, and T. M. Peters, "Visualization and Navigation System Development and Application for Stereotactic Deep-Brain Neurosurgeries," *Computer Aided Surgery,* vol. 11(5), p. 231:239, 2006.

[75] J. M. Fitzpatrick, P. E. Konrad, C. Nickele, and E. Cetinkaya, "Accuracy of customized miniature stereotactic platforms," *Stereotactic Functional Neurosurgery,* vol. 83, pp. 25–31, 2005.

[76] R. Balachandran, J. Mitchell, B. M. Dawant, and J. M. Fitzpatrick, "Accuracy evaluation of MicroTargeting™ platforms for deep-brain stimulation using virtual targets," in *Trans on Biomedical Engineering*. vol. 56 (1), Jan 2009, p. 37:44.

[77] P.-F. D’Haese, S. Pallavaram, P. E. Konrad, J. S. Neimat, J. M. Fitzpatrick, and B. M. Dawant, "Clinical accuracy of a customized stereotactic platform for deep-

brain stimulation after accounting for brain shift," in *Journal of Stereotac Funct Neurosurg*. vol. 88, 2010, p. 81:87.

[78] S. Pallavaram, B. M. Dawant, M. Remple, J. S. Neimat, C. Kao, P. E. Konrad, and P.-F. D’Haese, "Effect of brain shift on the creation of functional atlases for deep brain stimulation surgery " in *International Journal of Computer Assisted Radiology and Surgery*. vol. 5 (3): Springer Berlin / Heidelberg, 2010 (Published online: Aug' 2, 2009), p. 221:228.

[79] S. Pallavaram, B. M. Dawant, M. Remple, J. S. Neimat, C. Kao, P. E. Konrad, and P.-F. D’Haese, "Effect of intra-operative brain shift on populating electrophysiological atlases of somatotopy recordings in DBS surgeries," in *World Society for Stereotactic and Functional Neurosurgery (WSSFN) - 15th Quadrennial meeting,* Toronto, Canada, 2009.

[80] S. Pallavaram, B. M. Dawant, M. Remple, J. S. Neimat, C. Kao, P. E. Konrad, and P.-F. D’Haese, "Effect of brain shift on the creation of functional atlases for deep brain stimulation surgery," in *Computer Aided Radiology and Surgery (CARS)*, Germany, 2009.

[81] B. P. Rosenbaum, P.-F. D’Haese, H. Yu, S. Pallavaram, B. M. Dawant, J. S. Neimat, and P. E. Konrad, "Brain Shift during Deep Brain Stimulation Surgery Correlates Directly to Pneumocephalus and Inversely to Age," in *American Society of Sterotactic and Functional Neurosurgery (ASSFN) Biennial meeting* Vancouver, BC, Canada, 2008.

[82] S. Pallavaram, P.-F. D’Haese, M. Remple, J. S. Neimat, C. Kao, P. E. Konrad, and B. M. Dawant, "A method to correct for brain shift when building

electrophysiological atlases for deep brain stimulation (DBS) surgery," *LNCS(MICCAI, London),* vol. 5761, p. 557:564, 2009.

[83] O. Sydow, S. Thobois, F. Alesch, and J. Speelman, "Multicentre European study of thalamic stimulation in essential tremor: a six year follow up," *Neurol, Neurosurg Psychiatry,* vol. 74 (10), 2003.

[84] A. M. Lozano, "Vim Thalamic Stimulation for Tremor," *Archives of Medical Research,* vol. 31 (3), p. 266:269, 2000.

[85] M. P. Conn, *Neuroscience in medicine* 2nd ed. Totowa, NJ: Humana Press.

[86] B. A. Wallace, K. Ashkan, and A.-L. Benabid, "Deep brain stimulation for the treatment of chronic, intractable pain," *Neurosurg Clin N Am,* vol. 15, p. 343:357, 2004.

[87] T. Fukushima, Y. Mayanagi, and G. Bouchard, "Thalamic evoked potentials to somatosensory stimulation in man," *Electroencephalogr Clin Neurophysiol.,* vol. 40 (5), p. 481:490, 1976.

[88] P. Pollak, P. Krack, V. Fraix, A. Mendes, E. Moro, S. Chabardes, and A. L. Benabid, "Intraoperative micro- and macrostimulation of the subthalamic nucleus in Parkinson's disease," *Mov Disord,* vol. 17 (Suppl 3), p. S155:161, 2002.

[89] J. Volkmann, J. Herzog, F. Kopper, and G. Deuschl, "Introduction to the programming of deep brain stimulation," *Mov Disord,* vol. 17, p. S181:S187, 2002.

[90] D. Tarsy, J. L. Vitek, P. A. Starr, and M. S. Okun, *Deep Brain Stimulation in Neurological and Psychiatric Disorders*, 1st ed.: Humana Press, 2008.

[91] T. Guo, K. W. Finnis, A. G. Parrent, and T. M. Peters, "Development and application of functional databases for planning deep-brain neurosurgical procedures," *LNCS (MICCAI),* vol. 3749, pp. 835-842, 2005.

[92] C. R. Butson, S. E. Cooper, J. M. Henderson, and C. C. McIntyre, "Patient-speciftic analysis of the volume of tissue activated during deep brain stimulation," *NeuroImage,* vol. 34, pp. 661-670, Jan 15 2007.

[93] C. C. McIntyre, S. Mori, D. L. Sherman, N. V. Thakor, and J. L. Vitek, "Electric field and stimulating influence generated by deep brain stimulation of the subthalamic nucleus," *Clinical Neurophysiology,* vol. 115, pp. 589-595, Mar 2004.

[94] S. Miocinovic, A. M. Noecker, C. B. Maks, C. R. Butson, and C. C. McIntyre, "Cicerone: stereotactic neurophysiological recording and deep brain stimulation electrode placement software system," *Acta Neurochir Suppl,* vol. 97 (2), p. 561:567, 2007.

[95] S. Miocinovic, M. Parent, C. R. Butson, P. J. Hahn, G. S. Russo, J. L. Vitek, and C. C. McIntyre, "Computational analysis of subthalamic nucleus and lenticular fasciculus activation during therapeutic deep brain stimulation," *Journal of Neurophysiology,* vol. 96, pp. 1569-1580, Sep 2006.

[96] S. Miocinovic, M. Parent, A. Parent, C. R. Butson, G. S. Russo, J. L. Vitek, and C. C. McIntyre, "Activation of the subthalamic nucleus and lenticular fasciculus during therapeutic deep brain stimulation," *Stereotactic and Functional Neurosurgery,* vol. 85, pp. 32-32, 2007.

[97] S. Miocinovic, J. Y. Zhang, W. D. Xu, G. S. Russo, J. L. Vitek, and C. C. McIntyre, "Stereotactic neurosurgical planning, recording, and visualization for

deep brain stimulation in non-human primates," *Journal of Neuroscience Methods,* vol. 162, pp. 32-41, May 15 2007.

[98] C. R. Butson, S. E. Cooper, J. M. Henderson, and C. C. McIntyre, "Predicting the effects of deep brain stimulation with diffusion tensor based electric field models," *Medical Image Computing and Computer-Assisted Intervention - Miccai 2006, Pt 2,* vol. 4191, pp. 429-437, 2006.

[99] C. R. Butson, C. B. Maks, A. M. Noecker, S. Miocinovic, B. Walter, S. E. Cooper, J. L. Vitek, A. R. Rezai, J. M. Henderson, and C. C. McIntyre, "Combined analysis of neuroanatomical, microelectrode recording, stimulation spread, and behavioral outcomes data for deep brain stimulation," *Stereotactic and Functional Neurosurgery,* vol. 85, pp. 31-31, 2007.

[100] F. J. Castro, C. Pollo, O. Cuisenaire, J.-G. Villemure, and J.-P. Thiran, "Validation of experts versus atlas-based and automatic registration methods for subthalamic nucleus targeting on MRI," *International Journal of Computer Assisted Radiology and Surgery,* vol. 1(1), p. 5:12, 2006.

[101] S. Pallavaram, P.-F. D'Haese, M. Remple, J. S. Neimat, C. Kao, R. Li, P. E. Konrad, and B. M. Dawant, "Detecting brain shift during deep brain stimulation surgery using intra-operative data and functional atlases: a preliminary study," *IEEE International Symposium on Biomedical Imaging: From Nano to Macro,* p. 362:365, 2009.